Condensation of Water Vapor and Acid Mixtures from Exhaust Gases

vorgelegt von

Diplom-Ingenieur

Maria Pla Perujo aus Valencia (Spanien)

Fakultät III-Prozesswissenschaften

der Technischen Universität Berlin

Institut für Energietechnik

Fachgebiet Energie-, Impuls- und Stofftransport

zur Erlangung des akademischen Grades

Doktor der Ingenieurwissenschaften

- Dr.-Ing. -

genehmigte Dissertation

Promotionsausschuß:

Vorsitzender: Professor Dr. -Ing. F. Ziegler

Berichter: Professor Dr.-Ing. H. Auracher

Berichter: Dr. –Ing. W. Volz

Tag der wissenschaftlichen Aussprache : 22.11.2004

Berlin 2004

D83

Acknowledgements

This research work was carried out at Robert Bosch GmbH in Stuttgart in Germany under the direction of Professor Dr.-Ing. H. Auracher of the Technische Universität Berlin. I would like to thank him for enabling this joint research project. I greatly appreciate his cooperation, his support and encouragement and his guidance during the entire course of the thesis.

I am very grateful to Dr.-Ing. W. Volz, director of this project, for providing me with the opportunity to perform this research at Robert Bosch GmbH, for many fruitful discussions and his constant availability and help.

The contributions to this work of Dr. -Ing. S. Leuthner, director of the Energy Research Department at Robert Bosch GmbH, are gratefully acknowledged.

I would like to thank Uwe Clement and Frederik Dech for the invaluable help during the planning, construction, and running of the test rig. Within the frame of the diplom thesis, I am very grateful to Florian Wahl and Jochen Buschle for their contribution and help.

I am thankful to the staff of the Corporate and Development Applied Chemistry and Energy Research at Robert Bosch GmbH. In particular, I would like to thank Brigitte Moro and Horst Magenau for the grateful discussions and help.

I would like to dedicate this thesis to my parents, Maria Angeles Perujo Ferrer and Jose Pla Iborra for their never-ending support, love and affection. I wish also to express my deep gratitude to my husband Jorge Sanchez-Montero and my brother Jose Pla Perujo for their understanding and support.

Zusammenfassung

Gas-Brennwertgeräte haben sich in den letzen 10 Jahren bewährt und werden in zunehmendem Maße für Neubauten und in der Modernisierung von bestehenden Anlagen eingesetzt. Da Gas-Brennwertgeräte in der Lage sind die im Abgas enthaltene latente Wärme in zusätzliche Heizwärme umzusetzen, arbeiten sie besonders energiesparend und erreichen einen hohen Wirkungsgrad.

Erdgas wird mit sehr geringen Schadstoffemissionen verbrannt. Das Abgas enthält jedoch neben Kohlendioxid und Wasserdampf noch Verbrennungsprodukte wie Stickstoff- und Schwefeloxide. Stickoxide sind typische Produkte der Verbrennung. Schwefeldioxid entsteht durch die Oxidation des dem Brenngas beigemischten Odorierungsmittels. Bei der Kondensation dieser Produkte entsteht eine säurehaltige Lösung, welche Salpeter- und Schwefelsäure enthält. Durch Rückverdampfung und wiederholte Kondensation wird das Rauchgaskondensat in zunehmendem Maße korrosiv. Daher korrodieren Wärmeübertrager im Brennwertgerät.

Kondensation tritt auf, wenn die Oberflächentemperatur niedriger ist als der Taupunkt der Mischung. Um den Taupunkt der Mischung zu bestimmen, waren Gas-Flüssigkeits-Gleichgewichtsmodelle wie das Van Laar Modell und das Uniquaq Modell nötig. Für das binäre System HNO_3/H_2O liegt der Taupunkt bei 56 °C für einen Druck von 0,17 bar. Für das binäre System H_2SO_4/H_2O liegt der Taupunkt für einen Druck von 0,17 bar bei 115 °C.

In der vorliegenden Arbeit wird die Kondensation von Salpeter- und Schwefelsäure sowie von Wasserdampf in Anwesenheit von Luft auf einer senkrechten wassergekühlten Platte untersucht. Ein Simulationsmodell wurde entwickelt und durch Messungen an einem Teststand validiert. Das Simulationsmodell kann auf beliebige Geometrien angewendet werden, um Parameterstudien und Optimierungen an der Geometrie zur Reduzierung von Korrosion durchführen zu können.

Es wurde eine numerische Simulation mit dem kommerziellen CFD Programm FLUENT, sowie eine Simulation basierend auf empirischen Gleichungen mit einem Differentialgleichungslöser, EES, in 2D für eine senkrechte wassergekühlte Platte durchgeführt. Die numerischen Simulationen wurden mit realen 3D-Geometrien, Lamellen- und Rippenwärmeübertrager durchgeführt.

Der Vergleich der numerischen Simulation mit der auf empirischen Gleichungen basierenden Simulation zeigt, dass die Genauigkeit für fast alle Brennerleistungen und durchschnittlichen Oberflächentemperaturen sehr gut ist. Für eine Brennerleistung von 8 kW liegt die Abweichung bei bis zu 8 %, bei höheren Brennerleistungen liegt sie bei

1-2 %. Die Abweichung hängt davon ab, wie der Diffusionskoeffizient berechnet wird. In der numerischen Simulation wird die Diffusion über die Maxwell-Stefan Gleichung für Mehrkomponentenmischungen berücksichtigt. Durch diese Gleichung werden auch die nicht-idealen Anteile der Mischung betrachtet.

Die Unterschiede zwischen Simulation und Messung liegen zwischen 7 und 25 %, abhängig von der Brennerleistung und der durchschnittlichen Oberflächentemperatur der Platte. Die größten Abweichungen treten bei der geringsten mittleren Oberflächentemperatur von 20 °C auf. Es tritt Tropfenkondensation auf. Die Tropfen wachsen dabei sehr schnell und liegen in einem Größenbereich von 1 bis 3 mm. Zwischen den Tropfen treten Wirbel in der Gasströmung auf, die die analytische Lösung des Vorgangs erschweren. Es gibt keine Gleichung die diese Verhältnisse beschreibt.

Die Anwendung der numerischen Simulation auf reale 3D Geometrien zeigt gute Übereinstimmung mit experimentellen Ergebnissen.

Abstract

Boilers, in which condensation takes place, are a very competitive technology in Europe due to energy prices, strict government regulations and a public interest in energy efficiency. They operate at high efficiency by capturing some of the latent heat of condensation, and a large amount of the sensible heat of combustion.

When natural gas is combusted, only a very small amount of pollutants are formed. The products of combustion still contain oxides of nitrogen and sulfur as well as carbon dioxide and water vapor. Nitrogen oxides are typical by-products of combustion air, and sulfur is present at very low concentrations as odourant compound added to natural gas. Condensation of these products yields an acidic solution which contains concentrations of nitric and sulfuric acids. Therefore, flue gas condensate becomes increasingly corrosive at surfaces of the condensing heat exchanger after it is concentrated by repeated condensation and evaporation.

When the surface temperature is below the dew point of the multicomponent mixture, condensation occurs. Therefore, Vapor-Liquid Equilibrium models such as the Van Laar and Uniquaq models were required in order to determine the dew point of the mixture for a pressure of 0.17 bar. For the binary system HNO_3/H_2O, the dew point is 56 °C. For the binary system H_2SO_4/H_2O it is 115 °C.

In this work, the condensation of nitric acid, sulphuric acid and water vapor in the presence of air on a vertical water-cooled plate has been investigated. A simulation model has been developed and experimentally validated using measurements from a test rig. This simulation model can be applied to a given heat exchanger design in order to perform parametric studies and geometric optimization with the goal of minimizing corrosion.

A numerical simulation using the comercial CFD code FLUENT, and a simulation based on empirical correlations using the Engineering Equation Solver EES have been carried out for a 2D vertical water-cooled plate. The numerical model was applied to real 3D geometries including an annular fin heat exchanger and a pin fin heat exchanger.

By comparing the numerical simulation with the simulation based on the empirical correlations, the accuracy is very good for almost all range of combustion powers as well as average temperature surfaces. For a combustion power of 8 kW, the deviation between both simulations is about 8 %, whereas for higher combustion powers the deviation decreases until 1-2 %. These discrepancies are due to the way in which the diffusion coefficient has been obtained. In the numerical simulation the diffusion

process is taken into consideration by using the Maxwell-Stefan equation for multicomponent mixtures. By this equation, the non-idealities of the mixture are considered whereas in the simulation based on the empirical correlations the mixture is considered as ideal.

The discrepancies between experiments and simulation are in a range 7-25 % depending on the combustion power and the average surface temperature of the plate. The highest deviations correspond to the smallest average surface temperature of 20 °C. Dropwise condensation takes place, and the drops grow very quickly and they range from 1 to 3 mm. Vortices take place between the drops making the gas stream more complex as it is usually and there is no equation taking this behaviour into consideration.

The results obtained from the numerical simulation applied to real 3D geometries closely resemble experimental observations.

Contents

Nomenclature

Latine Letters

A	surface area	$[m^2]$
A_{12}, A_{21}	parameter of the Van Laar equation	[-]
c_p	heat capacity at constant pressure	$[J/kg \cdot K]$
d	diameter	[m]
d_h	hydraulic diameter	[m]
D	diffusion coefficient	$[m^2/s]$
g	acceleration due to gravity	$[m/s^2]$
h	sensible enthalpy	[J/kg]
H_0	net calorific value	$[kJ/m^3]$
H_u	gross calorific value	$[kJ/m^3]$
h_{fg}	enthalpy of vaporization	[J/kg]
J_A	diffusive flux of species	$[kg/m^2\ s]$
l	length of the plate	[m]
L	length of the tube	[m]
$\tilde{M}$	molar mass of components	[kg/kmol]
$\dot{m}$	mass flux	$[kg/m^2\ s]$
p	pressure	[Pa]
$\dot{q}$	heat flux	$[W/m^2]$
Q	heat flow rate	[W]
p_i^{sat}	saturation pressure	[bar]
q_i	molecular surface area	[-]
r_i	molecular van der Waals volume	[-]
r	radius	[m]
R	universal gas constant = 8,3143 J/mol K	[J/mol K]
R	thermal resistance	$[m^2K/W]$
S	shape factor	[-]

T	absolute temperature	[K],[ºC]
T_{sat}	saturation temperature	[K]
u	velocity along the surface	[m/s]
u_i	energy of interaction between groups	[J/mol]
v	velocity normal to the surface	[m/s]
x	position	[m]
x_i	mass fraction of component i in the liquid phase	[-]
$\bar{x}_i$	molar fraction of component i in the liquid phase	[-]
y_i	mass fraction of component i in the vapor phase	[-]
$\bar{y}_i$	mole fraction of component i in the vapor phase	[-]

Greek Letters

α	heat transfer coeffcient	[W/m^{2}K]
α_x	local heat transfer coefficient	[W/m^{2}K]
β	stefan correction factor	[-]
ϕ	segment fraction (Uniquaq Model)	[-]
ϕ	parameter in Ackerman correction factor	[-]
γ	activity coefficient	[-]
η	dynamic viscosity	[kg/ms = Pa s]
λ	thermal conductivity	[W/m K]
λ	exceed of air	[-]
ν	kinematic viscosity	[m^2/s]
θ	area fraction (Uniquaq Model)	[-]
ρ	density	[kg/m^3]
τ_{ij},τ_{ji}	binary parameters	[-]
ξ	ackerman correction factor	[-]

Subscript

avg	average

c	coolant
cond	condensate
g	gas
h	hydraulic
i	interface or inside
l	liquid
nc	noncondensable gas
o	outlet or outside
s, sat	saturation
v	vapor
w	wall
∞	free-stream

Dimensionless Numbers

Nu	Nusselt number, $\alpha \cdot l/\lambda$
Pr	Prandtl number, $\eta \cdot c_p/\lambda$
Re	Reynolds number, $\rho \cdot u \cdot l/\eta$
Sc	Schmidt number, $\eta/(\rho \cdot D)$
Sh	Sherwood number, $\beta \cdot l/D$

1 Introduction

1.1 Motivation, Objectives and Literature Survey

The main objective of this study is the development of a simulation model in which the condensation of exhaust gases containing nitric acid, sulfuric acid and water vapor is taken into consideration. This model has to be validated experimentally in order to be able to optimize the geometry of a given heat exchanger of a condensing boiler. Furthermore, it can be applied to other fields such as exhaust gas aftertreatment.

Many applications with condensation heat transfer require to consider the presence of non condensable gases. The design of condensers depends on the knowledge of internal condensation, heat and mass transfer processes. Therefore, aim in this thesis is to increase the knowledge and understanding of condensation of multicomponent gas-vapor mixtures, $H_2O/HNO_3/H_2SO_4$, in the presence of non condensable gases such as air, after being submitted a fuel gas to a combustion reaction.

Condensation heat transfer is a vital process in the power generation industries and has, as a result, been an area of research for over a hundred years. Over this period the understanding of the condensation process has gradually improved. Theories and models have become more accurate and are now applicable to a wider range of conditions.

It is a well-known fact that non condensable gases like nitrogen or air affects the heat transfer [1][2][6]. They accumulate at the steam-water interface building an inert gas boundary layer and cause a mass transfer resistance in the vapor phase.

If the temperature of the mixture falls below the acid dew temperature at any point of the vapor phase boundary layer, droplets composed of water and acid may develop. The steam condenses on the droplets and does not reach the surface. The condensation heat transfer to the cooling water layer therefore diminishes. This effect will not be taken into consideration as it is negligible in comparison with the amount of condensation directly at the surface of the plate [42].

In this work, the condensation of water vapor and acid gases such as nitric acid and sulphuric acid, in the presence of non condensable gases on a vertical water-cooled plate was investigated. An experimental set up of a vertical water-cooled plate was built and measurements were carried out with the aim to validate the simulation model. These investigations will be next applied to other real geometries in order to develop a compact, light-weight, resistant to corrosion and low cost heat exchanger.

Since the first energy crisis in 1973, there is a tendency to reduce exhaust gases temperatures down from their original value referred to as “acid dew point”, 115-160 °C. As a result, condensation occurs, which causes a frequent occurrence of corrosion, even with carefully desulphurized fuel, and/or large investments in stainless steel apparatus [46].

As it was mentioned, it will not be only considered the condensation of water vapor, but also the condensation of acid gases. As another objective in the present work is to predict the corrosion on surfaces where these very strong acids condense.

Condensation occurs when the surface temperature is below the dew point of the multicomponent mixture. Therefore, Vapor-Liquid Equilibrium (VLE) models are required in order to determine the dew point of the mixture.

Some models as Margules and Van Laar are mathematically easier to handle than other ones as Wilson, NRTL and UNIQUAQ, but sometimes the latter give a better accuracy. In this work, a ternary mixture, $HNO_3/H_2SO_4/H_2O$, is treated. Therefore it is recommended to use the UNIQUAQ model to describe this system. The reaction mechanisms, depending on the gas temperature along the plate, have been goal of study to know which components are existing in a given location of the heat exchanger under certain conditions. From this study, the problem can be simplified by assuming that above the dew point of the binary system HNO_3/H_2O of 56 °C and below the dew point of the system H_sSO_4/H_2O of 115 °C, water and sulfuric acid condense together. For a temperature near by 56 °C, all sulfuric acid has almost condensed and by cooling down below this temperature the condensation of nitric acid and water takes place.

For the binary systems H_2SO_4/H_2O and HNO_3/H_2O, a modification of Raoult´s law provides a good approximation as the gas phase in this system behaves as an ideal mixture, but the liquid phase presents non ideality. These systems exhibit azeotropy, and the Van Laar model has been applied as the activity coefficient plays a key role in the calculation of these vapor-liquid equilibria mixtures [43][45].

Investigations of condensation of nitric acid, sulphuric acid and water vapor appears seldom in the literature. The numerical simulation of the condensation of this ternary mixture could not be found. But there are some studies in which similar topics are discussed.

A. Ganzevles [30] performed experiments with air-steam and air-steam-ethanol mixtures to asses importance of Marangoni effect in actual condensation processes for a compact polymer heat exchanger. The heat resistances were taken into consideration and the heat resistance of the condensate was quantified. The study introduces Nusselt and Sherwood numbers and friction factors based on a characteristic length scale valid in dropwise condensation. New correlations were obtained from dedicated experiments

with a varity of process conditions. These correlations are not valid for the present study as they were for an air, air-steam and air-steam-ethanol mixtures. And the wetted area fraction changes depending on the mixture. A numerical simulation was carried out for a 2D geometry where one static drop was considered, and the temperature profile was studied at the drop surface.

J.D. Jackson, P., M. Ahmadinejad [38] carried out experiments with the aim of extending the available database on the condensation of steam in the presence of non-condensable gases. The mixture of steam and air was flowing over a water-cooled plate. The condensation rate could be determined by collecting condensate over a known period of time and weighing it. The experimental work is very similar to the experiments performed in this work, but the amount of condensate was not presented and a validation of the model was not possible.

S. Kaminski [57] has used the commercial CFD code FLUENT for the numerical simulation of the air-side transport processes in finned-tube heat exchangers working as air coolers. The aim of the investigation was the computation of velocity, pressure and temperature fields in typical segments of finned-tube heat exchangers. Additionally the influence of the relative air humidity on the waviness of the fins on the air-side performance was examined. It was discussed the possible condensation on the finned-heat exchanger by means of the air humidity and the surface temperature of the fin. When the surface temperature is below the dew point of humid air, condensation occurs. But the condensation process was not included in the simulation as it is done in this work.

J. Krey [45] has investigated the evaporation of the acid mixture composed of nitric acid, sulphuric acid and water. Therefore, a calculation of the vapor-liquid equilibrium was required by using UNIQUAQ model. This model was considered in this work but for the condensation, a simplification could be assumed using the Van Laar Model.

1.2 Outline

In chapter 2, the reaction mechanisms governing the formation of acid gases are described as well as their influence on the lifetime of the equipment (plate heat exchanger, condensing boilers, particle filter etc). The condensation of these acids causes a frequent occurrence of corrosion, even with fuels that not contain any sulphur. As condensation occurs below the dew point of the mixture, different Vapor-Liquid Equilibrium (VLE) models are described in this chapter.

Due to the condensation in the presence of non-condensable gases, concentration, velocity and temperature gradients are set up. Therefore, it is necessary to solve

simultaneously a set of boundary-layer conservation equations of mass, momentum, species and energy. These equations are briefly described in chapter 3.

In chapter 4, the determination of the heat and mass transfer coefficients and the heat resistances are outlined. As inertgases are present in the gas mixture, there is not only convective heat transfer from the gas to the coolant, but a convective mass transfer is also to be taken into account. Just as the velocity and thermal boundary layers determine wall friction and convection heat transfer, the concentration boundary layer determines convection mass transfer. This bears to an important consideration of the diffusion process.

The condensation process has been modelled by using empirical correlations and numerically by using different software programs EES and FLUENT. This is presented in chapter 5.

Experiments have been carried out to validate the simulation. The test rig as well as the experimental procedure are described in chapter 6.

In chapter 7, the simulation and experimental results are discussed. Finally, the conclusions and recommendations are presented in chapter 8.

2 The Thermodynamics of Condensation from Exhaust Gases

Natural gas is the fuel used for most of the currently available high efficiency home heating appliances. The products of combustion typically include nitrogen oxides, sulfur oxides and hydrogen chloride, as well as the expected water vapor and carbon dioxide. These oxides react with water vapor forming nitric acid, HNO_3, and sulfuric acid, H_2SO_4.

The object of this chapter is to get a better understanding about the reaction mechanisms of these acid gases. They are products of the combustion process and therefore this process is also briefly described here. Another point to be addressed in the present chapter is the estimation of the dew points by means of the phase equilibrium of a binary and ternary mixture.

2.1 Combustion

Combustion is a chemical process in which a substance (fuel) reacts rapidly with oxygen and gives off heat. Exhaust gases are coming from chemical reactions of the fuel (natural gas) and oxygen.

The standard combustion equation is written by:

$$C_n H_m + \left(n + \frac{m}{4} \right) O_2 \rightarrow n\, CO_2 + \frac{m}{2} H_2O\,. \qquad [2.1]$$

The most important units of magnitude for the combustion process are the heat and calorific values which mark the energy chemically bound in the fuel, and the air needs. The Net Calorific Value (H_0) is the quantity of heat produced by the combustion of a unit (volume, mass or amount of substance) of gas in air under constant pressure, after cooling of the combustion products to the initial temperature of the gas and air, and after condensation of the water vapor created by the combustion to the liquid state. The Gross Calorific Value (H_u) is the calorific value minus the latent heat of vaporization of the water vapor formed by the combustion of the hydrogen in the fuel. The water remains as vapor. These both values are shown below for methane as constituent present in the natural gas:

Fuel Gas	H_0 [kJ/m^3]	H_u [kJ/m^3]
Methane	39819	35883

The combustion is a chemical reaction combining fuel and oxygen to produce heat and combustion products. Stoichiometric combustion conditions are those where the relative fuel and air quantities are the theoretical minimum needed to produce complete combustion. Atmospheric air contains 21% oxygen by volume and is the most convenient O_2 source. The oxygen needs are [55]:

$$O_{min} = \left[\frac{1}{2} \cdot \left(CO^b + H_2^b \right) + 2 \cdot CH_4^b + \sum \left(n + \frac{m}{4} \right) \cdot C_n H_m^b - O_2^b \right] \frac{m^3\ O_2}{m^3\ \text{fuel gas}} . \qquad [2.2]$$

Then, the minimum quantity of air is obtained by:

$$l_{min} = \frac{O_{min}}{0.21} \frac{m^3\ \text{Air}}{m^3\ \text{fuel gas}} . \qquad [2.3]$$

In practice, combustion is hardly ever carried out in stoichiometric conditions. Some industrial burners may operate at air/gas ratios which are extremely close to the theoretically correct value, but the majority of burners require a measure of air in excess of the Stoichiometric quantity to ensure complete combustion.

$$\lambda = \frac{l}{l_{min}} \qquad [2.4]$$

where l denotes the required quantity of air.

2.2 Reaction Mechanisms of Acid Gases

Water vapor and carbon dioxide as well as nitrogen oxides, sulfur oxides and hydrogen chloride are typically products of combustion. Hydrogen chloride, HCl, comes from the combustion of chlorides (salt dust), nitrogen oxides, NO_x, are a typical by-product of combustion air, and sulfur oxides, SO_x, comes from the oxidation of the sulfur present at very low concentrations as odourant compounds added to natural gas.

While sulfur dioxide is recognized as a pollutant, it is not itself a source of trouble in furnaces, boilers and chimneys. But when sulfur dioxide is further oxidized to sulfur trioxide material problems may develop.

Sulfur dioxide and nitrogen oxides, NO_x, are toxic acid gases which readily react with the water in the atmosphere to form a mixture of sulfuric acid, nitric acid and nitrous acid.

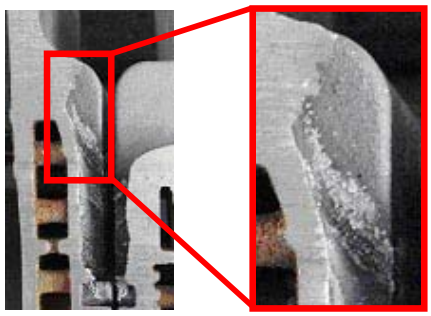

Figure 2.1 Corrosion on heat exchanger

Condensation of these reaction products occurs on surfaces which temperature are below the dew point of the gas mixture and yields an acidic solution This dilute solution of these acids result in a far greater acidity than normal (i.e. a lower pH) which could lead to corrosion (cf. Figure 2.1). In fact, the condensate becomes increasingly corrosive after it is concentrated by repeated condensation and evaporation, such as on heat exchanger surfaces.

In order to develop a model of the condensation of exhaust gases, the reaction mechanisms that take place in the gas phase depending on the gas temperature, the composition of the mixture, the dew point obtained as a function of the composition of the mixture, and consequently the amount of condensate and the pH value have to be known.

Concerning the reaction mechanisms in the gas phase, as in this study, a mixture composed of nitric acid, sulfuric acid and water will be considered, the reactions corresponding to the formation of these two acids are described below.

Nitrogen monoxide is very reactive and can, as a strongly endothermic compound, be prepared from nitrogen and oxygen [47]:

$$N_2 + O_2 \rightarrow 2NO \quad \Delta H = 90.94\ \text{KJ/mol}\ . \qquad [2.5]$$

This nitrogen monoxide is oxidized to NO_2:

$$2NO + O_2 \rightarrow 2NO_2 \quad \Delta H = -114\ \text{KJ/mol}\ . \qquad [2.6]$$

Nitrogen dioxide is a brownish red, toxic gas with a pungent odor. It is in equilibrium with its dimer, dinitrogen tetroxide, also called nitrogen peroxide, N_2O_4 (eq. [2.7]). The equilibrium is strongly temperature dependent, above 100 °C, it is shifted almost all the way toward nitrogen dioxide:

$$2NO_2 \leftrightarrow N_2O_4 \quad \Delta H = -57.2\ \text{KJ/mol}\ . \qquad [2.7]$$

Above 150 °C, nitrogen dioxide begins to dissociate:

$$2NO_2 \leftrightarrow 2NO + O_2 \quad \Delta H = -144.1\ \text{KJ/mol}\ . \qquad [2.8]$$

This reaction goes to completion at 650 °C. Figure 2.2 illustrates the dissociation of dinitrogen tetroxide and nitrogen dioxide as a function of temperature.

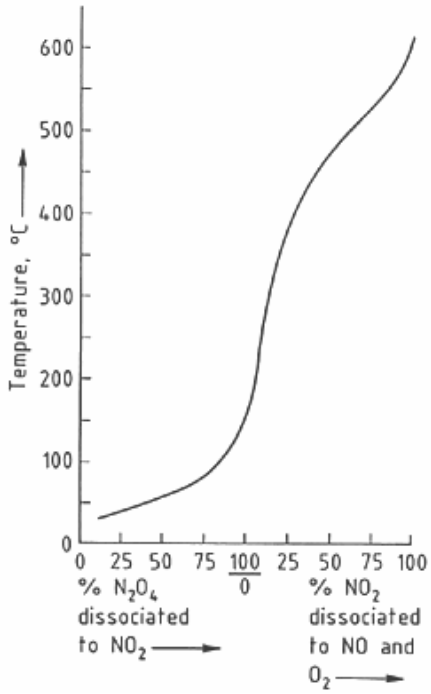

Figure 2.2 Dissociation of N_2O_4 and NO_2 as a function of temperature [47]

Nitrogen dioxide reacts with water to give nitrous and nitric acid. The nitrous acid shifts light to nitric acid and nitrogen monoxide, therefore nitric acid will appear finally:

$$4\,NO_2 + 2\,H_2O + O_2 \longleftrightarrow 4\,HNO_3\,. \qquad [2.9]$$

It is important to mention that nitric acid with water forms a maximum-boiling azeotrope at a concentration of 69.2 wt % of acid. The azeotropic mixture boils at 1 bar pressure and 121.8 °C, the boiling and dew point varies with the system pressure.

When the temperature of the mixture is higher than the boiling point, the reaction represented in eq. [2.9] shifts to the left, it means in the direction of the decomposition of nitric acid.

Highly diluted nitric acid is almost completely dissociated:

$$HNO_3 + H_2O \longleftrightarrow H_3O^+ + NO_3^-\,. \qquad [2.10]$$

In the process of obtaining sulfuric acid, sulfur dioxide forms sulfuric acid in the presence of oxygen and water by a two-step reactions.

But first the majority of the sulphur combines with oxygen to form SO_2:

$$S + O_2 \leftrightarrow SO_2 \,. \qquad [2.11]$$

At a temperature about 1200 °C, the thermodynamic equilibrium is shifted all the way toward to SO_2:
The sulfur dioxide reacts with molecular oxygen to form sulfur trioxide:

$$SO_2 + \frac{1}{2} O_2 \longleftrightarrow SO_3 \,. \qquad [2.12]$$

At a temperature of ca. 400 °C, the thermodynamic equilibrium is shifted all the way toward to SO_3. And above this temperature, the equilibrium shifts to the left to form SO_2. However, a small minority of the sulfur dioxide is further oxidized to SO_3 [32]. The formation of SO_3 is a complex process, and is dependent upon a number of factors such as the sulfur content of the fuel and amount of excess air. In [33] the conversion rate is estimated to vary from 1 to 5 percent. In the operational zone, it varies from 1 to 2 percent.

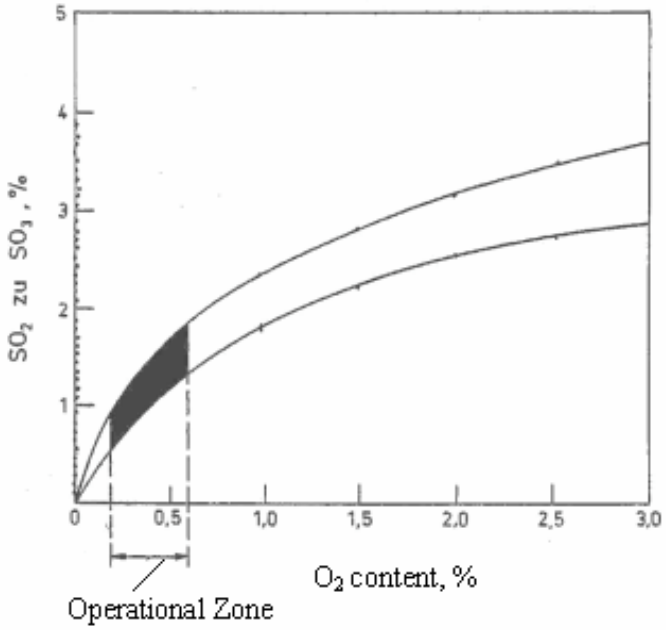

Figure 2.3 Conversion of SO_2 to SO_3 depending of the excess air [56]

It is assumed that all of the SO_3 converts to H_2SO_4. Below 400 °C begins the conversion of the sulfur trioxide in sulfuric acid, and for temperatures smaller than 176 °C, the equilibrium is all towards to H_2SO_4.

$$SO_3 + H_2O \longleftrightarrow H_2SO_4 \,. \qquad [2.13]$$

Thus, this reaction depends on the gas temperature in a range between 176 °C– 400 °C. Table 2.1 shows the dependence of the reaction above on the gas temperature.

Table 2.1 SO_3 conversion to H_2SO_4 at various gas temperature

Gas temperature [°C]	SO_3 converted to H_2SO_4, %
400	3.85
371	14.30
315	47.50
287	70.54
260	87.50
204	98.56
176	99.84

All the mechanisms of reactions above described, and corresponding to the formation of sulfuric and nitric acid are summarized in the Table 2.2 below:

Table 2.2 Reaction mechanisms for obtaining sulfuric and nitric acid

H_2SO_4	HNO_3
$S(g) + O_2(g) \rightarrow SO_2(g)$	$N_2(g) + O_2(g) \rightarrow 2\ NO(g)$
[1200 °C]	[1200 °C-650 °C]
$SO_2\ (g) + 1/2\ O_2 \leftrightarrow SO_3\ (g)$	$2\ NO(g) + O_2 \leftrightarrow 2\ NO_2\ (g)$
[1200 °C -400 °C]	[650 °C-150 °C]
$SO_3(g) + H_2O \rightarrow H_2SO_4(g)$	$2\ NO\ (g) + O_2 \rightarrow 2\ NO_2\ (g)$
[400 °C -120 °C]	[120 °C]
$[T<T^s_g]\ H_2SO_4(l)$	$[T<T^s_g]\ HNO_3\ (l)$
Condensation of H_2SO_4	$NO_2(g)+H_2O(g) \rightarrow 2\ HNO_3\ (l) + NO\ (g)$
	Condensation of HNO_3

From these reactions, the composition of each component in the gas mixture can be calculated, and therefore the dew point can be obtained as it depends on the mass fraction of the components present in the mixture and the pressure of the system.

2.3 Vapor-Liquid Equilibrium in Binary Mixtures

Design of condensing boilers requires the estimation of the phase equilibrium of fluid mixtures in order to know the composition of the vapor which is in equilibrium with the liquid mixture.

Whenever experimental data are available, there is a few or even no mixture data, and it is necessary to estimate the phase equilibrium from some suitable correlations. In this work, calculations are based on the Van Laar and UNIQUAC equations. Both models are presented in this chapter for different fluid mixtures, and it is to be mentioned that these available correlations or models are essentially empirical.

2.3.1 Introduction to Vapor-Liquid Equilibrium

Raoult´s law is the simplest model that allows to do VLE calculations. This is obtained when it is assumed that the vapor phase is an ideal gas, and the liquid phase is an ideal solution. Mathematically, it is expressed as:

$$y_i P = x_i P_i^{sat} \quad \text{for all species } (i=1,2,...,N) \qquad [2.14]$$

where x_i is the liquid phase mole fraction, y_i is the vapor phase mole fraction, P_i^{sat} is the vapor pressure of pure component i, and P is the total pressure. Raoult's law says that the partial pressure of each species in the vapor phase is equal to its mole fraction in the liquid phase times its pure-component vapor pressure.

The most straightforward, and perhaps the most commonly encountered types of VLE calculations are bubble point and dew point calculations. In a dew point temperature calculation, the temperature at which the first tiny bit of liquid forms when a vapor mixture of specified composition is cooled at constant pressure is computed, as well as the composition of the liquid.

There are a wide range of situations where the pressure is low enough that the vapor phase is nearly, but the liquid phase is not an ideal solution. Thus, much more realistic VLE calculations can often be done using a modified version of Raoult's Law that can be stated as:

$$y_i P = x_i \gamma_i P_i^{sat} \quad \text{for all species } (i=1,2,...,N) \qquad [2.15]$$

Where γ_i is called the activity coefficient of species i in the solution, and generally depends on both temperature and the solution composition. The activity coefficients play a key role in the calculation of vapor-liquid equilibria, specially in azeotropic mixtures. The Van Laar Model is used to estimate these coefficients for the binary systems HNO_3/H_2O and H_2SO_4/H_2O. And the UNIQUAQ model (a group contribution

method) is used to estimate these coefficients for the ternary mixture $H_2SO_4/H_2O/HNO_3$, as the non ideality is stronger and it has to be taken into account in more accuracy.

2.3.2 Nitric Acid/Water

Many binary systems exhibit azeotropic condition in which the composition of a liquid mixture is equal to that of its equilibrium vapor. The liquid phase is not an ideal solution, and therefore the estimation of the activity coefficients is necessary. The nitric acid (HNO_3) with water (H_2O) forms a maximum-boiling azeotrope at a concentration of 69.2 wt % of acid. The azeotropic mixture boils at 121.8 °C at 1 bar pressure, but as it is known the boiling and dew point varies with the pressure of system. The pressure of this binary system in the present work is about 0,17 bar. The Van Laar model [42] is used to estimate the phase equilibrium for this binary system at this pressure.

The Van Laar model states as:

$$\frac{G^E}{RT} = x_1 x_2 \left[\frac{A_{21}A_{12}}{A_{12}x_1 + A_{21}x_2} \right] \qquad [2.16]$$

where G^E is the excess Gibbs energy for a binary solution. Both constants A_{21} and A_{12} are specific for each binary system, and x_1 and x_2 are the mole fractions of the components in the mixture. The activity coefficients are determined by the following equations:

$$\ln \gamma_1 = A_{12} \left[\frac{A_{21}x_2}{A_{12}x_1 + A_{21}x_2} \right]^2 \quad \text{and} \qquad [2.17]$$

$$\ln \gamma_2 = A_{21} \left[\frac{A_{12}x_1}{A_{12}x_1 + A_{21}x_2} \right]^2 . \qquad [2.18]$$

When the azeotropic conditions (temperature, pressure, composition) are known, activity coefficients γ_1 and γ_2 at that condition are readily found by the equation below:

$$\gamma_i = \frac{P}{P_i^{sat}} \qquad [2.19]$$

with $y_i = x_i$, total pressure P and pure component vapor pressures P_i^{sat}. With these activity coefficients and the azeotropic composition it is possible then to find the two parameters A_{12} and A_{21} by simultaneous solution of the equations 2.17-2.18. The values of the activity coefficients are presented in a Table F.1 in the Appendix F.

2.3.3 Sulfuric Acid/Water

This binary mixture exhibit azeotropy as the former binary system. So, proceeding in the same way as above described for the binary system nitric acid (HNO_3) and water (H_2O), the activity coefficients for this system sulfuric acid (H_2SO_4)/water(H_2O) are estimated. The values of the activity coefficients are presented in Table G.1 in the Appendix G.

2.3.4 Air/Water

In case that no acids are contained in the mixture, and only water vapor is present, the dew point is then calculated for a mixture of water vapor and air as a function of the content of water $x_{water,sat}$ in the air [9]. From this data, functions are adjusted in order to obtain the saturation temperature T_{sat} in ºC:

- $x_{water,sat} < 0.0522$

$$T_{sat} = \frac{\ln\left(\frac{1000\, x_{water,sat}}{4.03}\right)}{0.064} \qquad [2.20]$$

- $0.163 < x_{water,sat} < 0.0522$

$$T_{sat} = \frac{\ln\left(\frac{1000\, x_{water,sat}}{5.11}\right)}{0.057} \qquad [2.21]$$

- $0.298 < x_{water,sat} < 0.163$

$$T_{sat} = \frac{\ln\left(\frac{1000\, x_{water,sat}}{4.12}\right)}{0.060} \qquad [2.22]$$

- $0.507 < x_{water,sat} < 0.298$

$$T_{sat} = \frac{\ln\left(1000\, x_{water,sat} + 1369.9\right)}{23.46} \qquad [2.23]$$

- $x_{water,sat} > 0.507$

$$T_{sat} = \frac{\ln\left(\frac{1000\, x_{water,sat}}{0.037}\right)}{0.12} \qquad [2.24]$$

2.4 Vapor-Liquid Equilibrium (VLE) in Multicomponent Mixtures

For the estimation of activity coefficients, it is necessary to choose some thermodynamically consistent analytical expression which relates activity coefficients to mole fraction. For the binary systems nitric acid/water and sulfuric acid/water, calculations were based on the van Laar equation. But in the case that the system is composed of nitric acid/sulfuric acid/water, the non ideality has to be considered in more accuracy than for the binary systems. Therefore, the UNIQUAQ method is used, one of the group contribution methods [43].

2.4.1 Sulfuric Acid/Nitric Acid/Water

The ternary mixture sulfuric acid/nitri acid/water is an aqueous solution of electrolytes. In this case, the ions to be considered are H_3O^+, SO_4^{-2} and NO_3^-. The best method to estimate the phase equilibrium of such systems is the UNIQUAQ method, and this is described in detail below.

First, the UNIQUAQ model per se contains a combinatorial part, essentially due to differences in size and shape of the molecules in the mixture, and a residual part, essentially due to energy interactions. Second, functional group sizes and interaction surface areas are introduced from independently obtained pure component molecular structure data.

The UNIQUAQ equation often gives good representation of both vapor-liquid and liquid-liquid equilibria for binary and multicomponent mixtures containing a variety of nonelectrolytes as water, alcohols, esters, amina etc. In a multicomponent mixture, as it is the case in the present thesis, the UNIQUAQ equation for the activity coefficient of component i is [45]:

$$\ln \gamma_i = \underbrace{\ln \gamma_i^{C}}_{\text{combinatorial}} + \underbrace{\ln \gamma_i^{R}}_{\text{residual}} \qquad [2.25]$$

where

$$\ln \gamma_i^{C} = \ln \frac{\phi_i}{x_i} + \frac{z}{2} q_i \ln \frac{\theta_i}{\phi_i} + \ell_i \frac{\phi_i}{x_i} \sum_j \tilde{x}_j \ell_j \qquad [2.26]$$

and

$$\ln \gamma_i^{R} = q_i \left[1 - \ln \left(\sum_j \theta_j \tau_{ji} \right) - \sum_j \frac{\theta_j \tau_{ij}}{\sum_k \theta_k \tau_{ki}} \right] \qquad [2.27]$$

$$\ell_i = \frac{z}{2}(r_i - q_i) - (r_i - 1) \qquad z = 10 \qquad [2.28]$$

$$\theta_i = \frac{q_i \tilde{x}_i}{\sum_j q_j \tilde{x}_j} \qquad \phi_i = \frac{\tau_i \tilde{x}_i}{\sum_j r_j \tilde{x}_j} \qquad \tau_{ij} = \exp\left(-\frac{u_{ji} - u_{ii}}{RT}\right). \qquad [2.29]$$

In these equations x_i is the mole fraction of component i and the sumations in equations 1.26 and 1.27 are over all components, including component i, θ_i is the area fraction, and ϕ_i is the segment fraction, which is similar to the volume fraction. Pure component parameters r_i and q_i are, respectively, measures of molecular van der Waals volumes and molecular surface areas. u_{ji} and u_{ii} are a measure of the energy of interaction between groups and they are obtained from experimental data. They are presented in the Appendix H.

In UNIQUAQ, the two adjustable binary parameters τ_{ij} and τ_{ji} appearing in the equation 2.27 must be evaluated from experimental phase equilibrium data.

The parameters r_i and q_i are calculated as the sum of the group volume and area parameters R_k and Q_k given in Appendix H. These group parameters are obtained from the van der Waals group volume and surface areas V_{wk} and A_{wk}, given by Bondi:

$$R_k = \frac{V_{wk}}{15.17 \frac{cm^3}{mol}} \quad \text{and} \quad Q_k = \frac{A_{wk}}{2.510^9 \frac{cm^3}{mol}}. \qquad [2.30]$$

3 Conservation of Mass, Momentum, Species and Energy for Laminar Flow

The presence of noncondensable gases leads to a significant reduction in heat transfer during condensation. A gas-vapor boundary layer (e.g., air-vapor) forms next to the condensate layer and the partial pressures of gas and vapor vary through the boundary layer. The build-up of noncondensable gas near the condensate film inhibits the diffusion of the vapor from the bulk mixture to the liquid film and reduces the rate of mass and energy transfer.

At the plate three boundary layers, concentration, momentum and temperature are formed simultaneously. By developing the governing equations, an understanding of the physical effects that determine boundary layer behavior can be improved and their relevance to convective transport further illustrated.

Thus, it is necessary to solve simultaneously a set of boundary-layer conservation equations of mass, momentum, species and energy [6]. These equations are already implemented in the software FLUENT and they will be solved in order to carry out the numerical simulation.

3.1 Physical Model and Coordinates

A schematic representation of the physical model and a coordinate system are shown in Figure 3.1.

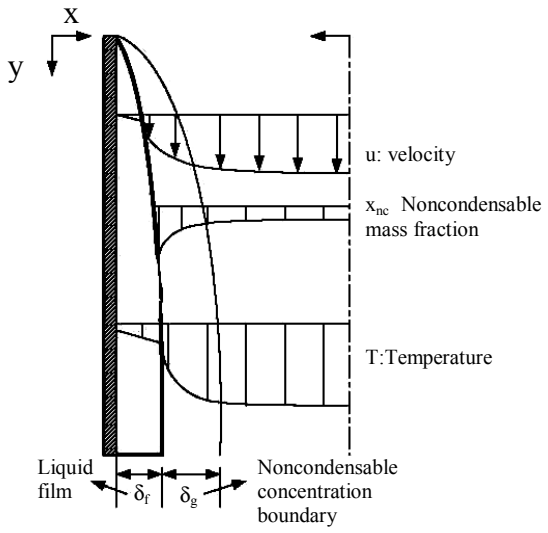

Figure 3.1 Coordinate system and related physical quantities

The coordinates along and normal to the surface are y and x respectively, and the corresponding velocity components are v and u. The vapor has a velocity u, temperature T, and noncondensable gas mass fraction x_{nc}. It is assumed that laminar flow within the liquid and vapor phases is induced by gravity g. The equations of conservation for steady laminar flow with condensation are described in the following section.

3.2 Continuity Equation

The equation for conservation of mass or continuity equation must be satisfied at every point in the velocity boundary layer. The equation applies for a single species fluid, as well as for mixtures in which species diffusion may be occurring [6].

This is the general continuity equation for every point in a fluid flow whether steady or unsteady, compressible or incompressible:

$$\frac{\partial}{\partial x}(\rho \cdot u)+\frac{\partial}{\partial y}(\rho \cdot v)=-\frac{\partial \rho}{\partial t}\,. \qquad [3.1]$$

With ρ representing the mass density, u for the velocity in mainstream, and v for the normal component.

In case of steady state, the eq. 3.1 is simplified:

$$u\frac{\partial(\rho)}{\partial y}+v\frac{\partial(\rho)}{\partial x}=0\,. \qquad [3.2]$$

For an incompressible fluid, the density ρ is constant and the eq. 3.2 becomes:

$$\frac{\partial(u)}{\partial y}+\frac{\partial(v)}{\partial x}=0\,. \qquad [3.3]$$

3.3 Momentum Equation

The second fundamental law that is pertinent to the velocity boundary layer is Newton´s second law of motion. This law states that the rate of change of momentum of a fluid particles equals the sum of the forces on the particle.

There are two types of forces on fluid particles:

- Surface forces: -pressure, and viscous forces
- Body forces: -gravity, centrifugal, coriolis, and electromagnetic forces

Eq. 3.4 represents the momentum equation for the steady state case in which the two terms on the left-hand side represent the net rate of momentum flow, and the terms on the right-hand side account for net viscous and pressure forces, as well as the body force of gravity.

$$\rho_v u\frac{\partial u}{\partial x}+\rho_v v\frac{\partial u}{\partial x}=\rho_v g-\frac{\partial p}{\partial x}+\frac{\partial}{\partial y}\left(\mu_v\frac{\partial u}{\partial y}\right). \qquad [3.4]$$

Assuming incompressible, steady laminar flow with constant fluid properties and negligible viscous dissipation and dp/dx=0, the equation is reduced to:

$$\rho_v u\frac{\partial u}{\partial x}+\rho_v v\frac{\partial u}{\partial x}=\rho_v g+\mu_v\frac{\partial}{\partial y}\left(\frac{\partial u}{\partial y}\right). \qquad [3.5]$$

3.4 Conservation of Species

The mass balance equation for a component A in a multicomponent mixture is:

$$\frac{\partial(\rho x_A)}{\partial t}+\omega\frac{\partial(\rho x_A)}{\partial x}=\frac{\partial}{\partial y}\left(j_A^*\right)+\dot{\Gamma}_A \qquad [3.6]$$

with ω representing the mass average velocity of the mixture, $x_A=\rho_A/\rho$ as mass fraction of the component A, Γ_A is the rate of increase of the mass of species A per unit volume of the mixture (kg/s m^3) and j_A^* is the relative or diffusive flux of species.

For a binary mixture consisting of two components A and B is the diffusive flux of the specie A j_A^* described by Fick's law:

$$j_A^*=-\rho D_{AB}\frac{\partial x_A}{\partial y}. \qquad [3.7]$$

For a multicomponent mixture consisting of N components is the diffusive flux of the specie A j_A^* described by eq. 3.8 below [6][33]:

$$j_A^*=-\rho\sum_{\substack{K=1\\K\neq A}}^{N}\frac{\tilde{M}^2}{\tilde{M}_A\cdot\tilde{M}_K}D_{AK}\partial x_A. \qquad [3.8]$$

If v is the velocity in the mainstream, u the one in the normal direction, and steady state is assumed, a two dimensional mass transport from eq. 3.6 for a binary mixture composed by components A and B is written:

$$u\frac{\partial(\rho x_A)}{\partial x}+v\frac{\partial\left(\rho x_A\right)}{\partial y}=\frac{\partial}{\partial y}\left(\rho D_{AB}\frac{\partial x_A}{\partial y}\right)+\frac{\partial}{\partial x}\left(\rho D_{AB}\frac{\partial x_A}{\partial x}\right)+\dot{\Gamma}_A . \qquad [3.9]$$

The diffusion coefficient and viscosity of the liquid can vary in the mainstream direction (x-direction) as well as in the normal direction (y-direction) depending on the temperature and the concentration

Diffusion in the mainstream (x-direction) is negligible in comparison with the convection in this direction. Therefore [1]:

$$u\frac{\partial(\rho x_A)}{\partial x}+v\frac{\partial\left(\rho x_A\right)}{\partial y}=\frac{\partial}{\partial y}\left(\rho D_{AB}\frac{\partial x_A}{\partial y}\right)+\dot{\Gamma}_A . \qquad [3.10]$$

A two dimensional mass transport for a multicomponent mixture can be obtained by substituting the eq. 3.8 in the eq. 3.6.

3.5 Energy Equation

Before deriving the equation of energy conservation, it is necessary to delineate the relevant physical processes. The energy per unit mass of the fluid includes the thermal internal energy e and the kinetic energy $v^2/2$:

$$E = h-(e+\frac{v^2}{2}) \qquad [3.11]$$

where h is the sensible enthalpy for compressible flows defined as:

$$h = \sum y_i h_i \qquad [3.12]$$

and for incompressible flows:

$$h = \sum y_i h_i + \frac{p}{\rho} \qquad [3.13]$$

with p for the pressure, ρ for the density of the fluid and h_i is the enthalpy of the component i described by the equation:

$$h_i = \int_{T_{ref}}^{T} C_{p,i}\,dT \qquad [3.14]$$

where T_{ref} is 298.73 K.

Energy is also transferred due to the diffusion of species and by work interactions involving the body and surface forces.

The conservation of energy equation takes the form:

$$\frac{\partial}{\partial t}(\rho E) + \nabla\left(\vec{v}(\rho E + p)\right) = \nabla\left(\lambda \nabla T - \sum_j h_j \vec{J}_i + \left(\bar{\bar{\tau}}\vec{v}\right)\right) + S_h \qquad [3.15]$$

where λ is the thermal conductivity, J_i is the diffusion flux of species i, h_i is the enthalpy of the component i in the mixture. The first three terms on the right-hand side represent energy transfer due to conduction, species diffusion, and viscous dissipation, respectively. S_h includes the heat of chemical reaction, and any other defined volumetric heat sources [36].

Assuming steady state, negligible viscous dissipation and dp/dx=0, the thermal boundary layer equation reduces to [37]:

$$\rho_v C_{p,v} u \frac{\partial T}{\partial x} + \rho_v C_{p,v} v \frac{\partial T}{\partial y} = \frac{\partial}{\partial y}(\lambda_v \frac{\partial T}{\partial y}) + \lambda_v \frac{\partial T}{\partial y}\frac{\partial \ln C_{p,v}}{\partial y} + C_{p,v}\frac{\partial (j_A^*)}{\partial y}\frac{\partial T}{\partial y} \qquad [3.16]$$

where j_A^* is the diffusive flux of the specie A in a binary or multicomponent mixture, as it is defined in the eq. 3.8.

4 Heat and Mass Transfer on a Cooled Vertical Plate with Condensation

In this chapter heat and mass transfer are simultaneously considered due to the condensation process of multicomponent mixtures. Several empirical correlations based on heat and mass transfer analogy are given as well as the diffusion coefficient for binary and multicomponent mixtures. These analogies are implemented in the simulation model developed by using the software EES presented in chapter 5. The heat resistances which play an important role are also described in this chapter and implemented in the model.

4.1 Heat Transfer Correlations for Forced Convection

4.1.1 Heat Transfer on the Coolant Side

Gnielinski correlation [15] was used from VDI Atlas adopting: 1) the Stephan correction [16] to consider small tube lengths (Laminar region), 2) the Rotta correction [18] as in small interval of time the laminar flow changes to turbulent (Transition region), and 3) the Konakov correction [17] to take into account a pressure factor (Turbulent region). The resulting relationships are:

$$Nu_L = \frac{\alpha_{water} d_i}{\lambda_{water}} \qquad [4.1]$$

Laminar Flow ($Re < 2300$ and $0.6 \le Pr \le 1000$))

$$Nu_{m,L} = [49.37 + ((1.62\,(2300\,Pr\,\frac{d_i}{l})^{\frac{1}{3}}) - 0.7)^3 + (Nu_{m,3,2300})^3]^{\frac{1}{3}} \qquad [4.2]$$

$$Nu_{m,3,2300} = [(\frac{2}{1+22\cdot Pr})^{\frac{1}{6}}\,(2300\,Pr\,\frac{d_i}{l})^{\frac{1}{2}}]^{\frac{1}{3}} \qquad [4.3]$$

Transition Region ($2300 < Re < 10^4$ and $0.6 \le Pr \le 1000$))

$$Nu_m = (1-\gamma)\,Nu_{m,L,2300} + \gamma\,Nu_{m,T,10^4} \qquad [4.4]$$

$$\gamma = \frac{\mathrm{Re} - 2300}{10^4 - 2300} \qquad 0 \le \gamma \le 1 \qquad [4.5]$$

Turbulent Region ($\mathrm{Re} \ge 10^4$ $0.6 \le \mathrm{Pr} \le 1000$)

$$\mathrm{Nu_m} = \frac{(\frac{\xi}{8})\ \mathrm{Re}\ \mathrm{Pr}}{1 + 12.7\ \sqrt{\frac{\xi}{8}}\ (\mathrm{Pr}^{\frac{2}{3}} - 1)} [1 + \left(\frac{d_i}{l}\right)^{\frac{2}{3}}] \qquad [4.6]$$

with

$$\xi = (1{,}8 \cdot (\log_{10} \mathrm{Re}) - 1.5)^{-2} \qquad [4.7]$$

4.1.2 Heat Transfer through the Wall

The heat transfer through the wall was accounted by a conventional relationship for a wall:

$$q = \lambda\ S\ (T_{w,o} - T_{w,i}) \qquad [4.8]$$

where S is the shape factor of a two-dimensional system [39].

4.1.2.1 Shape Factor

Shape factors to describe the heat transfer through conduction have been obtained for numerous two-dimensional systems [39], and results are tabulated for some common configurations. As it is shown in Figure 6.2 in chapter 6, a plate made of cooper coated with gold is mounted on an aluminium plate through which cool fluid is flowing. The geometry shape for a section of the plate can be observed in Figure 4.1:

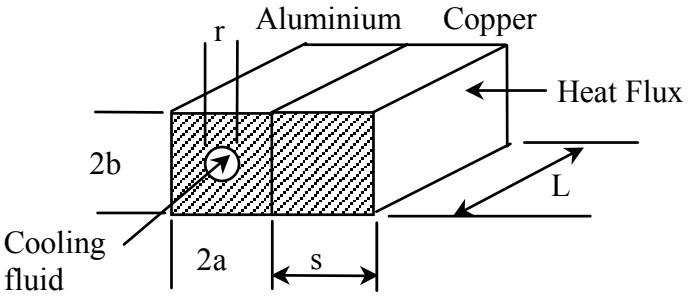

Figure 4.1 Schematic of the geometry shape of a section of the water-cooled plate

For the copper plate, the shape factor is obtained as follows:

$$S_{copper} = \frac{A}{s} \qquad [4.9]$$

where A and s are the area and thickness of the cooper wall.

For the aluminum plate, the shape factor goes like this:

$$S_{Alumimun} = \frac{2\pi L}{\ln\left(\frac{4a}{\pi r}\right) - 2C} \qquad [4.10]$$

with L as length of the tube where the cool fluid is flowing through, r radius of the tube and C a constant value depending on b and a:

Table 4.1 C values for the shape factor

b/a	1	1,5	2	3	5	∝
C = f(b/a)	0.0829	0.0178	0.0037	0.0016	$3.01\ 10^{-7}$	0

4.1.3 Heat Transfer through the Condensate Film

The heat transfer through the condensate film is estimated from the Nusselt correlation given by Stephan [6]:

$$\overline{\alpha}_{film} = 0{,}936 \cdot \left(\frac{\rho_L^2 \cdot g \cdot \Delta h_v^* \cdot \lambda_L^3}{\eta_L \cdot (T_s - T_w)} \cdot \frac{1}{L} \right)^{\frac{1}{4}} \qquad [4.11]$$

where ρ_l is the liquid density, g the gravity, λ_l thermal conductivity of the liquid, η_l liquid viscosity, T_s saturation temperature, T_w wall temperature, L is the length of the plate, $c_{p,l}$ specific heat capacity of the liquid, and Δh_v^* latent heat of vaporization modified by Rohsenow [20] with the inclusion of thermal advection effects:

$$\Delta h_v^* = c_{p,g} \cdot (T_g - T_s) + \Delta h_v + 0.68 \cdot c_{p,l} \cdot (T_s - T_w). \qquad [4.12]$$

The first term refers to the cooling from a superheated gas to the saturation temperature, and the last term refers to the subcooling of the liquid in x-direction.

4.1.4 Heat Transfer Analogy in the Vapor-Gas Mixture

The convective heat transfer in the gas is estimated from the Hilpert correlation by Dewitt and Incropera [6]:

$$Nu = C\,Re^{m}\,Pr^{n}\,. \qquad [4.13]$$

This empirical correlation is widely used, and the constants C, m and n can be found in [6].

An analysis of the fluid flow over the plate that considers conservation of momentum and energy including the effects of viscosity, temperature, and heat entering the plate from the fluid, results in the following equation for the local Nusselt number Nu_x as a function of x for laminar flow:

$$Nu_x = \frac{\alpha_x x}{\lambda} = 0.332\,Re_x^{1/2}\,Pr^{1/3}\,. \qquad [4.14]$$

If the flow is laminar over the entire surface, integration over the plate length L yields the Average Nusselt Number:

$$Nu_L = \frac{\alpha_L L}{\lambda} = 0.664\,Re_L^{1/2}\,Pr^{1/3} \qquad [4.15]$$

where α_L is the heat transfer coefficient.

A correction factor is considered due to the influence of the inertgas. This factor is known as Ackerman-Korrektur [1] and it is defined as follows:

$$\varsigma_{Ackerman} = \frac{\phi}{\exp(\phi)-1} = \frac{\dot{m}\,C_{p,g}/\alpha_g}{\exp(\dot{m}\,C_{p,g}/\alpha_g)-1} \qquad [4.16]$$

with $\dot{m}$ as mass flux and C_p the heat capacity of the gas

Since fluid properties can vary significantly with the temperature, there can be some ambiguity as to which temperature should be used to select property values. The recommended approach is the use of the average of the wall and free-stream temperatures, defined as the film temperature T_i:

$$T_i = \frac{T_w + T_g}{2}\,. \qquad [4.17]$$

4.2 Mass Transfer Correlations for Forced Convection

4.2.1 Rate Equations for Molecular Diffusion

The rate equation for mass diffusion is known as Fick´s law, and for the transfer of species A in a binary mixture of A and B, it can be expressed as:

$$J_A = -\rho D_{AB} \frac{\partial x_A}{\partial x} . \qquad [4.18]$$

This expression is analogous to Fourier´s law. Moreover, just as Fourier´s law serves to define one important transport property , the thermal conductivity, Fick´s law defines a second important transport property, namely the binary diffusion coefficient or mass diffusivity D_{AB}.

The quantity J_A is the mass flux of species A, and it is the amount of A that is transferred per unit time and per unit area perpendicular to the direction of transfer, and it is proportional to the mixture mass density ρ (kg/m^3), and to the gradient of species mass fraction x_A.

4.2.2 Diffusion Coefficient in Binary Gas Mixtures

There are several empirical correlations useful to estimate the gaseous diffusion coefficient in low-pressure binary mixtures up to about 10 bar. Experimental values are available for many pairs. The empirical correlations include equations proposed by Arnold, Gilliland, Andrussow, Wilke and Lee, Slattery and Bird, Chen and Othmer, Othmer and Chen, and Füller, Schettler, and Giddings [41].

Probably, the best of these empirical correlations is the one proposed by Füller, Schettler, and Giddings:

$$D_{ij} = \frac{0.001\, T^{1,75}(1/M_i + 1/M_j)^{1/2}}{p\,[(\sum \nu_i)^{1/3} + (\sum \nu_j)^{1/3}]^2} . \qquad [4.19]$$

The quantities $\sum\nu_i$, $\sum\nu_j$ are obtained by summing atomic-diffusion volumes for each constituent of the binary. Values of ν are listed in the Appendix D. M_i, M_j are the molar mass of the components i and j and T is the temperature in Kelvin.

The reliability of this method was tested by comparison to experimental data from the literature, as the other methods [41]. The average deviation between calculated and experimental values for binary gas systems at low pressures is 4 to 7 percent.

4.2.3 Diffusion in Multicomponent Mixtures

The effective diffusion coefficient D_{im} of the species i in a multicomponent mixture depends on the fluxes of the other species present. The coefficient D_{im} can, however, be related to the fluxes of the other components and the binary coeffcients D_{ij}, where the subscripts i and j refer to the different species in the mixture [2],[33]:

$$D_{im} = \frac{1 - \tilde{y}_i}{\sum_{j \neq i}^{n} \frac{\tilde{y}_j}{D_{ij}}} \qquad [4.20]$$

with D_{im} is the mass diffusion coefficient for species i in the mixture, D_{ij} the binary mass diffusion coefficient of component i in component j and y_j is the mole fraction of species i and y_j the mole fraction of species j.

As air does not condense under the given conditions, the case corresponds to the diffusion of three gases (Water, nitric acid, sulfuric acid) in a quaternary mixture in which one gas is stagnant (air) [34,36]. But as it is about a multicomponent mixture, the binary coefficients should be calculated by the Maxwell-Stefan equation (see Appendix E) from the binary diffusion coefficients D_{ij} obtained by eq. 4.19. Therefore, the binary diffusion coefficients D_{ij} is replaced by $D_{ij,Maxwell}$ in the equation 1.20. In case that the gas would be considered as ideal the Maxwell diffusion coefficients $D_{ij,Maxwell}$ are equal to the binary coefficients D_{ij}.

The mass flux of species i through the mixture containing n-components is written then:

$$J_i = -\rho\, D_{im} \frac{\partial x_i}{\partial x} - D_{T,i} \frac{\nabla T}{T} . \qquad [4.21]$$

The second term in the above equation corresponds to the thermal diffusion. This one is negligible in comparison to the mass diffusion for the case in this work. Therefore it will not be taken into consideration [41].

4.2.4 Mass Transfer Analogy in the Vapor-Gas Mixture

Assuming analogy, the mass transfer correlation for laminar flow has the same form as the corresponding heat transfer correlation, simply replacing Nusselt by Sherwood and Prandtl by Schmidt [6]:

$$Sh_x = \frac{\beta_x x}{D} = 0.332\, Re_x^{1/2}\, Sc^{1/3} . \qquad [4.22]$$

This is the equation for the Local Sherwood number, but if the flow is laminar over the entire surface, the average Sherwood number is obtained by integration over the plate length L. Then, the Average Sherwood number is:

$$Sh_L = \frac{\beta_L L}{D} = 0.664\,Re_L^{1/2}\,Sc^{1/3} \qquad [4.23]$$

where β is the mass transfer coefficient. As for the heat transfer coefficient where a correction factor called Ackerman-Korrektur is used, a correction factor called Stefan-Korrektur is used for the mass transfer coefficient to take into account for the influence of the flux caused by mass transfer perpendicular to the surface [1][2].

$$\varsigma_{stefan} = \frac{\phi}{\exp(\phi)-1} = \frac{\dot{m}/\rho\,\beta}{\exp(\dot{m}/\rho\,\beta)-1} \qquad [4.24]$$

with m as mass flux and ρ density of the gas

To take into account the temperature dependence of the fluid properties, the average temperature of the wall and free-stream is considered:

$$T_i = \frac{T_w + T_g}{2}\,. \qquad [4.25]$$

4.3 Heat Transfer Resistances

The heat is transferred from the gas at high temperature to the coolant at lower temperature.

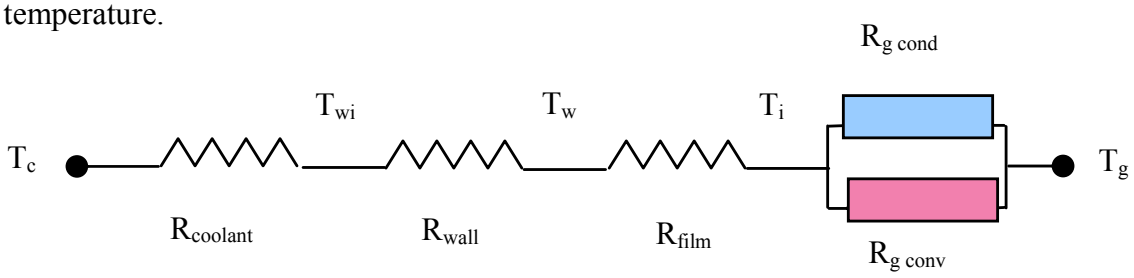

Figure 4.2 Thermal resistances encountered from the bulk mixture to the coolant

From the gas to the interface of the condensate with the temperature T_i, heat is transferred via convective heat transfer α_{conv}, and via convective mass transfer $\alpha_{g,cond}$. This is due to the boundary layer formed next to the condensate because of the presence of noncondensable gases. There is an additional resistance $R_{g,cond}$ to take into consideration in the gas phase as the components have to diffuse through this gas

boundary layer towards the wall. The heat transferred from the gas to the interface of the condensate is transferred then through the condensate to the surface, where the temperature is T_w, and this heat is transferred through the wall to the coolant with the temperature T_c. The heat transfer coefficient for the condensate is α_i and for the coolant α_c.

If inert gases are not present in the gas mixture, there is only convective heat transfer from the gas to the coolant. Heat resistances are defined as the inverse of the heat transfer coefficient. Each heat transfer coefficient, and therefore each heat resistance, have to be known in order to know the influence on the heat transfer mechanism. The total heat resistance is given by

$$R_{tot} = R_g + R_{film} + R_{wall} + R_{coolant}$$

with

$$R_g = \left(\frac{1}{R_{g,cond}} + \frac{1}{R_{g,conv}} \right)^{-1} \qquad [4.26]$$

$$R_{g,cond} = \frac{1}{\alpha_{g,cond}} \qquad [4.27]$$

$$R_{g,conv} = \frac{1}{\alpha_{g,conv}} \qquad [4.28]$$

with $\alpha_{g,cond}$ as condensation heat transfer coefficient. This coefficient is related to the Sherwood number, suitable for mass transfer processes, and to the condensation conductivity by means of the standard expression:

$$\alpha_{g,cond} = \frac{Sh\,\lambda_{cond}}{L} \qquad [4.29]$$

where the condensation conductivity is given by Peterson [10]:

$$\lambda_{cond} = \frac{D_{ij} h_{fg}^{\,2} C_{p,g} M_v^{\,2}}{RT^2} \phi \qquad [4.30]$$

ϕ is the logarithmic gas concentration distribution of steam and non-condensable in the gas boundary layer:

$$\phi = \frac{X_{nc,avg}}{X_{v,avg}} = -\frac{\ln((1 - x_{nc,bulk}) / (1 - x_{nc,i}))}{\ln(x_{nc,bulk} / x_{nc,i})} . \quad [4.31]$$

The condensation heat resistance $R_{g,cond}$ is combined in parallel with the convective heat resistance $R_{g,conv}$.

This parallel combination of the convective and condensation gas resistances is coupled in serie to those of condensate layer, the wall and the coolant. The condensate layer resistance is given by:

$$R_{film} = \frac{1}{\alpha_i} . \quad [4.32]$$

The thermal resistance of the tube wall is the standard one for a cylindrical tube of internal diameter d_i, and external diameter d_e , given by:

$$R_{wall} = \frac{\ln\left(\frac{d_e}{d_i}\right)}{2 \cdot \pi \cdot \lambda_w \cdot L} \quad [4.33]$$

where the λ_w is the thermal conductivity of the tube material, and L is the tube length.

Finally the coolant thermal resistance given by:

$$R_{coolant} = \frac{1}{\alpha_c} . \quad [4.34]$$

5 Simulation

In this chapter, the simulation software used in this work is described in detail. An analytical simulation, by using the software EES, as well as a numerical simulation, by using FLUENT, are carried out. A comparison of the simulation results with experimental data in order to validate the model is presented in chapter 7.

5.1 Simulation based on Empirical Correlations

The software EES (Engineering Equation Solver) was used to carry out the analytical simulation. The basic function provided by EES is the solution of a set of algebraic equations. EES provides many built-in mathematical and thermophysical property functions useful for engineering calculations. EES is particularly useful for design problems in which the effects of one or more parameters need to be determined.

5.1.1 Geometry

The geometry is presented in Figure 5.1.

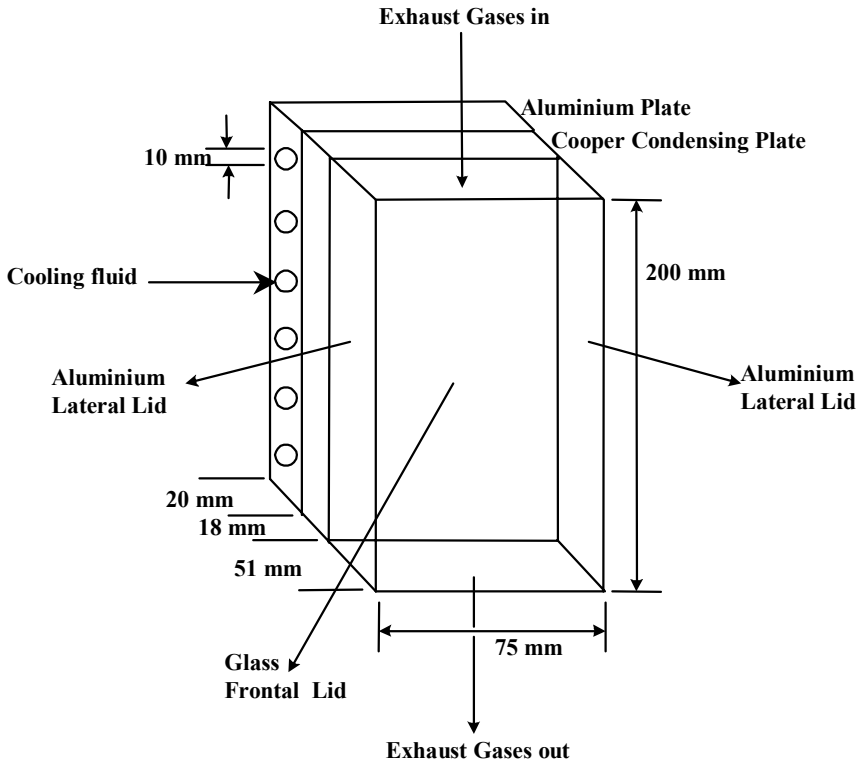

Figure 5.1 Geometry of the water-cooled plate with condensation

The plate is 200 mm long and 75 mm wide .Attached to the plate are three other walls so that the gases are flowing through a rectangular duct. The distance between the surface of the plate and the adjacent glass wall is 51mm.The glass wall serves as a window through which the condensation can be observed.

The exhaust gases flow downwards over the copper plate whereas the cooling fluid flows horizontally through the tubes placed in the aluminium plate as shown in Figure 6.2.

5.1.2 Assumptions

- The gas phase is considered as binary mixture of air and water vapor.
- Laminar flow and constant properties are assumed for the liquid film.
- The heat resistance due to the film is negligible as it contributes about 1-3 % in the total heat resistance [42]. Therefore, the condensation rate is obtained by the diffusion of the species in the gas phase.
- The condensation in the gas phase itself is negligible in comparison with the amount of condensate directly on the plate [42].
- The shear stress at the liquid-vapor interface is assumed to be negligible.
- The film originates at the top of the plate and flows downward under the influence of gravity.
- Momentum and energy transfers by advection in the condensate film are assumed to be negligible [6] due to the low velocities associated with the film
- A 2D simulation was carried out as the effect of the boundary layer at the edges of the duct in contact with the plate are not taken into consideration.

5.1.3 Boundary Conditions

In EES, the diagram window can be used in two ways. First, it provides a place to display graphic objects or text relating to the problem which is being solved. Second, the diagram window can be used for input and output of information. An example can be observed in Figure 5.2.

Some inputs variables such as combustion power, gas inlet temperature and excess air are required to run the simulation. If the combustion power is known, the mass flow of the exhaust gases can be obtained. The gas velocity is calculated in the plane orthogonal to the flow direction from the density of the gas mixture, the area of the rectangular duct and the mass flow of the exhaust gases.

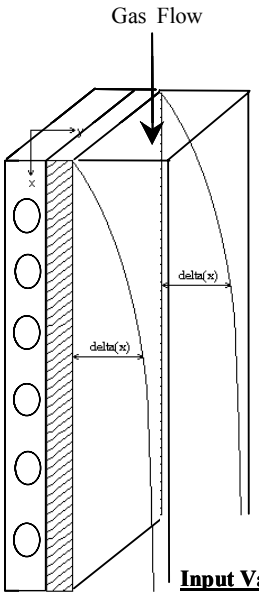

Input Variables

Combustion Power = 8 kW $T_{gas,inlet}$ = 125 °C Air Exceed = 1.2

Output Variables

Gas Flow	Heat/ Mass Transfer Coefficients	Heat Resistances
$v_{gas,inlet}$ = 1 m/s	α_{gas} = 8.54 W/m ^{2}K	$R_{gas,thermal}$ = 0.07
Re_{gas} = 2260	β_{gas} = 0.006 m/s	R_{Film} = 0.00017 m K/W
	α_{water} = 1400 W/m ^{2}K	delta (x) = 1 mm

Input Variables

$T_{surface}$ = 20 °C T_{sat} = 56 °C T_{film} = 20.2 °C

λ_{Alumin} = 290 W/m K

λ_{Copper} = 394 W/m K

Figure 5.2 Input and output variables in EES for a combustion power of 8 kW

The gas velocity, which determines the Reynolds number, varies with the combustion power.

In order to know if the gas flow is laminar or turbulent, the Reynolds number is taken into consideration. For a rectangular duct, the Reynolds number is based on the flow velocity, hydraulic diameter of the duct as characteristic length and the dynamic viscosity of the gas.

$$Re_{dh} = \frac{v\, d_h}{\nu} \qquad [5.1]$$

The Reynolds of the bulk flow has an influence in the boundary layer specially if it would be turbulent. In a high Re_{dh} flow, this layer is very thin, and in a low Re_{dh}, this layer becomes thicker. In case of the rectangular duct, if $Re_{dh} < 2300$, the flow is laminar and if $2300 < Re_{dh} < 10^4$, the flow is in the transition region.

For a combustion power of 8 kW and 12 kW, the flow is laminar as Reynolds is smaller than 2300. However, for a higher combustion power as 15 kW or 18 kW Reynolds is about 4300 and 5400. It means that the flow is not even turbulent. Thus, as mentioned in [5], if $Re_{dh} < 10^4$ the calculations can be carried out with the equations corresponding to laminar flow as described in chapter 4, because fully developed turbulent flow exists only for a Reynolds number above 10^4.

The flow is not hydrodynamic and thermal fully developed. In this case, the Nusselt number is calculated as the average Nusselt number for hydrodynamic and thermal fully developed flow (eq. 4.15) multiplied by a factor containing the Prandtl number and the parameter $X^+=L/d_h$ Pe with Pe as Peclet number [6]. As this factor takes a value near unity, the flow can be assumed as thermodynamic and thermal fully developed and therefore the Nusselt number is obtained by eq. 4.15. This calculation should be carry out as the discrepancies for the average Nusselt number are 5% for $1< Pr <\infty$ and they increase for $0,1 < Pr <1$ up to 10 %.

The Nusselt and Sherwood number and hence, the heat and mass transfer coefficient are then calculated depending on the Reynolds number (Re_{dh}) by the equations described in chapter 4. Once the heat transfer coefficients are known, the heat resistances can be obtained as mentioned also in chapter 4.

The surface temperatures and the heat flux are obtained from the energy balance:

- From gas to condensate

$$Q = (\alpha_g \xi)\, A_g\, (T_{avg,g} - T_i) + \dot{m}_{cond}\, h_{fg} \qquad [5.2]$$

- From condensate to wall

$$Q = \alpha_{cond}\, A_g\, (T_i - T_w) \qquad [5.3]$$

- From wall (gas side) to wall (water side)

$$Q = \lambda\, S\, (T_w - T_{wi}) \qquad [5.4]$$

with S as shape factor as described in equation 4.9.

- From wall to coolant side

$$Q = \alpha_c\, A_c\, (T_{wi} - (T_{c,o} + T_{c,i})/2) \qquad [5.5]$$

- In the coolant side

$$Q = \dot{m}_c\, C_{p,c}\, (T_{c,o} - T_{c,i}) \qquad [5.6]$$

To account for the temperature distribution in the longitudinal direction, the plate was divided into six segments. A one dimensional energy balance consisting of the equations shown above was applied at each of the seven nodes bordering the six segments. From the solution at each node a longitudinal temperature profile was generated.

The saturation temperature which depends on the content of water in the air is calculated as described in chapter 2.

The physical properties of the exhaust gases are obtained by polynomial equations depending on the temperature. The equations are presented in Appendix A.

Another important parameter to take into account is the binary diffusion coefficient which plays an important role in the mass transfer. It is calculated by the equation presented in Appendix D. Simulation results are presented in chapter 7.

5.2 CFD Simulation

FLUENT is a computer program for modelling fluid flow and heat transfer in complex geometries. It provides complete mesh flexibility, solving flow problems with unstructured meshes that can be generated about complex geometries with relative ease.

An advantage of FLUENT in comparison to EES program is that by using FLUENT a local temperature, velocity, mass fraction, condensation rate etc. distribution on the surface can be obtained. In addition to this, by the analytical solution an average value is assumed in the calculations, and it could happen that local condensation is already taking place for smaller values than the average one.

5.2.1 Simulation Software

The standard FLUENT interface cannot be programmed to anticipate every user´s needs. The use of User Defined Functions (UDFs), however, can enable to customize the FLUENT code to fit particular modelling needs. User-defined functions are written in the C programming language, and they are then implemented as compiled functions.

They can be used for a variety of applications as customization of boundary conditions, material property definitions, surface and volume reactions, source terms in FLUENT transport equations etc..

A species model is applied in a combination with a modified surface reaction. By default the Arrhenius rate equation is activated. By using the UDF, this Arrhenius model is replaced by the condensation model defined by the rate of diffusion of water, nitric acid, and sulfuric acid towards the cold surface. The rate of diffusion is described by eq. 4.21.

In order to access variables from the FLUENT solver the macros user-defined memories (UDM) are available. By these macros, solution variables can be accessed such as rate of condensate, velocity, temperature, mass fraction, dew point and pH-value.

In Figure 5.3, the inputs required in Fluent, in order to carry out the simulation, are represented:

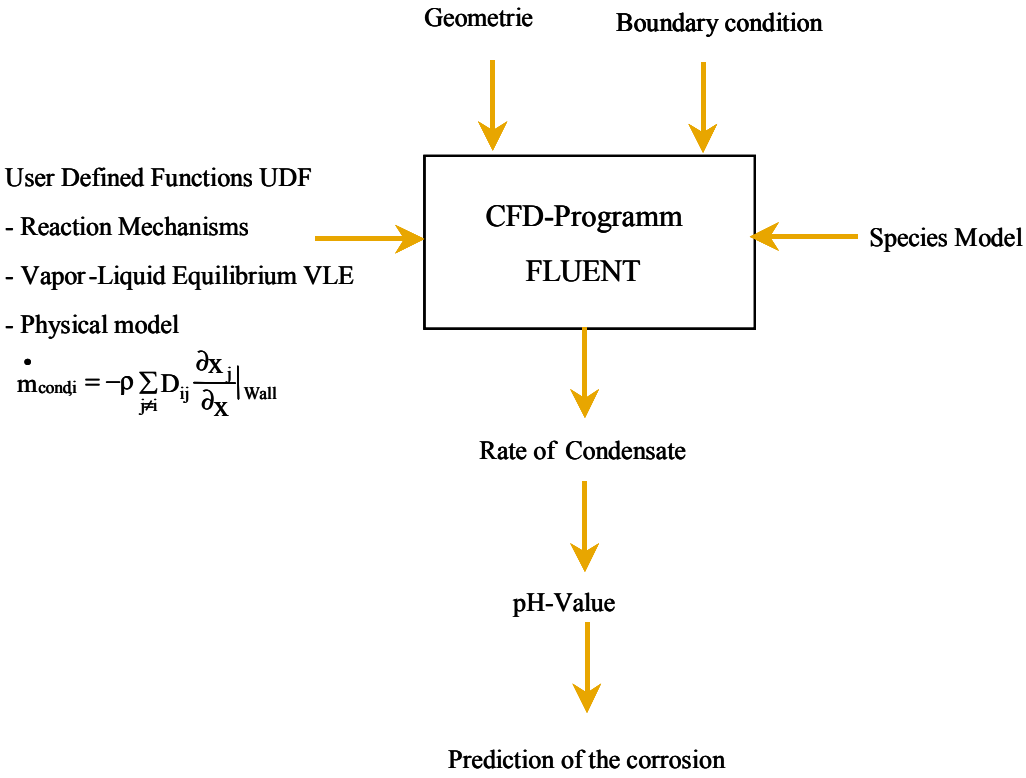

Figure 5.3 Schematic of the inputs required in FLUENT and some outputs

5.2.2 Simulation Model

5.2.2.1 Geometry

A 2D model is used to carry out the simulation of the condensation on a vertical water-cooled condensing plate. The gas mixture flows downwards over the condensing plate. A sample of the computational domain and grid is shown in Figure 5.4.

The computational mesh was generated using Map elements. In order to accurately resolve the solution fields in the vicinity of the surface of the plate, the mesh was refined at this point.

This mesh refinement was used to ensure an accurate resolution of the temperature, concentration and velocity gradients. The discretization scheme was second order accurate. A SIMPLEC velocity-pressure coupling multigrid solution procedure was used.

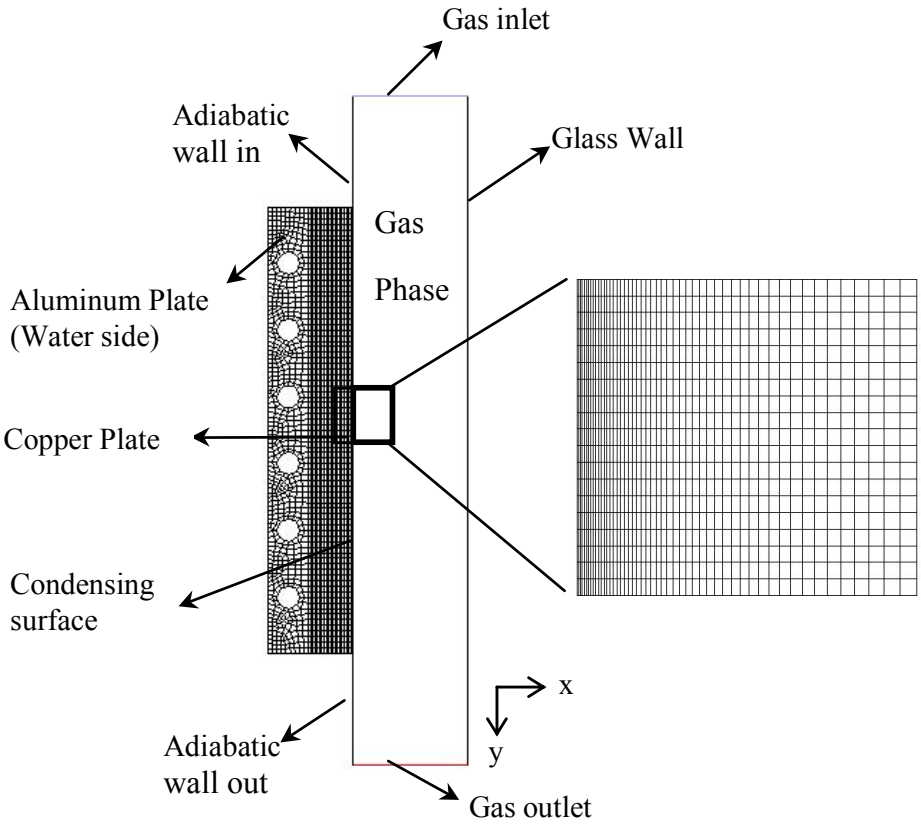

Figure 5.4 Computational domain and grid near the condensing plate

For the simulation, fine meshes of up to 8000 elements were used. The mesh near the plate surface was refined as it was mentioned above, and the cells are 2.4 mm high and 0.23 mm wide. The reason why this mesh refinement in this region is due to the accumulation of inert gases next to the wall giving a boundary layer through which the vapor must diffuse. The grid is fine enough near the wall to take into account the effect of this inert gas boundary layer in the condensation process

It is considered that condensation occurs at the surface of the condensing plate only. There is a 5 cm inlet section named “Adiabatic wall in” in Figure 5.4, so that a laminar velocity profile is developed before entering the condensing plate. And a 5cm outlet section named “Adiabatic wall out” in Figure 5.4 in order to take into account the back flow effects.

5.2.2.2 Conservation Equations

The governing equations for laminar flow are those of two-dimensional continuity, momentum, energy and conservation of species. These equations are given in chapter 3.

5.2.2.3 Discretization of the Conservation Equations

The general transport equations are non-linear differential equations, and they cannot be solved analytically. Therefore, they are discretized into algebraic equations

$$\underbrace{\frac{\partial}{\partial t}\int_V \rho\,\phi\,dV}_{\text{Unsteady}} + \underbrace{\int_V \rho\,\phi\,dV\,dA}_{\text{Convection}} = \underbrace{\oint_A \Gamma\,\nabla\phi\,dA}_{\text{Diffusion}} + \underbrace{\int_V S_\phi\,dV}_{\text{Generation}} \quad [5.1]$$

The equations were solved using FLUENT 6.1.22 FLUENT's *segregated method*, where the governing equations are solved sequentially. In that method, each discretized transport equation is linearized implicitly with respect to the equation's dependent variable. Because the equations are non-linear and coupled, iterations must be performed before a converged solution is obtained.

5.2.2.4 Assumptions

In order to carry out the calculations in an efficient way, a number of assumptions and simplifications are made:

- For the simulation, in case of combustion of methane only, a gas mixture of air, water vapor, nitric acid is considered. On the other hand, in case that combustion of methane with a certain amount of an odourant compound (C_3H_8S) takes place, a gas mixture of air, water vapor, nitiric acid and sulfuric acid is then considered. The intermediate reactions are not taken into account, because the inlet gas temperature is below the temperature at which the acids are completely formed (see chapter 2).

- The influence of the film in the condensation process is negligible. Analytical calculations of the heat resistances from the bulk gas mixture to the coolant were carried out with the EES program. The results show that the influence of the film in the total heat resistance is below 4 % (see chapter 7). According to [7] the influence on the heat resistance due to the film when it is laminar and in the presence of noncondensable gases is negligible and smaller than 5%.

- The condensation is assumed to take place on the surface of the condensing plate only. The condensation in the gas phase itself is negligible in comparison with the amount of condensate directly on the plate [42].

- The Reynolds number of the bulk flow Re_{dh} is assumed laminar for the reasons explained in this chapter in the section 5.1.3. The length of the plate plays also an important role in order to know if fully developed flow takes place. Some calculations have been carried out to obtain the required hydrodynamic entry length in order to know if fully developed laminar flow exits. This is described in more

detail in chapter 7, but as it was mentioned in section 5.1.3 the flow is not hydrodynamic and thermal fully developed.

- The influence of the gravitational forces are considered, but the surface forces are negligible.
- Diffusion in the flow direction y of the flow (c.f. Figure 5.4) is neglected, due to relatively high velocities.
- The physical properties of the species in the gas mixture, as density, viscosity, specific heat capacity and thermal conductivity, are given as a function of the temperature. Although, constant values could be taken due to the small temperature range (see Appendix A).
- The binary diffusion coefficients are obtained by eq 4.19.
- The diffusion coefficients in a multicomponent mixture are obtained depending on the binary diffusion coefficients, and the mass fraction of the components in the mixture by eq 4.20.
- The dew point of the ternary mixture H_2O, H_2SO_4 and HNO_3 is not considered in the simulation. It is assumed that above the dew point of the binary system HNO_3-H_2O (about 56 ºC, at p = 0.17 bar), water and sulfuric acid condense together. For a temperature near by this dew point, all sulfuric acid has almost condensed. And when the gas is cooled down below 60 ºC, the condensation of nitric acid and water takes place. It is to be mentioned that the dew point of the binary system H_2SO_4-H_2O is about 120 ºC at 0.17 bar.
- Both binary systems are azeotropic mixtures. Therefore, the liquid phase is considered as real by considering the activity coefficient calculated by a VLE model. The nonidealities of the mixture are manifested in deviations of the activity coefficient from unity (see chapter 2).

5.2.2.5 Boundary Conditions

First of all, a mesh-independent solution had to be ensured. So that, the mesh was checked at a certain condition by refining it as well as using local solution adaption features of the code. In performing the mesh refinement, two different models were taken into consideration, as the rate of condensation can be obtained either by the mass flux through the cell or by the diffusion rate equation (Fick´s law).

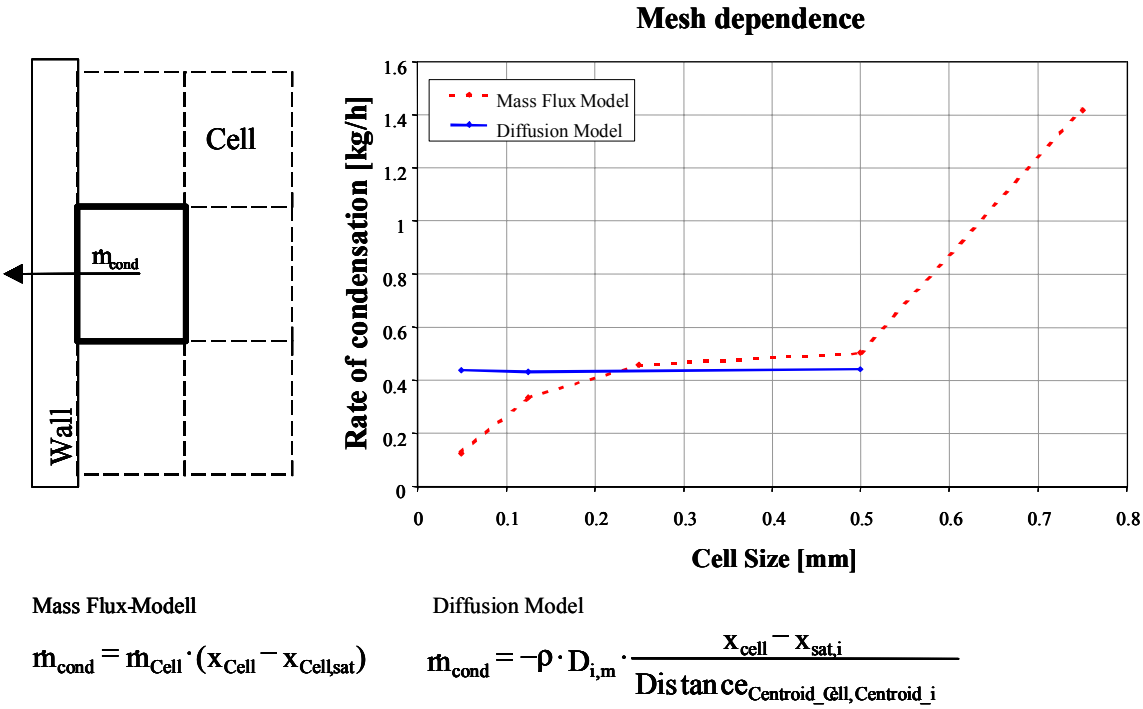

Mass Flux-Modell

$$\dot{m}_{cond} = \dot{m}_{Cell} \cdot (x_{Cell} - x_{Cell,sat})$$

Diffusion Model

$$\dot{m}_{cond} = -\rho \cdot D_{i,m} \cdot \frac{x_{cell} - x_{sat,i}}{Distance_{Centroid\_Cell,Centroid\_i}}$$

Figure 5.5 Mesh dependence by the Mass Flux model and Diffusion model

In the above figure, the rate of condensation $\dot{m}_{cond}$ is presented against the cell size. It can be observed that by the Diffusions model the condensation rate remains constant for all cell sizes, whereas by the mass flux model the condensation rate decreases by refining the mesh. For this reason, the Diffusion Model was considered in order to carry out the simulation for the condensation of the exhaust gases.

By the Mass Flux model, the problem is that the mass flux flowing through each cell is dependent on its size. The bigger the cell size is, the higher is the mass flux. This could be a problem by complexe geometries as the mesh drawing would be a big effort without knowing which mesh is the best one. By means of this variation with the cell size with this mass flux model, it can be said that the condensation process depends extremely on the diffusion of the species towards the wall.

Once the mesh-independent solution is ensured, the inputs required in Fluent have to be set. These inputs include definitions of the physical models, definitions of the boundary conditions associated with the condensing surface, definitions of the UDF and location of the compiled UDF.

Concerning the physical models, the species model in Fluent is activated, and the mixture species and surface reaction can then be specified. The UDF, where the diffusions model is programmed, is implemented in Fluent. The boundary conditions are next described in detail with help of Figure 5.4.

The Gas Phase is defined as fluid mixture containing nitric and sulfuric acid, water vapor and air. The physical properties of the components present in the mixture are calculated depending on the temperature as presented in Appendix A. However, the physical properties of the mixture are also obtained depending on the mixture composition. The diffusion coefficient is calculated by eq 4.20 depending of the individual $D_{ij,Maxwell}$.

In the Gas inlet zone, a velocity inlet is taken as boundary condition. But not only the velocity has to be set as input, even the gas inlet temperature and the corresponding vapor mass fractions of the components in the mixture (y_{hno3}, y_{h2so4}, y_{h2o}). The mass fraction of air will be automatically obtained by Fluent as difference from unity.

In the Gas outlet zone, a pressure outlet is chosen as boundary condition. In case of backflow, this effect will be taken into consideration and it will not have an influence in the results.

The two walls in the inlet and outlet section are defined as adiabatic walls. It means that the heat flux is equal zero. They are considered in order to get an uniform velocity profile at the top of the condensing plate, and to avoid an influence of the backflow in the simulation.

The copper plate and aluminium plate are as solid defined with a thermal conductivity of 394 W/mK and 230 W/mK, respectively. The values for the thermal conductivity are taken from [7].

The Glass window by which condensation can be observed is defined as wall in Fluent. As boundary condition the temperature at this wall is given. This temperature is measured in the test section to find out wether if it has an influence in the temperature boundary layer as shown in chapter 7.

Another zone to be taken into consideration is the copper plate, where the condensation model is to be applied. The boundary condition is set as a wall. In this zone, the surface temperature is defined as well as the reaction of phase change from gas to liquid of each condensing component in the mixture. The reactions are defined in Fluent with help of the species model, and they are described as follows:

$$H_2O\,(g) \xrightarrow{T<T_{sat}} H_2O\,(l) \qquad [5.7]$$

$$HNO_3\,(g) \xrightarrow{T<T_{sat}} HNO_3\,(l) \qquad [5.8]$$

$$H_2SO_4\,(g) \xrightarrow{T<T_{sat}} H_2SO_4\,(l)\,. \qquad [5.9]$$

When the surface temperature of the plate is below the dew point of the mixture in a certain location, condensation occurs. The diffusions model is applied to get the rate of condensation :

$$\dot{m}_{cond} = -\rho D_{i,m} \frac{x_{cell} - x_{sat,i}}{Distance_{centroid\_cell,centroid\_i}} . \qquad [5.10]$$

For a better understanding of the above equation represented in terms of Fluent, a simplified schematic in the boundary cell is shown below:

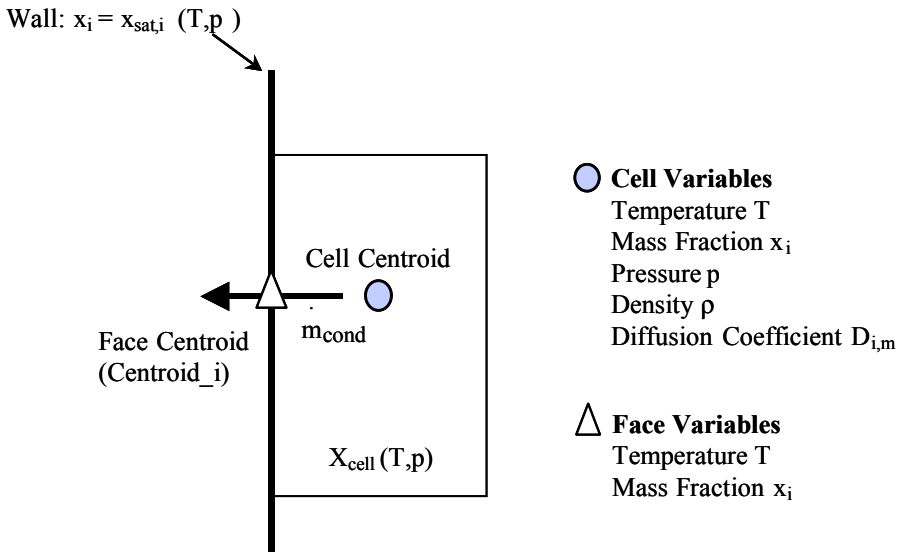

Figure 5.6 Schematic in the Boundary Cell at the surface of the plate

In Figure 5.6 can be observed that at the condensing surface the vapor mass fraction of the components x_i is set to a value corresponding to the saturation condition $x_{sat,i}$ for the temperature and mixture pressure at the wall. This is required because it is undesirable to compute the condensation rate where vapor exists at a temperature below its saturation temperature. Consequently, when the mass fraction in the cell next to the wall corresponds to the saturated condition, the rate of condensation is equal zero. On the other hand, when the mass fraction in the cell next to the wall is higher than the saturated condition, the condensation rate is not zero.

It is assumed that condensation occurs only on the wall, although possible condensation of the steam can take place on the water droplets and not reach then the water surface. This amount is negligible in comparison with the amount condensing directly on the surface [42].

As mentioned in the assumptions section in the present chapter, the dew point of the ternary mixture H_2O, H_2SO_4 and HNO_3 is not considered in the simulation. It is assumed that above the dew point of the binary system HNO_3-H_2O (c.f. Figure 5.7) (about 56 ºC, y_{hno3}=0.0009, at p = 0.17 bar), water and sulfuric acid condense together. The dew point of the binary system H_2SO_4-H_2O is 115 ºC at 0.17 bar (c.f. Figure 5.8)

for a sulfuric mass fraction of 3 10^{-6}. For a temperature close to the dew point of nitric acid and water system of 56 °C, all sulfuric acid present in the mixture has almost condensed.

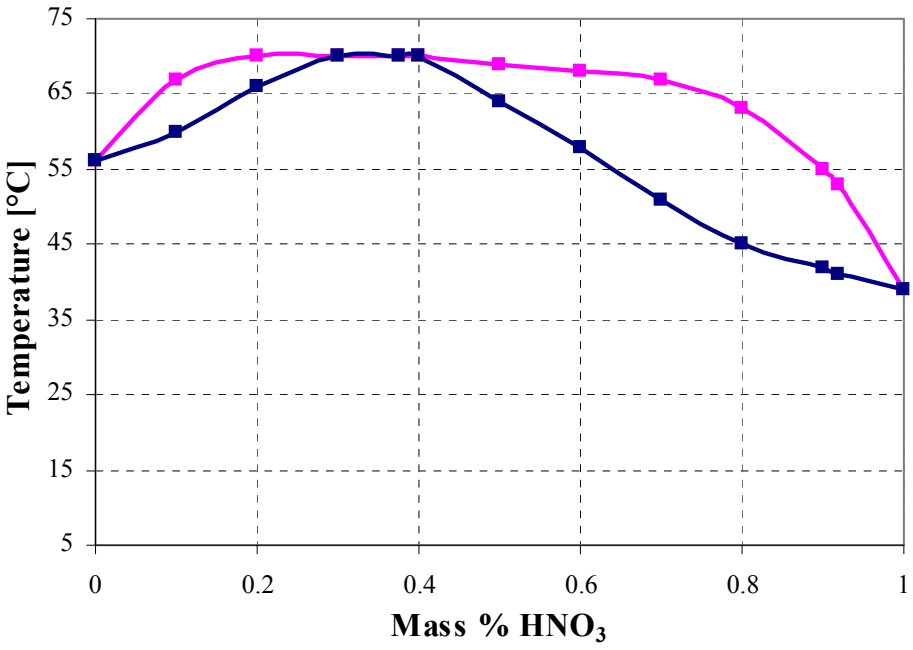

Figure 5.7 Phase equilibrium diagram for HNO_3-H_2O at $p_{hno3}+p_{h2o}$=0.17 bar

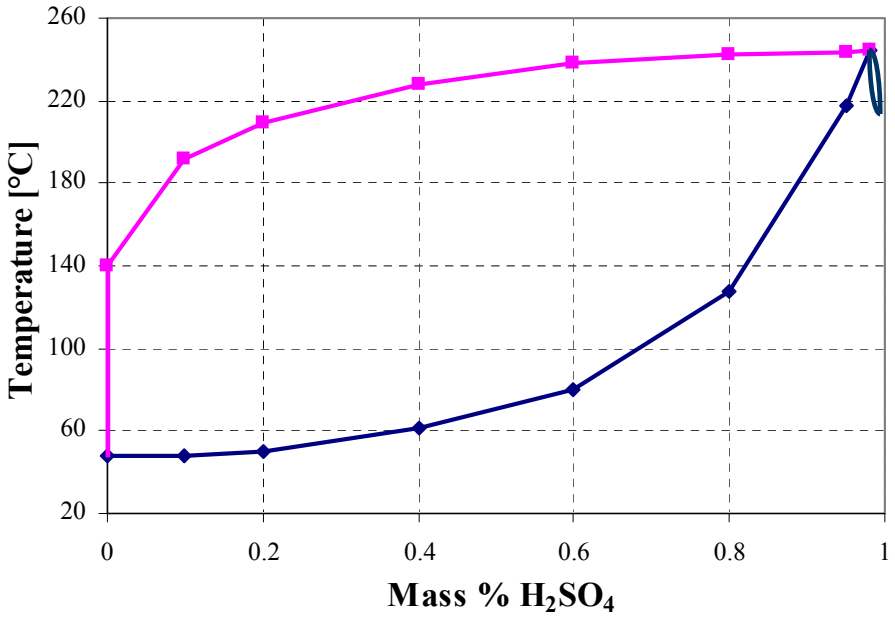

Figure 5.8 Phase equilibrium diagram for H_2SO_4-H_2O at $p_{h2so4}+p_{h2o}$=0.17 bar

When the gas is cooled down below 56 ºC, the condensation of nitric acid and water takes place. Both binary systems exhibit azeotropic condition in which the composition of a liquid mixture is equal to that of its equilibrium vapor. For such systems, the liquid phase is not an ideal solution, and the activity coefficients have to be estimated as described in chapter 2. It was found out that they have a relevant influence on the results, therefore they can not be neglected.

The temperature at the condensing surface is a decisive parameter for the condensation. And this temperature has to be then defined. In chapter 6, the test facility is described where it is explained that at the surface of the plate a temperature gradient is produced in the main flow direction. This is due to the heat coupled from the flange to the plate because of the heating in this region in order to avoid condensation in this location (see Figure 7.1)

In the simulation, there are two ways to consider the temperature profile at the wall. First, the heat flux transferred from the flange to the plate is known as the corresponding temperatures were measured by thermocouples located at the bottom of the flange and at the top of the plate. An insulated material with a thickness of 2 mm and a thermal conductivity of 0.2 W/m.K is situated in between. The heat flux can be calculated by conduction. This heat flux as well as the heat transfer coefficient in the water side can be set in Fluent. By coupling the copper plate (condensing surface) which is adjacent to the aluminium plate where water is flowing though, the corresponding temperature profile on the cooper plate for the different combustion power is reached. Second, the surface temperature was measured by means of eight thermocouples situated in different locations inside the cooper plate over the entire length in the main flow direction. The distance between these thermocouples and the surface of the cooper plate is 2 mm. The surface temperature was then estimated in order to know whether the measurements could be taken as values for the simulation. A maximal deviation of 0.1 K was estimated. Therefore, by adjusting the experimental data is quite easy to obtain a certain temperature profile depending on the length of the plate. The later option is taken into consideration because of its simplicity.

The measured temperature profiles are linear in the form:

$$T_w = C + m\,\text{Position}\ . \qquad [5.11]$$

The parameters C and m are presented in the table below, they represent the ordinate and slope respectively. T_w is the surface temperature in Kelvin, and the position varies from zero until 0.2 m corresponding to the length of the plate.

Table 5.1 Parameter of the temperature profile at the condensing plate for

$T_{avg,w}$ [K]	C	m
293	287.52	38
303	297.75	34
313	308.35	30
323	319.65	30

In Figure 5.9, the temperature profiles are plotted against the length of the plate for four different average surface temperatures $T_{avg,wall}$:

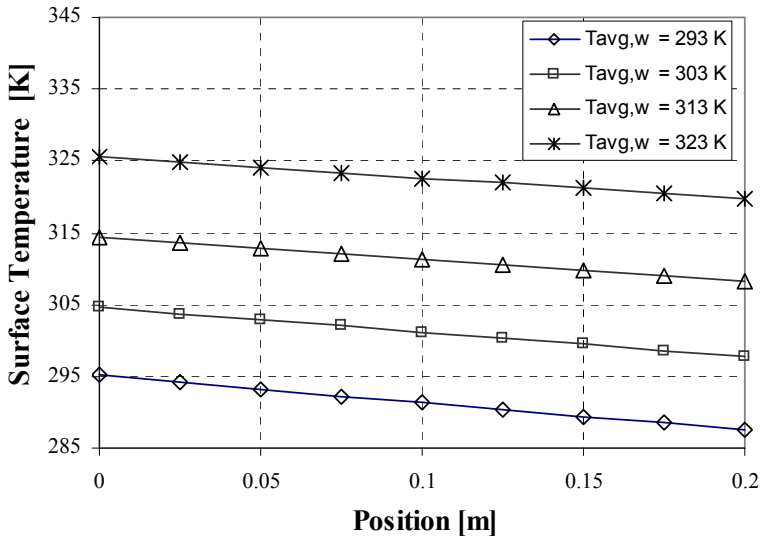

Figure 5.9 Measurements of the temperature profile at the surface of the water-cooled plate in order to consider them as boundary condition in the simulation

The position zero corresponds to the top of plate, it means immediately under the flange. And the position 0.2 m corresponds to the bottom of the plate.

For each combustion power in a range of 8-24 kW, the four temperature profiles were applied in order to make a comparison of the results depending on the power input. The experimental and simulation results are discussed in chapter 7.

A last important point to be presented in this section is the structure of the UDF where the condensation model is programmed:

- First, the values of density, pressure, temperature, mass fraction are read by existing macros in Fluent.

- The specific gas constant of the compounds in the mixture are defined as a constant, and the gas specific constant for the mixture can be obtained:

$$R_m = \sum y_i R_i \qquad [5.12]$$

- The partial pressure of the components is calculated in the form:

$$p_i = y_i \frac{R_i}{R_m} p \qquad [5.13]$$

- The activity coefficients γ_i are obtained by the Van Laar Model (see chapter 2) and the saturation pressure $p°_{sat,i}$ is obtained by the Antoine equation presented in Appendix A.

- Finally, by using Raoult´s law described in chapter 2, the saturated mass fraction is calculated, and a comparison between the $x_{sat,i}$ (c.f. Figure 5.6) and the mass fraction in the cell x_{cell} is done. In case that $x_{cell} > x_{sat,i}$ condensation takes place and the rate of condensation is obtained by the Fick´s law equation (chapter 4). In case that $x_{cell} < x_{sat,i}$ no condensation occurs, so the rate of condensation is set to zero.

A flux diagram of the structure of the program in the User-Defined Functions (UDF) can be observed in the figure below:

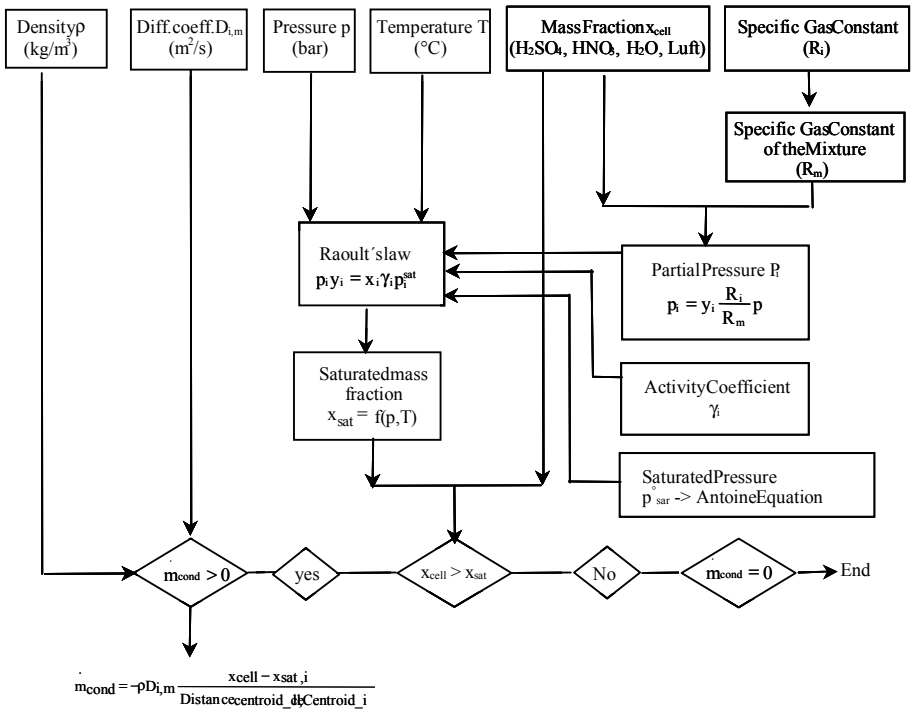

Figure 5.10 Structure of the UDF program

6 Experimental Equipment and Methods

The experimental rig and the operating procedure are described in this chapter. The experimental work was undertaken with the objective for validate the simulation model for the condensation of exhaust gases on a vertical cooled plate.

6.1 Test Facility

Figure 6.1 shows a schematic diagram of the test facility. Natural gas, composed by methane only or methane with an amount of 50 mg/m^3 of an odorant compound (C_3H_8S) containing sulfur, is supplied through a piping system. The gas flows then into a mixing chamber where it joins a flow of air. The flow rates are indicated on the flowmeters Q1 and Q2. The mixture enters then the combustion chamber or burner made of a stainless steel mesh. Two ignition electrodes are used for the ignition of the entering gas/air mixture to the burner. Due to the combustion process, exhaust gases are produced and pass to a shell and tube fin heat exchanger made of copper.

Condensation of the exhaust gases is not desired in this part of the test section because it could have an influence on the measurement of the mixture composition at the inlet of the test section, and consequently on the results of the analysis of the condensate. For this reason, a heating bath is integrated in the test facility in order to adjust the surface temperature by controlling the temperature of the cooling fluid flowing into the tubes of the fin heat exchanger. This bath is compatible with water, some types of oils and some alcohols. In case that the natural gas contains no sulfur on it, the dew point of the mixture is 56 ºC. So that, water can be used as cooling medium flowing into the tubes of the heat exchanger to reach surface temperatures above the dew point. On the other side, if the natural gas contains a certain amount of sulfur, the dew point of the mixture increases up to 115 ºC, and water can be only heated up to an average temperature about 85-90 ºC, above this temperature water boils. A SIL180 oil (Thermohaake GmbH) is used instead. The maximum working temperature of this oil is 180 ºC.

The exhaust gases leaving the fin heat exchanger flow through an aluminum flexible tube before entering the test section where the condensing plate is settled. This tube is heated up to 150-200 ºC by a heating band. At the bottom in the inner side of this aluminium flexible tube, there is a flow equalizer made of stainless steel. Next an insulated flange is integrated (Figure 7.1), so that a laminar velocity profile is reached before entering the test section. These both pieces are also warmed up to 150-200 ºC by heating bands. Indeed, the condensation process is to be avoided in the inner wall of the flexible tube as well as in the flange by these adjustable heating bands. An insulated

material with a thermal conductivity of 0.2 W/mK is used between the flange and the plate, nevertheless heat is transferred to the condensing plate (c.f. Figure 7.1). Consequently, a surface temperature gradient of about 5 K is produced on it in flow direction (c.f. Figure 5.9). In transversal direction, the gradient is maximum 0.05 K.

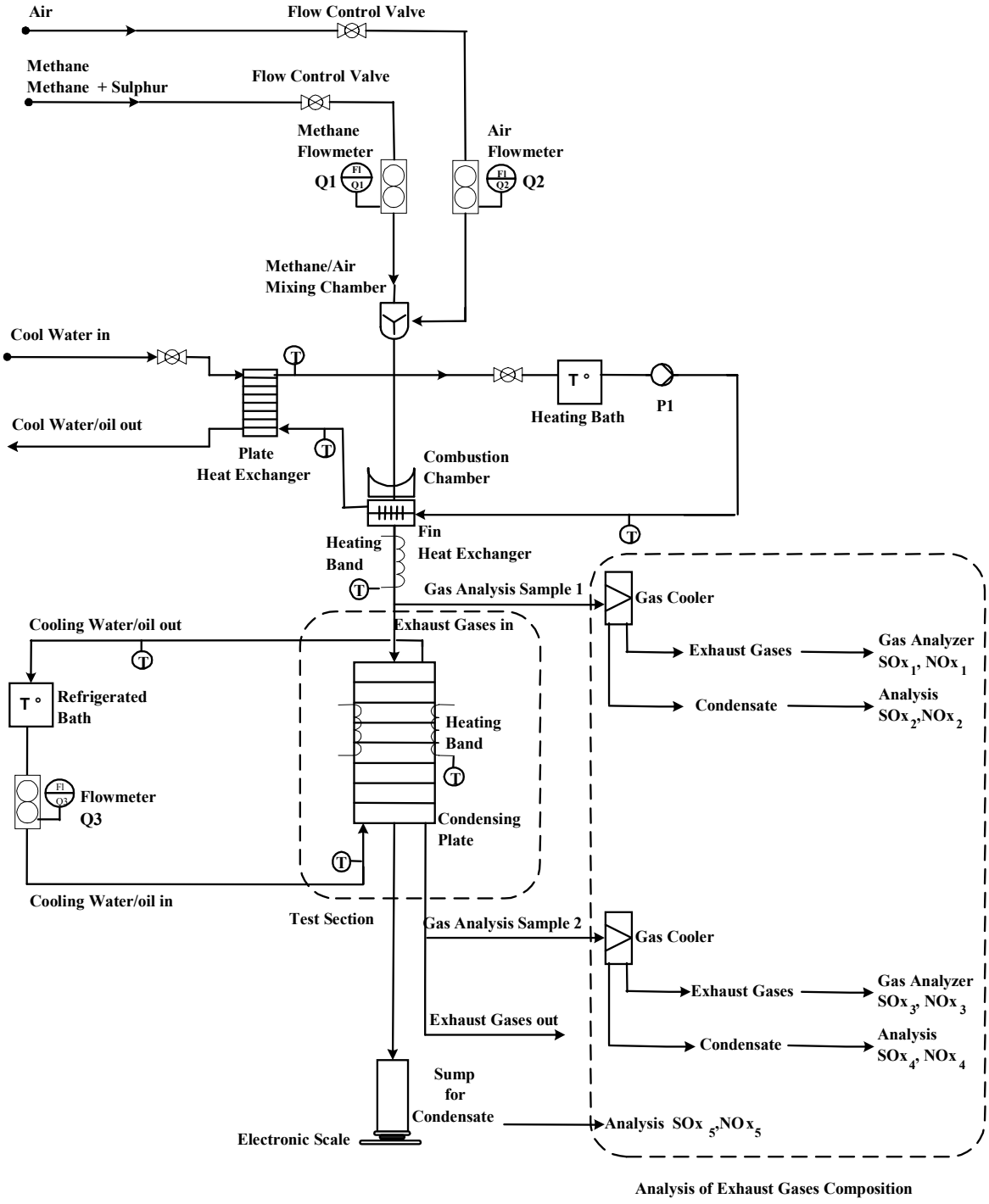

Figure 6.1 Schematic of the test facility

Figure 6.2 shows an schematic of the test section. It is a condensing plate made of copper (75 mm width, 200 mm height) mounted on an aluminium plate (c.f. Figure 5.1) where a conducting paste is put in between to insure good thermal contact. Water or oil flow is injected into the channel situated on the left hand side of the aluminium plate (c.f. Figure 6.2.a) and is forced to pass in parallel through six small tubes (10 mm diameter, 75 mm length) placed inside the aluminium plate and connected to this channel. The cooling fluid leaves the aluminium plate at the upper part of a second channel situated on the right hand side.

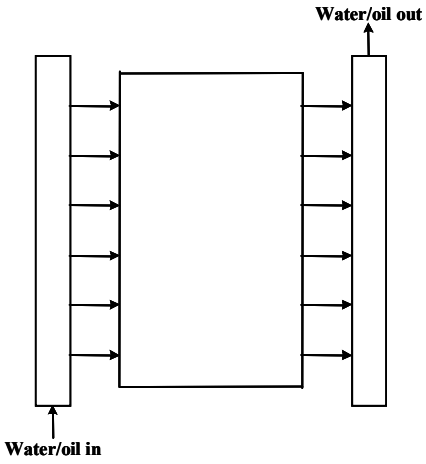

Figure 6.2. a Cool fluid distribution

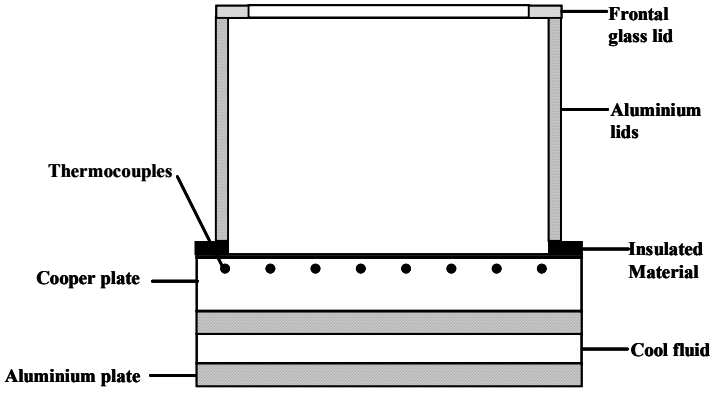

Figure 6.2.b Cut-off of the condensing device

This cooling water system enables the sub-cooling of the plate to be controlled by varying the cooling fluid flow rate and temperature independently. The temperature rise of the cooling water flow is measured by means of PT-100 situated at the entry and exit of the cooling fluid flow passage. Thus, knowing the rate of flow of the cooling fluid and its temperature rise the rate of heat transfer can be determined. The flow rate is indicated on the flowmeter Q3 (c.f. Figure 6.1).

The copper plate is the condensing surface, and it is firstly coated with a thin layer of nickel (3 μm) and then with one of gold (2 μm) in order to avoid possible corrosion due to condensation of acid gases. There are two aluminium lids at both sides of the copper plate of width 51 mm, and a frontal lid made of glass in order to allow the observation of the condensation process. The lids are heated up to 150-200 ºC by heating bands (c.f. Figure 6.2.b). Thus, condensation occurs on the copper plate surface only. The wall temperature on the cooper plate is measured with 8 thermocouples (1 mm diameter) inserted inside the cooper plate. A refrigerated bath is placed nearby this condensing plate for adjusting the surface temperature by controlling the temperature of the cool fluid.

The condensing plate has an arrangement which allows its orientation to be varied. But experiments were only carried out with the vertically arranged plate. With the plate horizontal, condensate is not able to drain from the plate.

The gas/air mixture enters the test section and flows downwards over the condensing plate. A balance of the mass of exhaust gases (NO_x, SO_x) is carried out in order to take this parameter as boundary condition for the simulation.

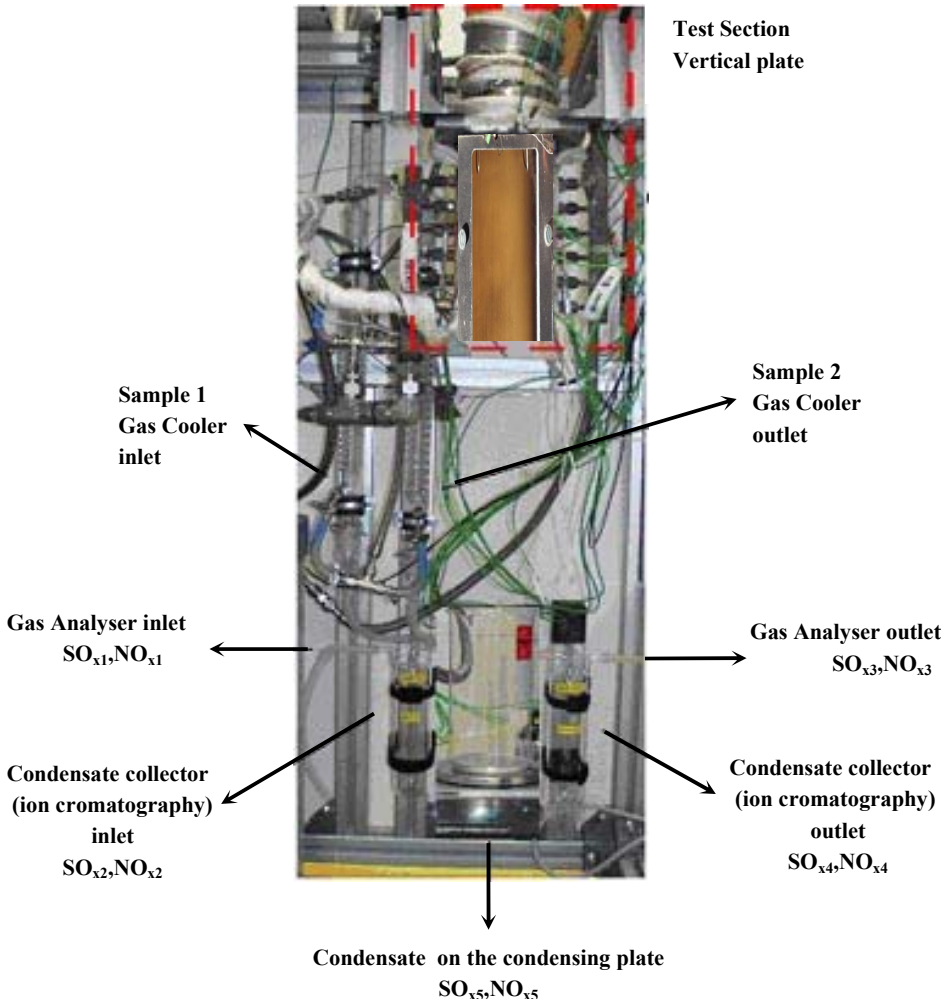

Figure 6.3 Analyses of exhaust gases and test section

At the entry, a gas sample (cf. Figure 6.3) is taken and passes through a cooler where it condenses partially. The condensate composition (NO_{x2}, SO_{x2}) is analysed by ionic chromatography and the gas is led directly to a gas analyser (NO_{x1}, SO_{x1}). The addition of both analyses results gives the total composition of NO_x and SO_x at the entering test section. The same procedure is carried out at the outlet of the test section, the concentration of the nitrogen oxide and sulphur oxide is analysed (NO_{x3}, SO_{x3}, NO_{x4}, SO_{x4}). The condensate on the condensing plate is analysed as well (NO_{x5}, SO_{x5}). The addition of these quantities (index 3,4) at the exit and on the plate (index 5) should be

the same as at the entry (index 1,2), so that the balance is fulfilled. The two coolers are required to reduce the temperature of the gas to below 50 °C, as the gas analyser supports a maximal temperature of 50 °C.

On the base of the test section there is one condensate collector that catches condensate which falls from the condensing plate. The rate at which condensate is produced on the plate can be determined from measurements of the weight of the sump by a known period of time of 30 minutes. A computer-based system consisting of a 18 channel scanner and a precision digital voltmeter is used for signal monitoring. A LabView program is used for data acquisition.

6.2 Measurement Techniques

6.2.1 Temperature

Temperatures were measured by type K (Chromel-Alumel) stainless steel sheathed thermocouples (THERMOCOAX GmbH). All thermocouples were 1 mm in diameter and 100 mm in length. Electrical connections were made by compensated plugs and shielded compensated thermocouple leads.

6.2.2 Heating Bands

All parts where the condensation had to be avoided were heated up by heating bands type HSS (HORST GmbH). They are made of a very flexible glass-yarn-insulated heating cable, and it allows a usage even in places where very small winding radius are required. This type of heating tape has an Additional Protective Braid.

6.2.3 Heating and Refrigerated Bath/Circulator

In order to adjust the temperature of the fluid flowing into the tubes of the condensing plate and the fin heat exchanger, a HAAKE Model F3-C heating/refrigerated bath (Thermohaake GmbH) was installed. Bath capacity is 5L, pumping capacity 16 L/min, heater: 1000 W. The temperature range is -20 to +150 ° C.

Water can be used as bath liquid until temperatures up to 80-85 °C. Above this temperature SIL180 (Thermoelektron GmbH) is used. The properties of this oil are summarized in 6.2.4.

6.2.4 SIL180 Synthetic Bath Liquid

SIL180 (Thermohaake GmbH) is an oil to reach surface temperature in the heat exchanger above 120 °C in order to avoid the condensation. The working temperature

range is –40/200 °C. Although other bath liquids were compatible with the HAAKE F3-C Model, they were not good enough because either the working temperature range was not valid or they were corrosive to the material of the bath.

6.2.5 Gas Flow Rate

The gas flow was measured by an EL-FLOW mass flowmeter/controller type F-2023AC-FA-44V for air, and type F202AC-FA-44V for methane (BRONKHORST GmbH). The maximal air flow is 36 m^3N/h and the maximal methane flow is 3 m^3N/h. The uncertainty is presented in 6.4.

6.2.6 Liquid Flow Rate

For the water/oil flow measurement an electromagnetic flowmeter MAGFLO® (Danfoss GmbH) was used. The converter type is MAG3000. The sensor type is MAG1100 and the temperature range is –20 to 200 °C. The uncertainty is presented in 6.4.

6.2.7 Gas Analyzer

In this investigation the exhaust gas concentration was measured by an ULTRAMAT 23® gas analyzer (SIEMENS AG) . It is suitable for the continuous measurement of concentrations of gases, such as CO, CO_2, NO, SO_2, CH_4 among other ones. Up to three of these components plus oxygen (O_2) can be measured simultaneously by this analyzer. The sample gas temperature ranges from 0 to 50 °C. Concentration range: 0-250 mg/m^3 CO, 0-400 mg/m^3 NO, 0-400 mg/m^3 SO_2. Accuracy < 2 %.

Two samples were taken in the test facility (c.f. Figure 6.1), one at the inlet of the test section and the other one at the outlet. As it was described, the samples condense partially, so that the remaining gas is led directly to this gas analyzer.

6.3 Experimental Procedures

6.3.1 Preparation of the Plate Surface

The surface of the copper plate was treated in order to get more accurate results in the analysis of the mixture composition. The procedure is described in the appendix B. This treatment avoids the oxidation of the plate surface due to the acids and, hence, a wrong measurement of the exhaust gases concentration.

6.3.2 Operating Procedure

Firstly, the refrigerated bath and heating bath are filled with the cooling fluid. It can be either water or thermal oil SIL180 (Thermohaake GmbH). The cooling fluid flow rate in the fin heat exchanger situated after the combustion chamber was adjusted to keep the surface temperature above the dew point avoiding therefore condensation in this part of the test rig. Also, the cooling fluid flow rate in the test section was adjusted to keep a constant temperature at the surface of the condensing plate. This surface temperature was set to a value below the dew point of the mixture in order to promote condensation.

When combustion of pure methane occurs, the dew point of the exhaust gas mixture is 56 °C, and surfaces temperature above this point are to be reached by circulating water into the tubes of the fin heat exchanger. But when combustion of methane with an amount of 50 mg/m^3 of an odorant compound containing sulphur occurs, the dew point increases up to 115 °C approximately, and therefore water is replaced by thermal oil SIL180 in order to reach surfaces temperatures in the fin heat exchanger above 120 °C.

Secondly, heating bands were switched on and set up to a temperature above 150 °C in order to make sure that the surface temperatures, where the heating bands were situated, were above the dew point of the mixture. These bands were manually adjusted.

When the temperature of the condensing plate surface and heating bands changed less than 0.05 K/min, the test facility was ready to start with the measurements. Average surface temperatures of 20 °C, 30 °C, 40 °C and 50 °C were set on the condensing plate for a combustion power of 8 kW, 12 kW, 15 kW and 18 kW in case that pure methane was introduced to the system. Average surface temperatures of 30 °C and 40 °C were set if methane with an amount of sulphur was introduced instead. But in this case, the measurements were only carried out for a combustion power of 8 kW. A heat flux of 8 kW-18 kW covers the range of typically applied values in gas condensing boilers.

Methane and air were introduced to a mixing chamber. The flow rate ratio between methane and air (see chapter 2) was adjusted over a control element in the program LabView. Once the desired conditions were chosen, the mixture entered the combustion chamber, where the ignition took place due to two ignition electrodes. A constant value of 1.2 for the excess of oxygen was taken and the combustion process was fully completed.

The exhaust gases leaving the combustion chamber reached temperatures of 1500 °C. They passed to a shell and tube fin heat exchanger where they were cooled down to temperatures above the dew point of the mixture depending on the combustion power

(cf. Figure 6.4). Next, they flowed through a flexible tube of 50 cm length before entering the test section where the condensing plate is situated.

When thermal oil SIL 180 was used as cooling fluid flowing into the tubes of the fin heat exchanger, an additional plate heat exchanger (cf. Figure 6.1) had to be installed in order to make sure that the temperature of the thermal oil did not exceed 180 °C. This is the maximal working temperature for the oil. Three thermocouples were established in this part of the test facility: 1) at the inlet of the fin heat exchanger, the temperature should be higher than the dew point which is 115 °C, 2) at the outlet, it should not exceed 180 °C and 3) after the additional plate heat exchanger in order to control that the cooling is good enough. Because the difference between the dew point of the mixture and the maximal working temperature of the thermal oil is small, there was a limitation on the measurements when the combustion of methane containing sulphur was desired. For a heating power of 8 kW, the temperature at the outlet of the fin heat exchanger was already 165-170 °C. Therefore, measurements for higher heating power were not possible.

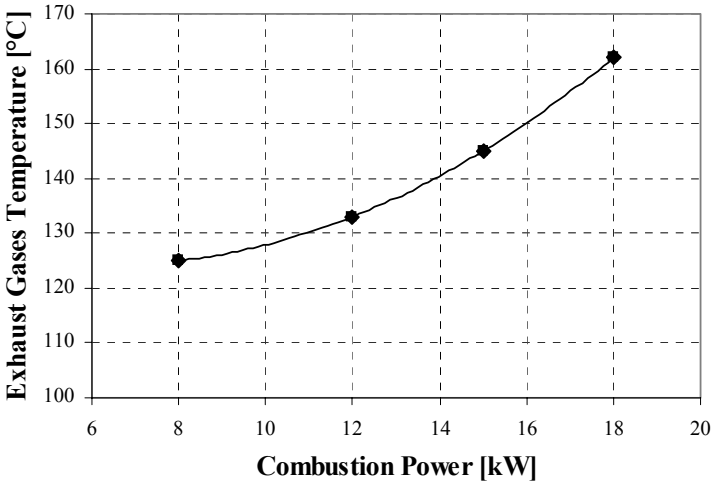

Figure 6.4 Exhaust gases temperature at the entry of the test section

Under steady state conditions, it was assumed that the surface temperature changed less than 0.1 K/min, the inlet gas temperature of the condensing plate less than 0,5 K/min, and inlet water temperature less than 0.01 K/min. It took about an hour approximately until the steady state was reached.

When steady conditions had been achieved the rate of heat transfer was determined. Firstly, condensate from the condensing plate was collected over a period of time of 30 minutes and weighted. The latent heat transfer could then be determined knowing the latent heat of the vapor. Secondly, the cooling water temperatures at inlet and outlet of the condensing plate cooling water passage were measured by means of PT-100

installed at those locations. The flow rate of cooling water was measured using a flow meter Q3 (c.f. Figure 6.1). Then the total rate heat transfer was calculated from the product of the mass flow rate of cooling water, the specific heat capacity of the cooling water and the temperature rise of the cooling water. The difference between the total rate heat transfer and the latent heat transfer gives the sensible heat transfer. An error analysis for the measurements is presented in 6.4.

As it was mentioned, the combustion power was varied in a range 8 kW-18 kW to give gas flow rates of 3.44 g/s, 6.44 g/s and 7.44 g/s. Measurements of condensation rate and exhaust gases composition were made by supplying mixtures of pure methane/air, and also methane/air with an amount of 50 mg/m^3 of merchaptane (C_3H_8S). With the exhaust gases flowing downwards over the condensing plate, droplets of condensate formed very rapidly at many points on the surfaces and coalesced to form rivulets. These ran off the plate quickly leaving the surface clear so that further dropwise condensation could occur. The process was repeated all over the surface in a very dynamic manner.

Figure 6.5 shows the droplets formed on the water-cooled plate in a vertical orientation for a combustion power of 8 kW:

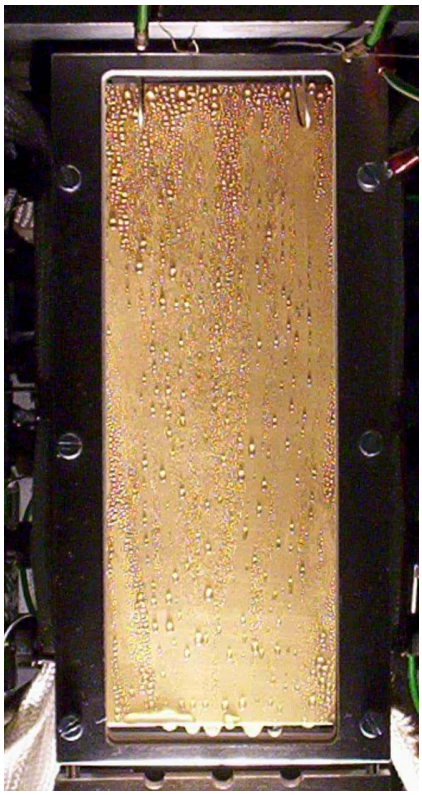

Figure 6.5 Dropwise condensation on the gold coated cooper plate

The rate of condensation $\dot{m}_{cond}$ is plotted in Figure 6.6 against the combustion power for an average surface temperature of 40 °C.

It was tested by other authors (J.D.Jackson and M. Ahmadinedad [38]) that with a horizontally arranged plate condensate could not drain readily from the upper surface and much of it was covered by liquid for much of the time. Droplets of condensate formed and detached from time to time at various places. As a consequence of the poor drainage of condensate from the plate and the thermal resistance of the liquid on the surfaces, heat transfer was greatly inhibited. Therefore, measurements were not carried out with an horizontal orientation of the plate.

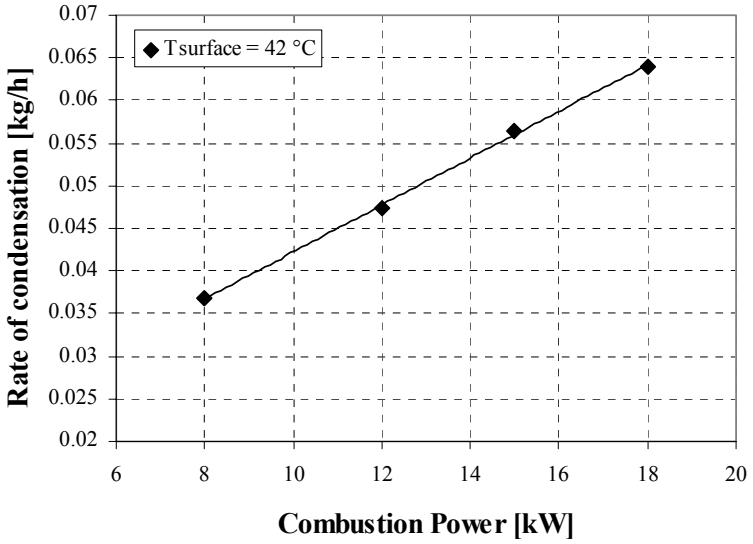

Figure 6.6 Rate of condensation on a vertical condensing plate

Experiments were also performed to establish the accuracy with which the dew point of the mixture was assumed in the simulation. This one was calculated by a Vapor-Liquid Equilibrium model as described in chapter 2. As reference temperature the calculated dew point was taken. The surface temperature was firstly set some degrees Celsius above this value. Then, it was reduced until condensation on the plate was observed as shown in Figure 6.7. In case that a mixture of pure methane/air was supplied the experimental dew point was obtained at about 55 ºC whereas the calculated temperature is 56 ºC. For a mixture of methane/merchaptane/air, the dew point is 115 ºC, but it was not possible to observe condensation when the surface temperature was set to this value. The explanation for this fact is that the amount of sulphuric acid (0.0004 %) contained in the gas mixture is very small compared to the amount of air (88 %) and steam (11.4 %) and it was impossible to observe the condensation of sulphuric acid at a first glance. Consequently, it was assumed that the calculated dew point by a VLE model was good enough, as it was verified from the literature [48].

A last point to be addressed is the measurement of the mass of exhaust gases in order to consider them as boundary condition for the simulation. As it was mentioned in the present chapter, a balance of the exhaust gases composition was carried out (cf. Figure 6.3). The mass that was measured at the inlet of the test section had to be equal to the addition of the mass measured at the outlet of the test section and the amount of condensate in order to fulfil the balance. In chapter 7, this will be described in more detail.

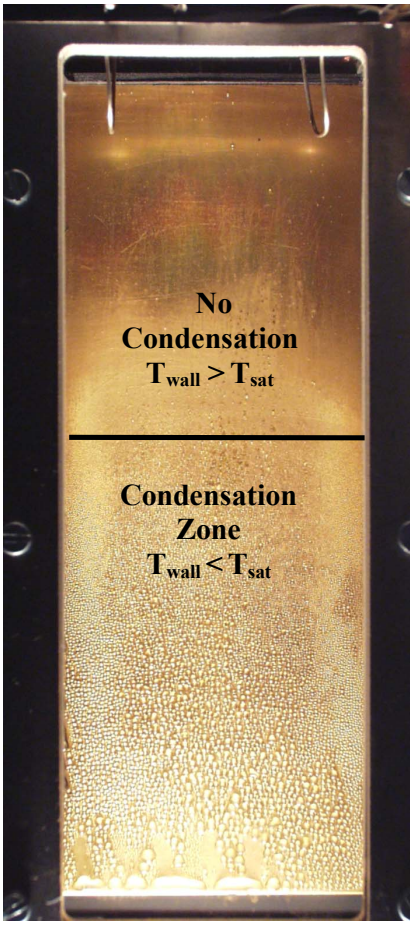

Figure 6.7 Effect of the surface temperature on the condensation process. When the surface temperature is smaller than the saturation temperature of 56 °C, condensation occurs (below). When the surface temperature is higher than the saturation temperature, condensation does not occur (above)

6.4 Experimental Error and Uncertainty

The Moffat method [53] was used for the uncertainty analysis of the measurements. A detailed description of the calculation procedure is presented in Appendix C. The estimation of the uncertainty associated with the most important individual variables

will be given. These variables are the ones which have to be taken into consideration to carry out the simulation. In the following paragraphs details on the estimation of the uncertainty of the variables are given:

- Inlet and outlet gas temperature $T_{g,in}$, $T_{g,out}$: The systematic error associated with the temperature measurement by thermocouples could be deduced by calibration. The standard deviation of the measurements was ± 0.5 K. The systematic error had to be estimated from the manufacturer's claim of uncertainty of the calibration apparatus: ± 0.3 K.

- Water flow rate $\dot{V}$: The systematic uncertainty is given by the manufacturer´s specification ± 0.5 l/h and the random error is ± 4 l/h.

- Water temperature T_{water}: The random error associated with the temperature measurement by resistence thermometers PT100 class A was ± 0.01 K. The systematic error was estimated by the manufacturer to be ± 0.3 K.

- Surface temperature T_{wall}: The measurement of this temperature is very important as it determines condensation. This was taken as parameter in the simulation. The deviation of measurements was ± 0.1 K and the systematic error was ± 0.3 K.

- Total condensate rate $\dot{m}_{cond}$: The amount of condensate on the surface of the plate was weighted on a scale, therefore the systematic error was estimated by the manufacturer ± 0.035 g.

- Concentration of sulphuric acid in the exhaust gas x_{h2so4} and condensate rate $\dot{m}_{cond,h2so4}$: The mass fraction of the components present in the gas mixture is required as input parameter in the simulation. Therefore a balance of the composition of sulphuric acid was carried out. An analysis of the condensate was done by chromatography and the systematic error was ± 1 ppm. In addition to this analysis, a gas analyser was also used as described in chapter 6 and the error was ± 1ppm.

- Concentration of nitric acid in the exhaust gas x_{hno3} and condensate rate $\dot{m}_{cond,hno3}$: As for the sulphuric acid, a systematic error due to the chromatography was ± 3 ppm and the error estimated by the manufacturer for the gas analyser was ± 1 ppm.

The results of the analysis of uncertainty are presented in the Table C.1 in Appendix C.

7 Experimental and Simulation Results

In the previous chapters, the simulation model has been described in detail as well as the experimental test rig and how the experiments were performed. The aim of the present chapter is the discussion of the experimental and simulation results.

7.1 Heat and Mass Transfer

7.1.1 Rate of Heat Transfer

As described in chapter 5, the heat transfer from the gas to the condensate is expressed in the form:

$$Q = Q_{sensible} + Q_{latent} = \alpha_g \, A_g \, (T_{avg,g} - T_w) + \dot{m}_{cond} \, h_{fg} \qquad [7.1]$$

where α_g is the heat transfer coefficient in the gas phase and h_{fg} the latent heat of vaporization.

However, another sources of heat must be considered in the former equation. The heat flux coming from the flange situated before the entering test section as described in chapter 6 and the heat loss through the glass. An insulated material is located between the flange and the condensing plate as it is shown in Figure 7.1. Nevertheless, heat is transferred to the plate, and this has to be considered in the eq 1.1 together with the heat loss through the glass by which the condensation can be observed:

$$Q = \alpha_g \, A_g \, (T_{avg,g} - T_w) + \dot{m}_{cond} \, h_{fg} + C_1 \Delta T_{fl} - Q_{glass} \, . \qquad [7.2]$$

The third term corresponds to the heat flow rate of the flange where ΔT_{fl} is the temperature difference in the flange and $C_1 = \lambda_{fl} A / s_{fl}$ taking a constant value of 1.78 W/K. Both parameters were obtained experimentally. The fourth term corresponds to the heat loss through the glass. The heat loss through the glass Q_{glass} is given by the measured temperature of the glass and the free convection in the atmospheric air. This represents maximum 3 % of the total heat flux Q. Consequently, it can be neglected.

All heat that is transferred from gas mixture to the condensate and the heat from the flange must be then conducted through the plate, and is finally removed by the coolant, which is flowing on the other side of the condensing plate:

$$Q = \dot{m}_c \, C_{p,c} \, (T_{c,o} - T_{c,i}) \qquad [7.3]$$

The rate at which heat was removed by cooling water flowing through the tubes within the plate could be determined by knowing the flow rate of the cooling water, the specific heat capacity and the temperature rise of the cooling water. On the other side, the condensation rate could be determined by collecting condensate over a known period of time of 30 minutes and weighing it. Then, the sensible heat could be obtained by the difference between the total heat flow rate Q, the latent heat Q_{latent}, and the heat flow rate from the flange Q_{flange}. The energy balance is then fulfilled.

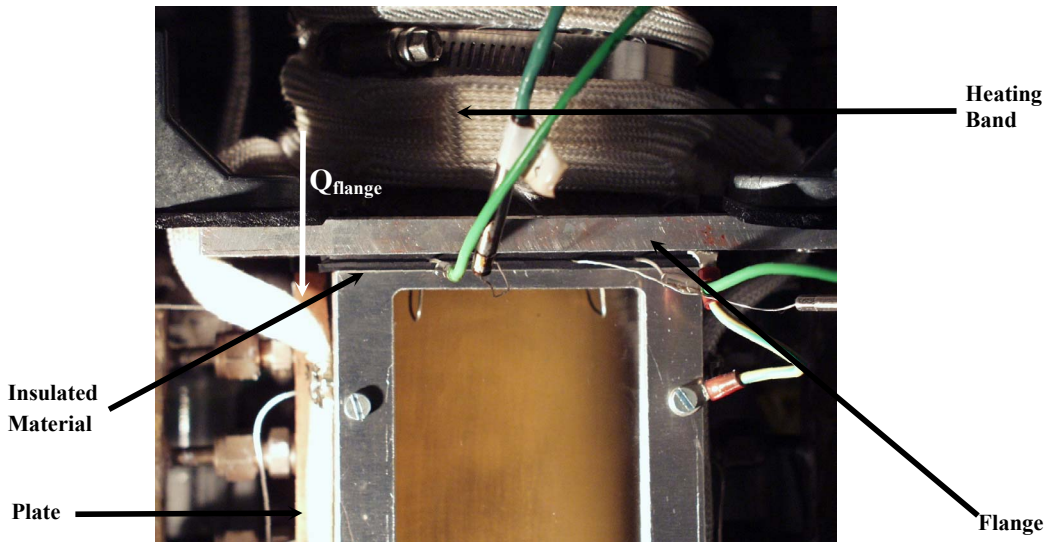

Figure 7.1 Enlarged view of the flange situated at the top of the test section (Plate)

A set of experiments was completed in which the heat flow rate Q from a mixture of water vapor, nitric acid, sulfuric acid and air in varying combustion power was measured as a function of the plate subcooling $\Delta T = T_g - T_{sat}$. In Figure 7.2, the rate of heat transfer against plate subcooling ΔT for different combustion powers is plotted.

The cooling fluid flow was kept constant with a value of 192 l/h, but its temperature in the test section was adjusted to keep a constant temperature profile at the surface of the condensing plate for different power inputs. This surface temperature was set to a value below the dew point of the mixture 56 ºC in order to promote condensation. Firstly, a surface temperature about 20 ºC was set up, and it was increased until a temperature about 50 ºC near to the dew point being able to observe the effect of the subcooling on the amount of condensate, and consequently on the heat transfer, as it is shown in Figure 7.2. The smaller the surface temperature, the higher the temperature difference between cold coolant and hot gas mixture, therefore there is an increase of heat flow rate from the gas to coolant.

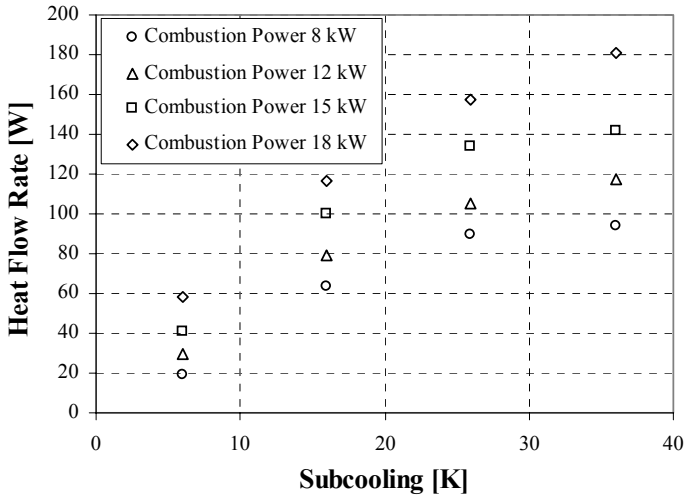

Figure 7.2 Effect of subcooling ($T_g - T_{sat}$) on the heat flow rate for several gas flow rates 3.44 g/s for 8 kW, 5.44 g/s for 12 kW, 6.44 g/s for 15 kW and 7.44 g/s for 18 kW

By a comparison of the heat transfer for several combustion powers corresponding to the same surface temperature (cf. Figure 7.2), it can be observed that the heat transfer rate continues to increase as the combustion power is raised. An explanation for this is the buildup of the inertgas boundary layer at the surface of the plate. When a combustion power of 8 kW is supplied, the gas velocity is small and consequently a thick inertgas boundary layer is built near the wall. It results in a worse heat and mass transfer. Whereas for higher combustion powers, higher velocities are reached and a thin boundary layer is built, therefore a better heat and mass transfer. The components can diffuse easily through the boundary layer towards the wall.

Another point to be addressed is that by increasing the gas velocity the vapor flow might change from laminar to turbulent, resulting in an increase of the mass and heat transfer rate. But the vapor flow is not even fully developed laminar for the highest combustion power of 18 kW. The plate length L is sufficiently short such that turbulent flow is never triggered. This will be discussed in more detail in the section 7.2.1.

7.1.2 Heat Transfer and Mass Transfer Coefficient

The most important magnitudes for heat and mass transfer processes is the heat transfer coefficient α and mass transfer coefficient β. They depend on conditions in the boundary layer, which are influenced by surface geometry, the nature of the fluid motion, and an assortment of fluid thermodynamic and transport properties.

As the boundary layer thickness grows in the flow direction (see Figure 7.3), the fluid mechanics change significantly, so that the convective heat transfer coefficient varies along the length of the plate having a local convective heat transfer coeffcient α_x.

However, it varies not only due to the boundary layer but also due to the linear temperature profile at the plate as described in chapter 5 (c.f. Figure 5.9).

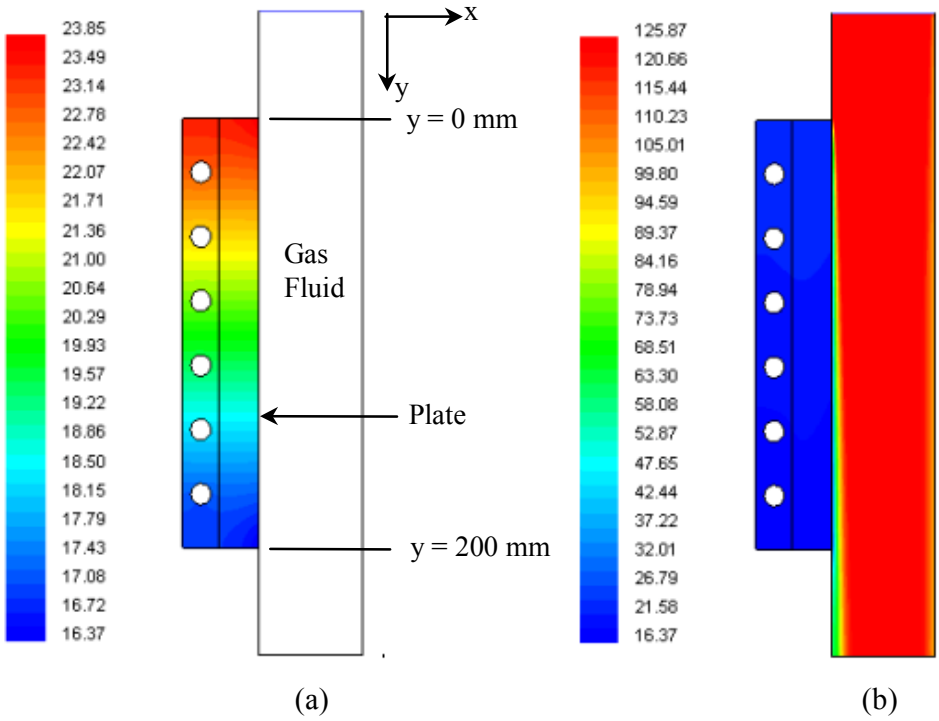

Figure 7.3 Temperature profile at the wall (a) and thermal boundary layer (b)

The variation of the heat transfer coefficient along the length of the plate can be observed in Figure 7.4.

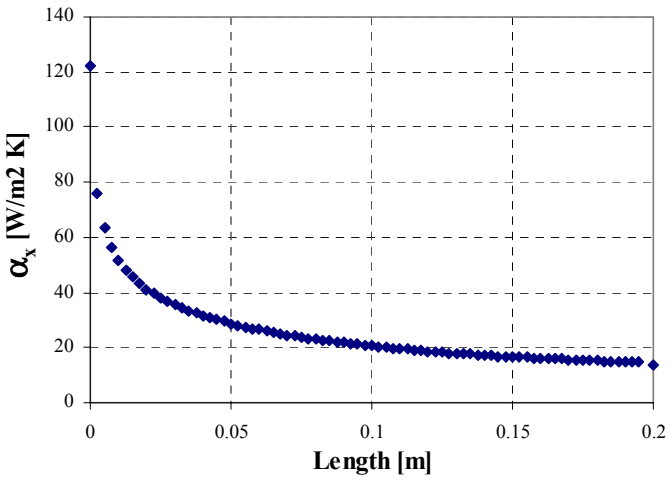

Figure 7.4 Local heat transfer coefficient along the plate for 8 kW and $T_{avg,w}$=20 °C from Fluent Simulation

The local heat transfer coefficient $\alpha_{g,x}$ is the quotient of the heat flux q and the temperature difference ΔT between the gas fluid T_g in the bulk and the local wall temperature on the plate $T_w(x)$:

$$\alpha_{g,x} = \frac{\dot{q}}{T_g - T_w(x)} . \qquad [7.4]$$

In Figure 7.4, it can be observed that at the top of the plate (y=0) a higher value for the heat transfer coefficient is reached due to the thin boundary layer at this point, but as the boundary layer grows in y-direction the heat transfer coefficient decreases as the temperature gradient, which is the driving force for heat transfer, will be reduced.

When condensation occurs, the latent heat and sensible heat transfer has to be considered simultaneously based on a heat and mass transfer analogy as described in chapter 4. Consequently, as the local convective heat transfer coefficient, the local mass transfer coefficient β_x varies along the length of the plate due to the growing of the boundary layer thickness as represented in Figure 7.5:

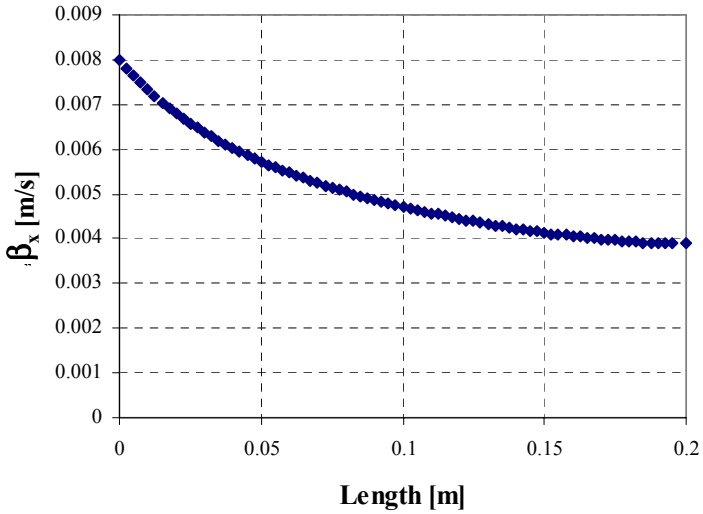

Figure 7.5 Mass transfer coefficient along the plate length for 8 kW and $T_{avg,w}$=20 °C

From the above figures, it can be observed that convection heat and mass transfer can be regarded as analogous. As for the heat transfer coefficient was explained, at the top of the plate (y=0) a higher value for the mass transfer coefficient can be observed, and as the boundary layer grows the mass transfer coefficient decreases. An explanation for this is that there is a bulk velocity of the gas mixture towards the wall, and non-condensable gases accumulate next to the wall building a boundary layer through which the vapor must diffuse. Therefore, the thinner the boundary layer, the better the transport of the species towards the wall resulting in an increase in the condensing rate.

7.1.3 Heat Transfer Resistances

The presence of non-condensable gas in a vapor which is condensing on a cold surface presents a diffusional resistance to condensation. As a result of the mass flow of the gas over the surface, non-condensable gases accumulates next to the liquid/vapor interface. A balance occurs between the bulk convection of non-condensable gas towards the surface of the plate and the diffusion of non-condensable gas from the interface. The balance between convection and diffusion results in a logarithmic gas concentration distribution near the interface as described in chapter 4.

To take into account the diffusional resistance, a model based on the diffusion layer theory [10] has been used. The mass transfer coefficient β is expressed in terms of an equivalent condensation heat transfer coefficient $\alpha_{g,cond}$ (eq.4.29-4.31). The heat flux is then controlled by the condensation heat transfer coefficient combined in parallel with the sensible heat transfer coefficient $\alpha_{g,conv}$ in the gas phase and in serie with the film, wall and coolant resistances as presented in Figure 4.2.

The total heat flux can be expressed as:

$$\dot{q} = \frac{T_g - T_c}{\sum_i R_i} \qquad [7.5]$$

where T_g is the temperature in the bulk mixture, T_c is the temperature of the coolant and R_i the thermal resistances.

In order to know if the condensation is controlled either by diffusion (condensation heat transfer coefficient) or by convection (sensible heat transfer coefficient), it is necessary to calculate the thermal resistances R_i encountered from the bulk mixture to the coolant.

By using the software EES, some calculations were carried out for different combustion powers in a range of 8 kW-24 kW and different surface temperatures. In Figure 7.6, the results corresponding to a combustion power of 8 kW and an average surface of 20 °C are plotted. It can be observed that the thermal resistance based on the condensation heat transfer coefficient $R_{g,cond}$, as a function of the mass transfer coefficient β, is smaller than the thermal resistance based on the convection heat transfer coefficient $R_{g,conv}$. Therefore, the condensation is controlled by diffusion across the gas boundary layer.

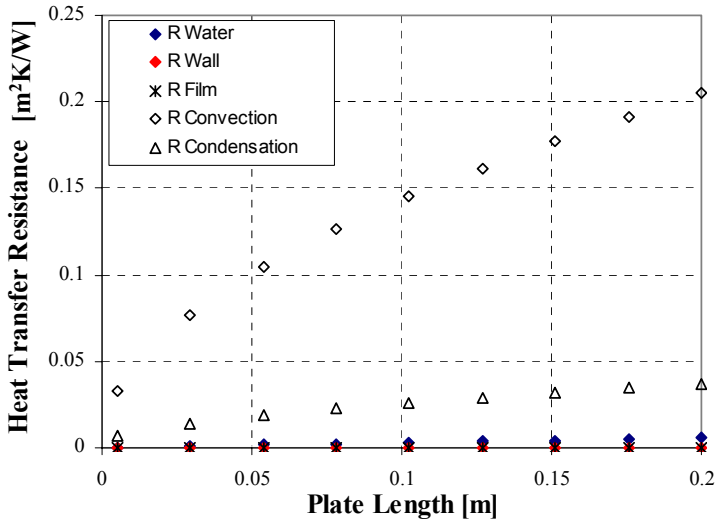

Figure 7.6 Thermal resistances for a combustion power of 8 kW and $T_{avg,w}$=20 °C by eq. 4.26,4.27,4.28,4.32,4.33,4.34

The film, wall and coolant resistances are negligible in comparison to the gas thermal resistance.

From the figure, it can be also interpreted the influence of the non-condensable boundary layer on the mass and heat transfer depending on the length of the plate. At the top of the plate,y = 0, the inertgas boundary layer is thinner. The convection and condensation thermal resistances are smaller and consequently a better heat and mass transfer towards the wall exists. As the inertgas boundary layer increases with the length of the plate, the thermal resistances increases as well.

Since at the top of the plate, the inertgas boundary layer is thin and it is important to check out if the condensation process is also controlled by diffusion at this location. In Figure 7.6, it can be observed that the diffusion also dominates at the inlet of the plate, as the condensation thermal resistance is smaller than the convection thermal resistance. But the best way to check this is by calculating the ratio of the overall heat transfer coefficient k´ from film to coolant and the heat transfer coefficient in the gas phase α_g [6]. For the case

$$\frac{k'}{\alpha_g} > 2 \qquad [7.6]$$

the diffusion controls the condensation process at the inlet of the plate. Otherwise, the condensation would be controlled by convection. Some calculations have been carried out and the ratio is higher than 2 for the entire plate. At the inlet this ratio has a value of 10, and it decreases with the length of plate until a value of 2.9. These two parameters k´and α_g are obtained from the energy balance:

$$\dot{q} = k'(T_w - T_{water}) = \alpha_g (T_g - T_w) . \qquad [7.7]$$

7.1.4 Gas Diffusion Coefficient

A careful treatment of chemical species diffusion in the species transport and energy equations is important when details of the molecular transport processes are significant, e.g., in diffusion-dominated laminar flows.

Diffusion coefficients in ideal-gas binary systems have been shown to be properties of the gas pair. The effective diffusion coefficient $D_{i,m}$ of species i in a multicomponent mixture also depends on the fluxes of the other species present. It is related to the mass fraction of the other components and the binary coefficients for each gas pair. The Maxwell-Stefan equations are used to obtain the corresponding diffusive mass fluxes (see Appendix E).

For an ideal gas mixture the activity and fugacity coefficients are unity In this case, the Maxwell diffusion coefficients would be equal to the ideal binary diffusion coefficients D_{ij} presented in Appendix A. In this thesis, the mixture exhibits deviations from ideal behavior as described in chapter 2. These deviations are taken into consideration in the Maxwell-Stefan equation [44] by a thermodynamic factor calculated from activity coefficient models as Margules, Van Laar, Wilson, NRTL and UNIQUAC. As described in chapter 4, the binary diffusion coefficients D_{ij} have to be replaced by $D_{ij,Maxwell}$ in eq 4.19.

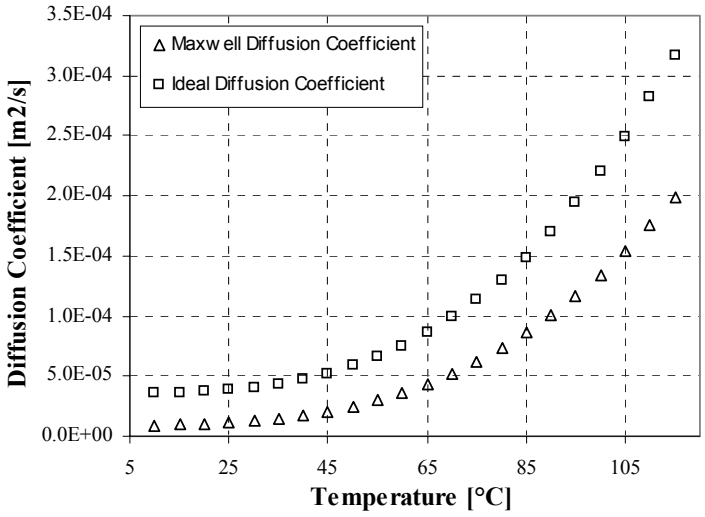

Figure 7.7 Diffusion coefficient Air-Water vs Temperature

In Figure 7.7, the ideal binary diffusion coefficient and the Maxwell diffusion coefficient of Air-Water depending on the temperature are plotted.

It can be observed that the Maxwell Diffusion coefficient for the gas pair Air-Water is smaller than the corresponding to the ideal mixture. This is due to the consideration of the diffusive flux of the other components present. Although the nitric and sulfuric acid are present in a small amount, their effect in the rate of diffusion must be taken into consideration as the molecular transport processes are significant especially in laminar flows.

There is also a Fick´s law correlation for multicomponent mixture [44], but it does not consider directly the non-ideality of the mixture as the Maxwell-Stefan equation. They are defined in the same way but related by the thermodynamic factor. Consequently, the physical interpretation of the Fick diffusion coefficient D is less transparent than for the Maxwell-Stefan diffusivity.

The software Fluent has the ability to model full multicomponent species transport by using the Maxwell-Stefan equation. In Figure 7.8, the rate of condensation when the Maxwell-Stefan equation is plotted in comparison with the results when an ideal binary diffusion coefficient is applied by using the software Fluent. It is known that the rate of condensation is proportional to the diffusion coefficient (see chapter 4).

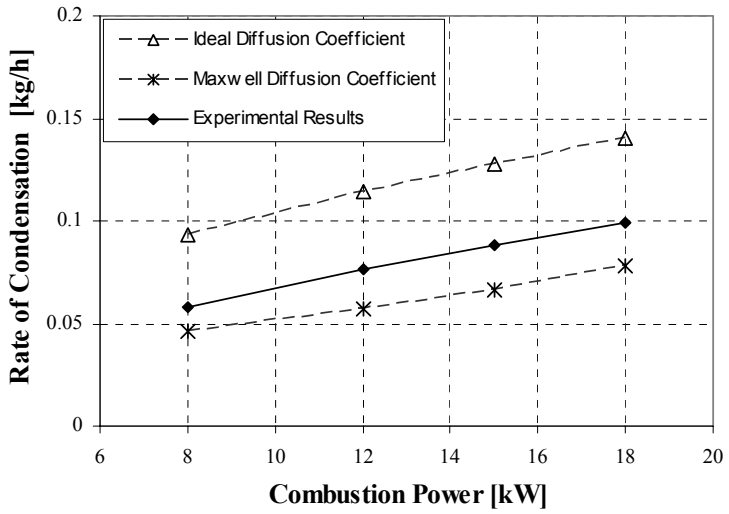

Figure 7.8 Rate of condensation for an average surface temperature 20 °C

From Figure 7.8, it can be seen that by using the ideal diffusion coefficient the discrepancies obtained in comparison with the experimental data are higher than by using the Maxwell diffusion coefficient. By the ideal diffusion coefficient, the deviations are in a range of 30-37 % uncertainty, whereas by the Maxwell-Stefan method the deviations are in a range of 17-21 %. In section 7.4, some plots of the rate of condensation corresponding to different average surface temperatures can be seen.

7.2 Convection Boundary Layer

Three boundary layers are developed over the surface of the plate: A velocity boundary layer referring to the manner in which the velocity varies with y (c.f. Figure 7.3) through the boundary layer. A thermal boundary layer due to the temperature gradient between the fluid free stream and surface, and a concentration boundary layer that determines convection mass transfer. The simulation results are described in the following sections in more detail.

7.2.1 Velocity

In Figure 7.9 , two velocity profiles are presented. On the left, the gas velocity profile is shown for a combustion power of 8 kW, and on the right the profile corresponding to a combustion power of 18 kW. The higher the combustion power, the higher the volumetric flow of the exhaust gases, therefore higher velocities are reached. In this way, the boundary layer for higher power input are thinner.

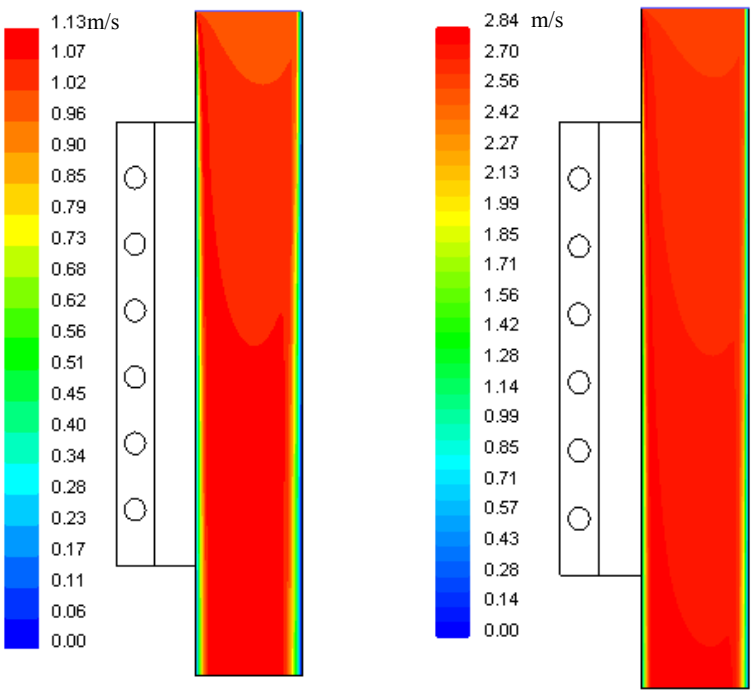

Figure 7.9 Velocity profile for a power of 8 kW (left) and 18 kW (right)

It can be observed that the consideration of the glass window has no much influence in the velocity profile (see right hand side of the contour plot in Figure 7.9).

Another point to be addressed is the slow velocity profile developed at the inlet due to entrance effects.

As described in chapter 5 (c.f. Figure 5.4), a 5 cm inlet section named “Adiabatic wall in” before the condensing plate is considered. In order to be able to analyse the influence of this inlet section in the velocity profile is shown in Figure 7.10 in a vectorial form. On the left it is shown the vectorial velocity profile for a combustion power of 8 kW, and on the right for a combustion power of 18 kW.

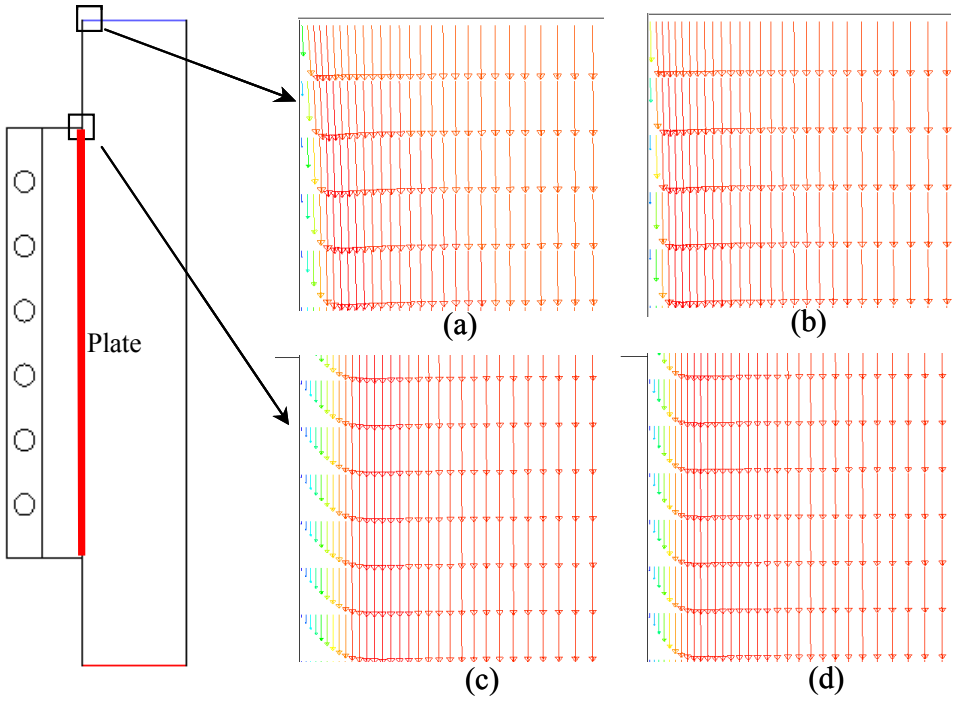

Figure 7.10 Velocity vector in the gas phase, on the left hand side above and below for 8 kW at the inlet (a) and at the top of the condensing plate (c), on the right hand above and below for 18 kW at the inlet (b) and at the top of the plate (d)

In figures a and b, the velocity vectors at the inlet section before the condensing plate (adiabatic walls, c.f. Figure 5.3) are plotted. In figures c and d, the velocity vectors profiles from the top of the condensing plate are shown. For higher combustion power a steeper parabolic velocity profile at the surface of the plate is observed (d). Consequently, a thinner inertgas boundary layer is developed.

The velocity profile changes from the top of the inlet section (a,b) until the top of the plate (c,d), where a laminar profile is developed. But due to the quasi linear temperature profile at the surface of the plate (c.f. Figure 7.3), the velocity profile is not whole constant over the plate length. In addition to this, a laminar fully developed velocity profile is not reached. An explanation for this is found by the calculation of the hydrodynamic entry length, as the length of the plate plays an important role to get fully developed flow.

The hydrodynamic entry length depends whether the flow is laminar or turbulent in the form [5]:

$$L_{fd,h} = 0.056\,Re_{dh}\,d_h \qquad \text{For Laminar Flow, } Re_{dh} < 2300 \qquad [7.8]$$

$$L_{fd,h} = 1.5\,Re_{dh}^{0,25}\,d_h \qquad \text{For Turbulent Flow, } 2300 < Re_{dh} < 10^4 . \qquad [7.9]$$

The hydrodynamic entry length $L_{fd,h}$ for a combustion power of 8 kW is 7.68 m (eq. 7.8), and for a combustion power of 18 kW is 0.78 m (eq. 7.9). It means that beyond these lengths laminar fully developed velocity profile is reached. The length of the plate is 0.2 m. It is short enough that fully developed velocity profile will never take place, and turbulent flow will never be triggered.

Experimentally, dropwise condensation takes place instead of filmwise condensation. Therefore, the effect of the drops in the gas flow and in the rate of condensation is studied.

Some arbitrary drops were assumed to exist on the surface of the plate. Drops with a sphere or elliptic shape were taken into consideration. The diameter of the drops was about ca. 1 mm, and hence smaller than the thickness of the boundary layer of 1-2.5 mm corresponding to 8 kW. Also drops with different diameters in a range 1-4 mm in order to have bigger ones than the boundary layer of 1-2.5 mm were assumed. The results are presented in section 7.4.2.

A 3D simulation for the vertical cooled plate was carried out in order to know whether it had an influence in the results, but it was found out that the results did not differ more than 2 % in comparison with the results from the 2D simulation.

7.2.2 Temperature

Just as the velocity boundary layer develops when there is fluid flow over a surface, a thermal boundary layer must develop if the fluid free stream and surface temperatures differ.

In Figure 7.11 on the left hand side, the temperature profile for 8 kW is plotted and on the right hand side the temperature profile for a combustion power of 18 kW. The average surface temperature corresponds to 20 °C. It is important to note that the adiabatic walls have no influence on the temperature profile, as they had in the velocity profile.

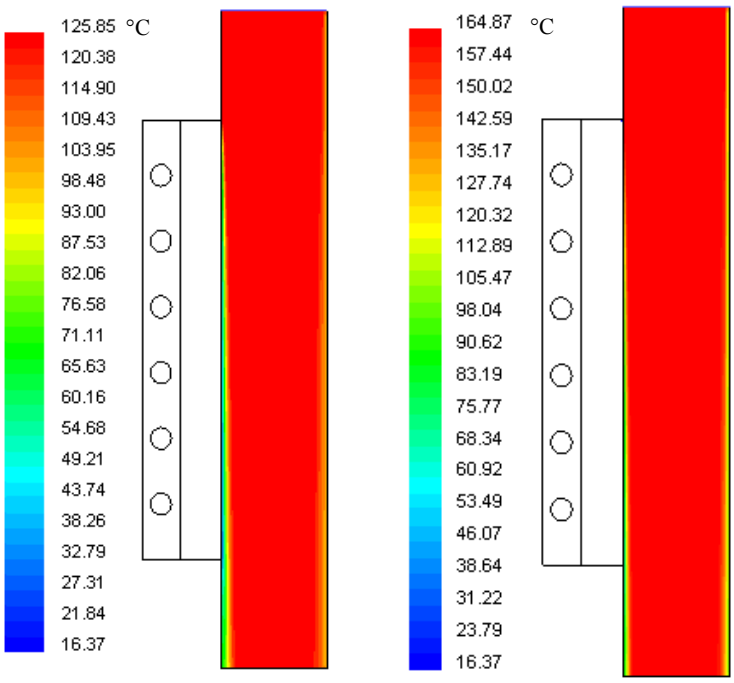

Figure 7.11 Temperature profile for a power of 8 kW (left) and 18 kW (right)

The temperature profile at the surface has the same tendency as the velocity profile. For 18 kW combustion power, the gas velocity is higher and consequently the thermal boundary layer is thinner. On the opposite, for a combustion power of 8 kW, the gas velocity is smaller, so a thicker thermal boundary layer is formed.

The effect of the glass window (c.f. Figure 5.3) depending on the power input can be well observed in these figures. For 8 kW, a temperature profile on the side of the glass window it can be hardly seen in comparison to the temperature profile for 18 kW where it is visible. The reason is because the temperature at this surface is 120 °C, being almost the same as the gas inlet temperature of 125 °C for 8 kW. A negligible temperature gradient is then existing. In case of 18 kW, the gas inlet temperature is 165 °C and this considerable temperature difference of 45 °C is reflected in the results.

As condensation is only desired at the surface of the plate, the temperature of the glass window was set to 120 °C above the dew point of the mixture namely 115 °C when sulfuric acid is present. In case for a mixture of nitric acid, water and air, the dew point is 56 °C. So that, this temperature of 120 °C in the glass window is also high enough.

7.2.3 Concentration

For multicomponent mixture condensation the distinctive feature is the significant change of components concentration during the condensation process. The profile of the mole fraction of the sulfuric acid, nitric acid and water in the gas phase is plotted in Figure 7.12 .

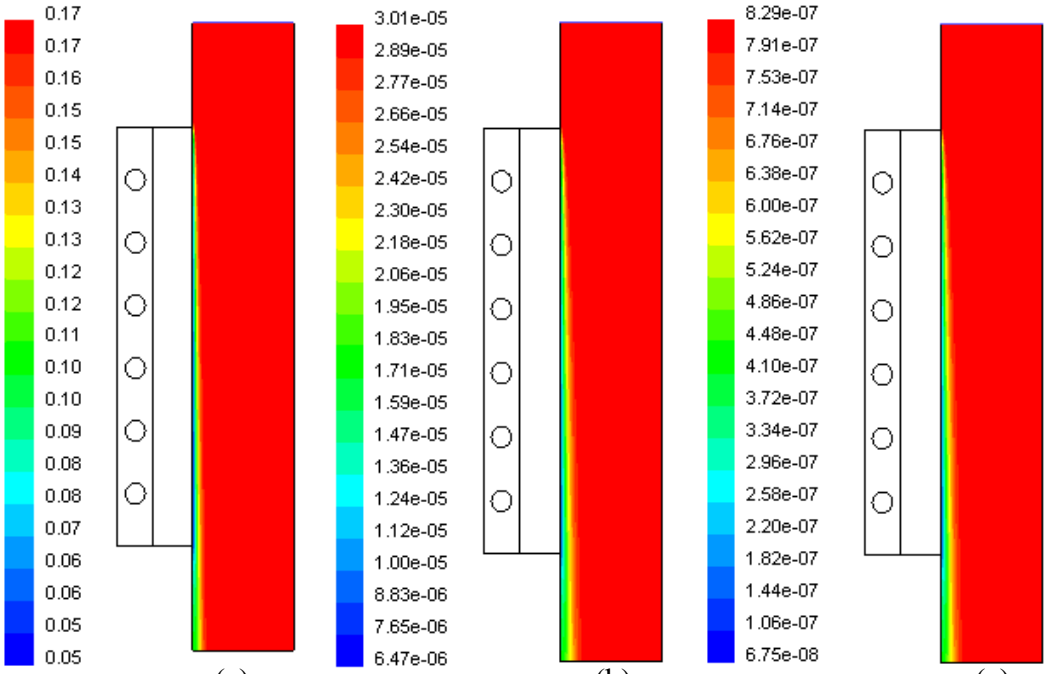

Figure 7.12 Mole fraction profile of H_2O (a), HNO_3 (b), H_2SO_4 (c) for a combustion power of 8 kW

The concentration boundary layer has the same tendency as the thermal and velocity boundary layer. Due to the condensation process at the interface, there is a bulk velocity of the gas toward the wall. Nitric acid, sulfuric acid and water vapor condense at the plate and air accumulates next to the wall. A noncondensable gas boundary layer is formed through which the components have to diffuse to condense at the plate.

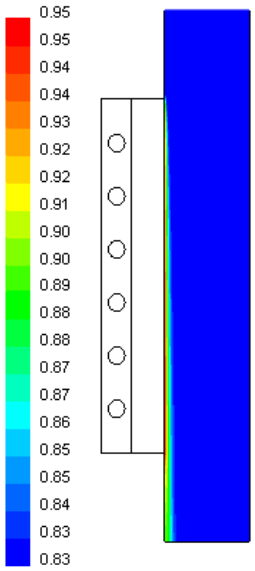

Figure 7.13 Mole fraction profile of Air for a combustion power of 8kW

The concentration of the air (c.f.Figure 7.14) at the interface is higher than its value in the bulk. This, in turn, decreases the partial pressure of the vapor at the interface below its bulk value. The saturation temperature at which the condensation takes place is also reduced (c.f. Figure 7.15-7.16) and the thermal driving force is higher, thereby reducing heat transfer.

The rate of heat transfer significantly depends on diffusion interactions which define the complicated concentrations profiles in normal direction to flow of mixture. In Figure 7.14, the concentration profiles of all components present in the mixture in normal direction to the flow (direction x) are plotted. A typical profile in the presence of noncondensable gases is observed.

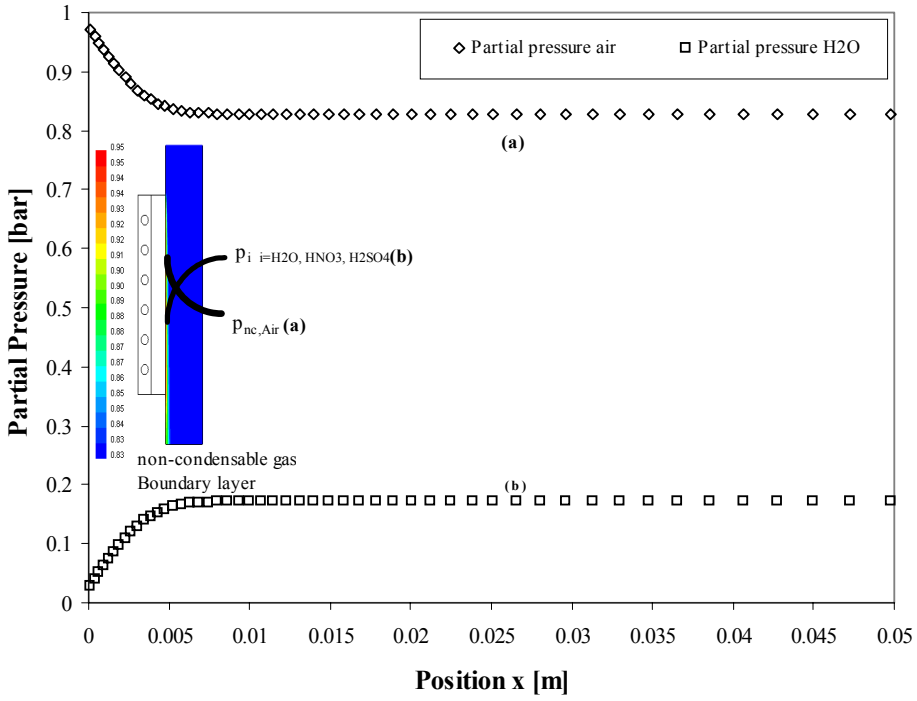

Figure 7.14 Partial pressure of air-water present in the mixture for a combustion power of 8 kW

The partial pressure of nitric and sulfuric acid in the bulk, 3 10^{-5} and 8 10^{-7} bar, respectively, are negligible in comparison with the partial pressure of water vapor 0.17 bar and air 0.88 bar. But the tendency is the same as for the partial pressure of water vapor (b).

For a combustion power of 18 kW, higher gas velocity are reached, so a thinner concentration boundary layer is formed. The concentration boundary profile has the same tendency as in Figure 7.12.

7.3 Dew Point Temperature

During condensation, the dew point temperature will decrease due to a composition shift. The preferential condensation of the heavier component in a mixture leaves the remaining vapor phase enriched with the lighter component, thus causing the dew point temperature to drop. This leads to a decrease in temperature difference between the condensate and coolant, leading to a reduction in local heat transfer.

In figures below, the dew point corresponding to the binary systems nitric acid-water and sulfuric acid-water are shown.

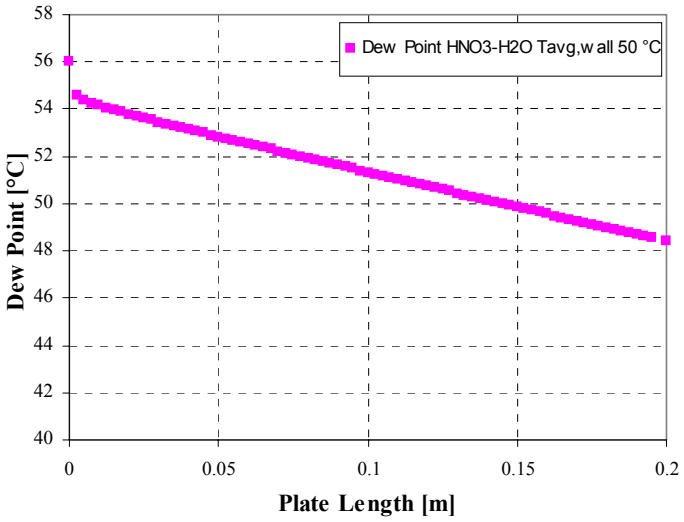

Figure 7.15 Dew point vs length of the plate for the binary system HNO_3-H_2O

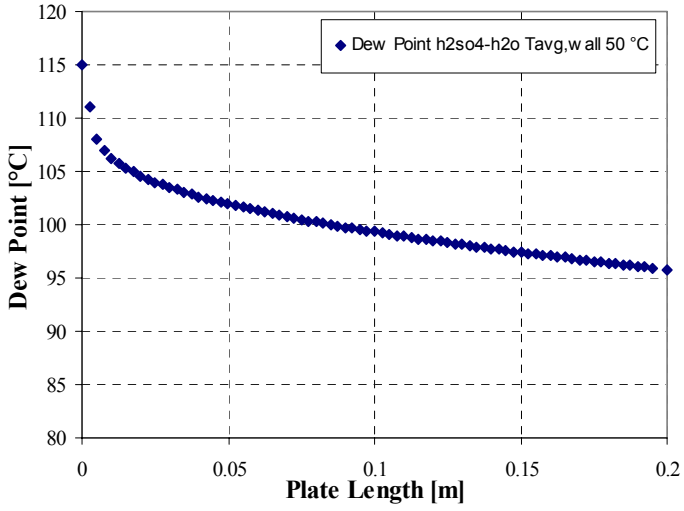

Figure 7.16 Dew point vs length of the plate for the binary system H_2SO_4-H_2O

A variation in the dew point between 15-20 °C along the length of the plate is observed in the above figures.

7.4 Condensation Rate

In the following sections, the condensation of nitric acid, sulfuric acid as well as the total condensation rate are presented.

7.4.1 Condensation Rate of Nitric and Sulfuric Acid

As explained in section 7.2.3, a concentration boundary layer is formed due to the presence of non-condensable gases in the gas mixture. This concentration gradient as well as the velocity and thermal gradients have an influence in the rate of condensation. At the top of the plate, the rate of condensation is the highest as the boundary layer is thinner in this location. The condensation rate decreases with the length of the plate as the boundary layer grows.

In Figures 7.17 and 7.18 the simulated profile of the condensation rate of nitric and sulfuric acid over the length plate is shown. Indeed, the highest rate of condensation can be observed at the top of the plate, as the molecules can diffuse more quickly through the thin boundary layer. In case of condensation of water, the tendency is the same as for nitric and sulfuric acid.

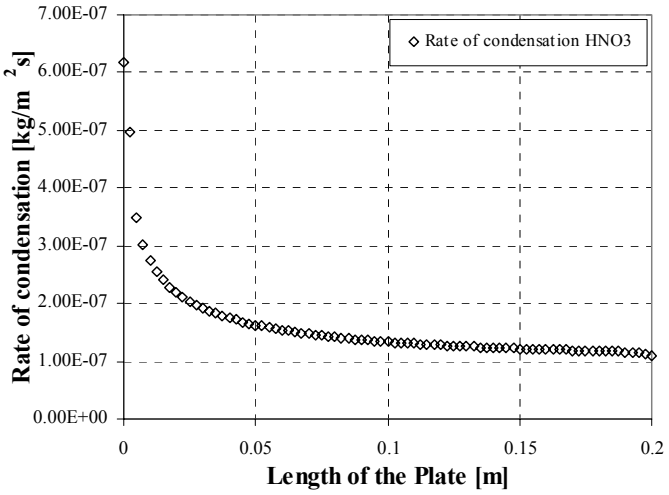

Figure 7.17 Rate of condensation of nitric acid for 8 kW, $T_{avg,w}$ 20 °C

Depending on the combustion power, more or less nitric acid condenses but the amount of water present in the condensate increases or decreases at the same time too. It means that the concentration of nitric and sulfuric acid in ppm remains constant in all combustion power range due to the constant value of 1.2 for the excess of oxygen set

for all experiments. A comparison between the results obtained by the simulation in Fluent and the experimental data is can be found in the following section 7.4.1.1.

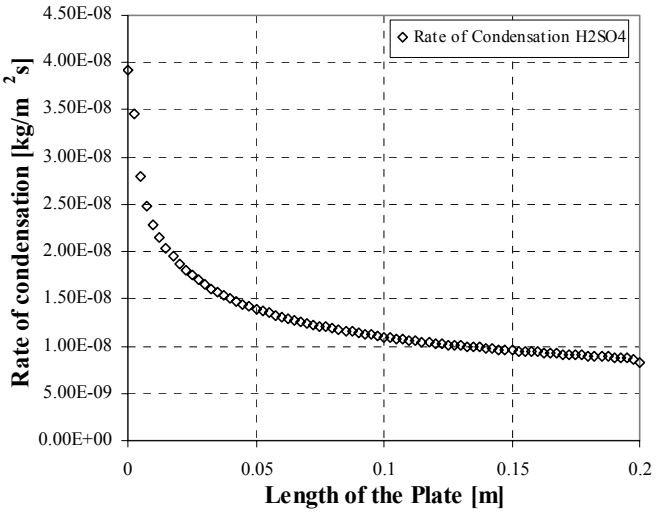

Figure 7.18 Rate of condensation of sulfuric acid for 8 kW, $T_{avg,w}$ 20 °C

7.4.1.1 Composition Balance of NO_x and SO_x

The measurement of the compositions of NO_x and SO_x was carried out in the test section in order to know the amount of nitric acid and sulfuric acid present in the exhaust gases. This value is assumed as inlet boundary condition for the simulation to validate the model. The way of procedure is explained in detail in chapter 6. But it may briefly be mentioned that a gas sample was taken at the inlet and outlet of the test section, and in order to fulfil the balance the mass at the inlet should be equal to the mass at the outlet by taking into account the condensate on the plate too.

The concentration of NO_x and SO_x experimentally obtained is shown in Figure 7.19 and 7.20. As mentioned in the former section, it can be observed that the concentration remains almost constant for all combustion power, and the reason is because a constant value of approximately of 1.2 for the excess of oxygen was taken for all experiments.

A comparison between the amount of NO_x and SO_x measured at the inlet and outlet, by taking into account the amount of condensate, of the test section is done. From Figure 7.19, it can be noted that there is a difference of 6 ppm in the NO_x amount whereas a difference of 0.2 ppm is obtained for the SO_x amount as shown in Figure 7.20. These discrepancies between inlet and outlet exist as the mass composition balance have to be applied for all components present in the mixture including water vapor. It means that at the inlet there is more water vapor than at the outlet as it condenses at the surface of the plate. By carrying out the corresponding calculations, it was found out that the mass balance was fullfilled.

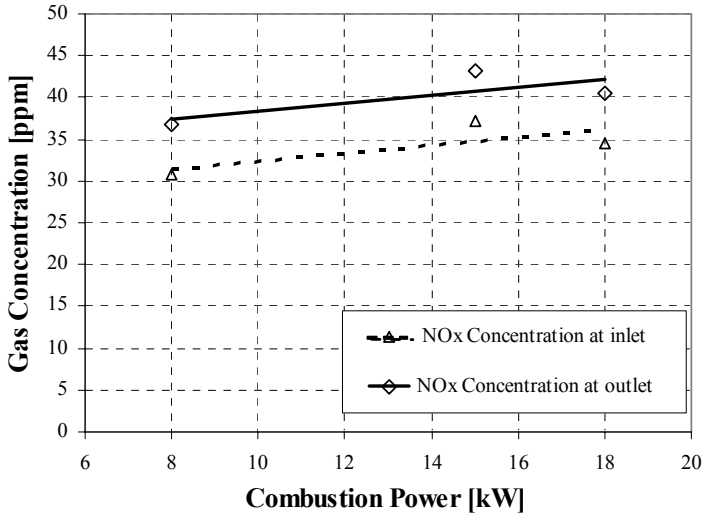

Figure 7.19 NO_x concentration in the exhaust gases

As it was mentioned, the amount of NO_x and SO_x measured is a boundary condition in the numerical simulation. Therefore, it is not only aim of validating the simulation by a comparison of the experimental and simulation results of the total condensation rate, but also the rate of condensation of nitric and sulfuric acid has to be taken into account and be compared. This is also done in order to know if the prevention of possible corrosion problems can be interpreted from the simulation results with good accuracy, being able then to optimize the geometry if it is required.

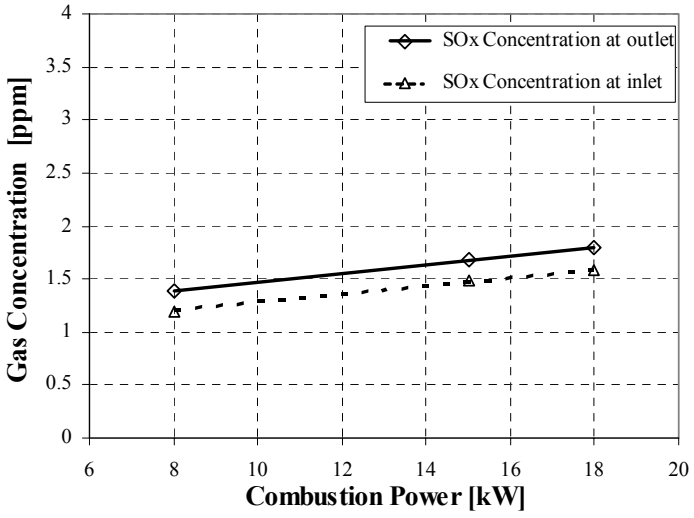

Figure 7.20 SO_x concentration in the exhaust gases

From the analyses of the gas samples, the amount of NO_x and SO_x in the condensate is known. It results in a concentration of 14.34 ppm and 1.06 ppm respectively. In the simulation, a value of 13.78 ppm NO_x and 1.08 ppm SO_x is obtained. It means that there

is only a deviation of 3.8 % in the NO_x concentration and 2.8 % error in the SO_x concentration. The accuracy of the simulation is very good.

7.4.2 Total Condensation Rate

As described in chapter 6, on the base of the test section there is one condensate collector that catches condensate which falls from the condensing plate. The rate at which condensate is produced on the plate can be determined from measurements of the weight of the sump in an electrical scale. This amount is compared with the simulation results in order to validate the model.

The experimental results and the simulation results by the numerical and empirical solution are presented in the next figures 7.21 for different average surface temperature.

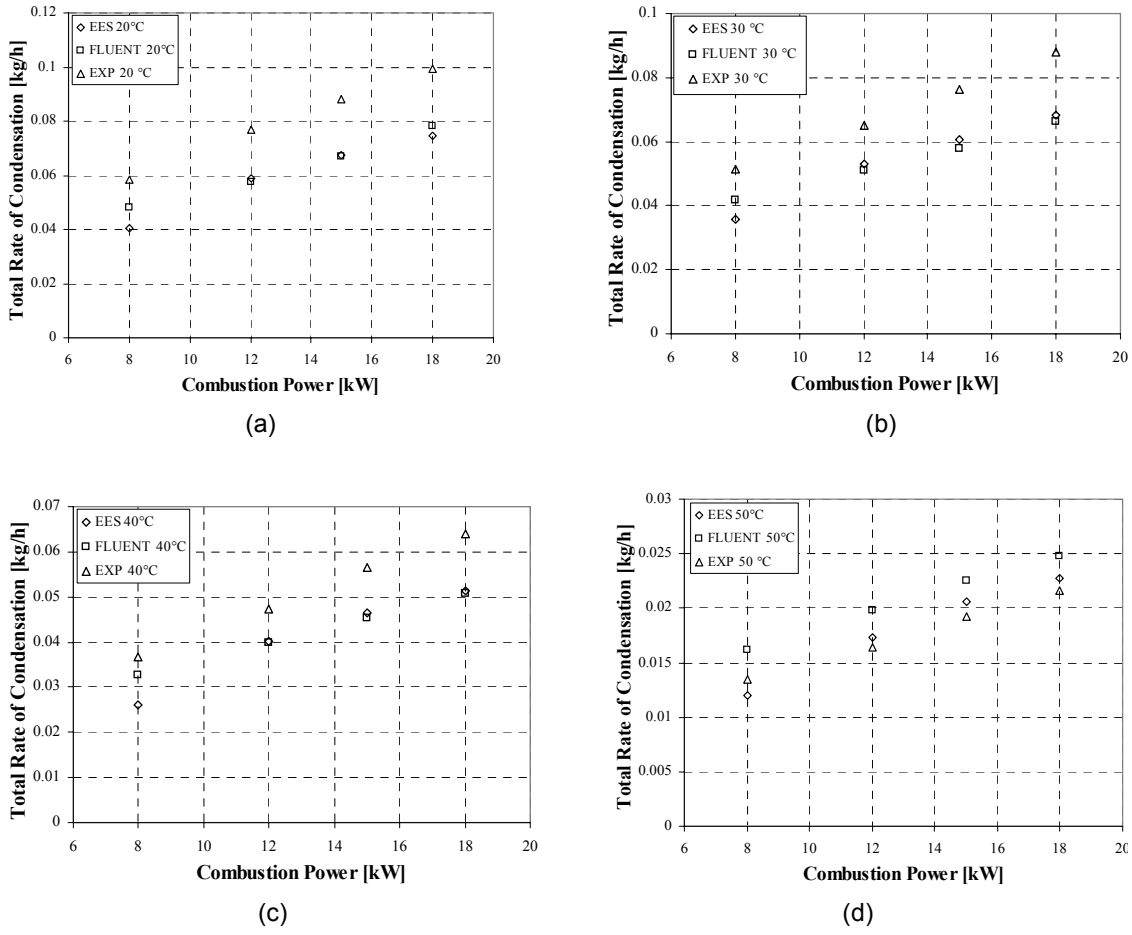

Figure 7.21 Total rate of condensation for an average surface temperature of 20 °C (a), 30 °C (b), 40 °C (c) and 50 °C (d)

From Figure 7.21, it can be observed that the rate of condensation increases as the combustion power increases. This is because for higher combustion powers a thinner boundary layer is formed. Consequently, a larger condensation rate is obtained.

The average surface temperature was varied in a range of 20 °C-50 °C. It means, below the dew point 56 °C for the binary system nitric acid/water, and of course below the dew point 115 °C for the binary system sulfuric acid/water. The condensation on the plate is ensured. Whether pure methane or methane with a certain amount of sulfur is applied does not have an influence in the total condensation rate as the amount of sulfur is very small in comparison with the mass fraction of water vapor present in the mixture. But of course, it has an influence on the corrosion process at the surface.

By comparing experiments and simulation, the deviations between the numerical simulation carried out with the software Fluent and experiments are in a range of ± 10-25 %, whereas the deviations by the simulation based on empirical correlations carried out with the software EES are in a range of ± 7-30 %. The simulation results differ to each other in maximal 8% for a combustion power of 8kW. Above 12 kW, the accuracy between both simulations is very good.

The explanation for this 8 % deviation for 8 kW combustion power is due to the small gas velocity, and therefore the thicker inertgas boundary layer built at the surface of the plate. As mentioned in former sections, the condensing components have to diffuse through the non-condensable gas under the influence of its partial pressure gradient. In turn, the noncondensable gas tries to diffuse away from the interface against the vapor flow. Due to this phenomena, the results obtained by Fluent are more accurate as by the empirical solution in comparison with the experiments. One reason could be that in the numerical simulation the diffusion coefficient is better considered as in the simulation bases on empirical correlations. For the latter, the diffusion coefficient is calculated by the Füller, Schettler, and Giddings equation presented in Appendix D corresponding to an ideal mixture. On the other hand, the diffusion coefficient in Fluent is calculated by the Maxwell-Stefan equation for multicomponent mixtures presented in Appendix E considering the non-idealities in the gas (see section 7.1.4).

Another point to be noted from the figures presented above is that the accuracy between simulation and experiments varies also depending on the surface temperature. The deviations are about 25 % for an average surface temperature of 20 °C whereas for an average surface temperature of 50 °C they decreases to 7-10 %.

An explanation for this is the formation of droplets on the plate depending on the surface temperature. With the exhaust gases flowing downwards over the condensing plate, droplets of condensate begin to form on the surface very rapidly at many points. Once the droplets form, they can begin to grow on the surface. These drain off the plate quickly, coalescing with smaller drops on the way down, leaving the surface. Further dropwise condensation could occur as bare areas of metal surface are exposed to the gas. The process is repeated all over the surface in a very dynamic manner.

In Figure 7.22, the droplets formed on the surface of the plate for an average temperature of 20 °C (right) and 50 °C (left) are observed.

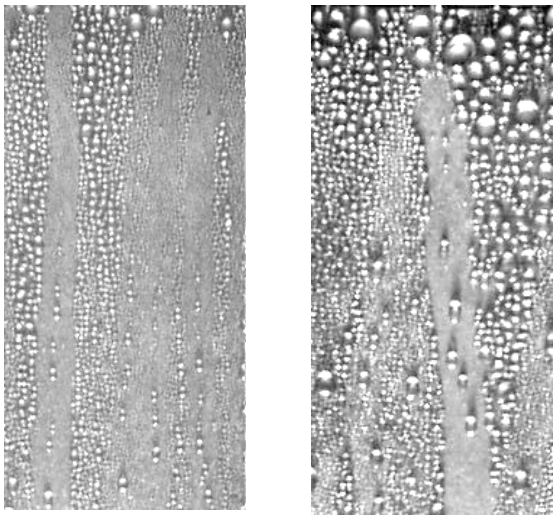

Figure 7.22 Droplets formed at the condensing plate for an average surface temperature of 50 °C (left) and 20 °C (right)

On the left figure, the droplets are much smaller than in the other case. This is because the surface temperature is higher and the droplets grow slowly. The residence time is much longer and therefore the surface is covered for a longer time with condensate.

On the other hand, when the surface temperature is 20 °C, the droplets grow more quickly and they run off the surface leaving the surface clear so that further condensation could occur. The dropwise condensation effect is much stronger in this case than for higher average surface temperature.

As the droplets are growing, vortices take place between them making the gas stream more complex as it is in the theoritical case. The physic is very complicated then and there is no governing equations to take into consideration this behavior. The smaller the droplets, the smaller the vortices. Therefore, there is not too much influence on the main gas stream and a better accuracy between experiments and simulation is observed (c.f. Figure 7.21 d). On the opposite, as the droplets are larger, the vortices are more accentuated having an influence on the main gas stream and a worse accuracy between experiments and simulation is obtained (c.f. Figure 7.21 a).

In order to check this effect of turbulences between the drops in the gas flow and so that in the rate of condensation, a numerical simulation was carried out for 8 kW. Some arbitrary drops were assumed to exist on the surface of the plate as shown in Figure 7.23. Drops with a diameter of 1mm smaller than the thickness of the boundary layer of

1-2.5 mm were considered, as well as, drops with different diameters in a range of 1-3 mm in order to have bigger ones than the boundary layer.

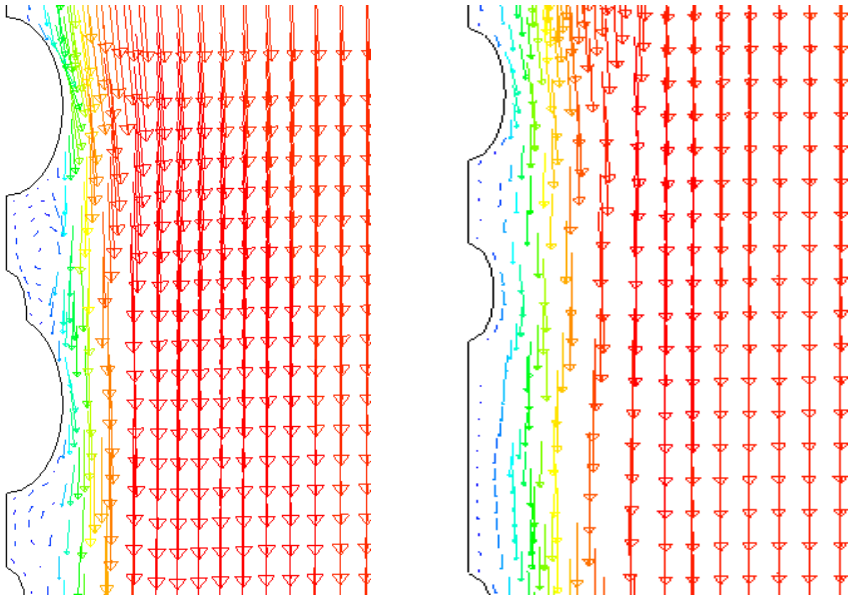

Figure 7.23 Velocity vectors for droplets of 3 mm diameter (a) and 1 mm diameter (b) for a combustion power of 8 kW

From the Figure 7.23, it can be clearly observed what it was mentioned in the paragraph above. For bigger droplets corresponding to an average surface temperature of 20 °C, vortices can be seen (a). For smaller droplets corresponding to an average surface temperature of 50 °C, vortices do not exist (b) although a disturbance exists.

A 3D Simulation for the cooled vertical plate was carried out in order to know whether the gas boundary layer at the aluminium lids had an effect, and it was found out that the results were the same as for the 2D simulation.

7.5 3D-Simulation

7.5.1 Annular Fin Heat Exchanger

It is objective of this work to apply the condensation model, programmed in the UDFs in Fluent, in real geometries to optimize them. The first simulation in a real geometry is based on a fin heat exchanger as shown in Figure 7.24.

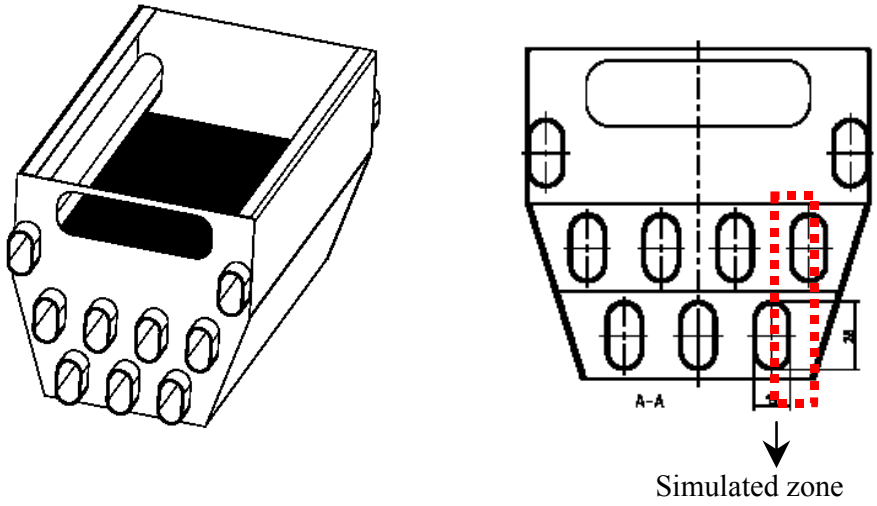

Figure 7.24 Fin heat exchanger

The tubes and fins are arranged in a staggered geometry as the path of the main flow is more tortuous and a greater portion of the surface area of downstream tubes remains in this path. Consequently, a better heat transfer takes place.

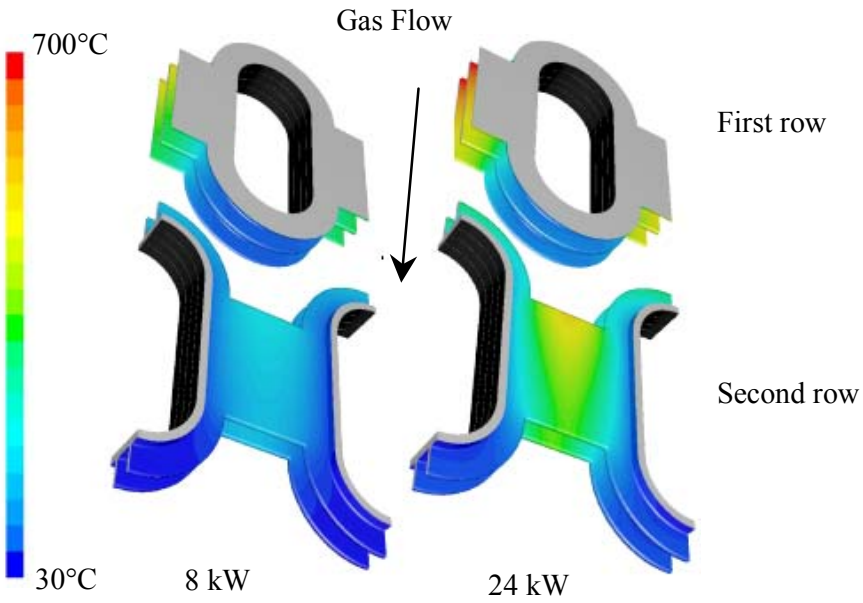

Figure 7.25 Surface temperature profile in a fin heat exchanger for 8 kW and 24 kW

In Figure 7.25, the temperature profile for the cut-out section with the symmetric part marked in Figure 7.24 is shown for a combustion power of 8 kW and 24 kW. The surface in a gray color represents a cut-off of the fin and tube surface. The gas flows downwards, and the first row of fins tubes is warmer than the second. In the zone

between two tubes, the surface temperatures are the highest. Thus, the temperatures are much higher for 24 kW as for 8 kW.

As explained in detail in chapter 2, the exhaust gases mixture is composed of sulfuric acid, nitric acid, water vapor and air. The first components that condense on the surface are sulfuric acid and water when the surface temperature is below the dew point corresponding to this binary system. The dew point depends on the mass fraction of the components present in the mixture. For an amount of sulfur of 11 ppm in the gas and 17 vol. % water vapor the dew temperature is 115 °C. These both components condense first at the top of the tube in the second row (c.f. Figure 7.26). The condensation rate decreases along the tube in direction of the gas flow due to the formation of the noncondensable gas boundary layer. The effects are the same as the ones explained in the former section for the condensing plate. At the bottom of the second row, condensation of sulfuric acid and water in the fin is also observed. At this location in the fin, the surface temperature reaches for the first time a temperature below the dew point. The condensate will be more or less corrosive depending on the composition of the components in the condensate.

When the surface temperature is below 56 °C, the condensation of nitric acid together with water takes place. This dew temperature for this binary system corresponds to 30 ppm of nitric in the gas and 17 % water vapor in volume. As it is described in section 7.3, the dew point varies during the condensation due to the partial pressure gradient. All sulfuric acid present has almost condensed above 56 °C, and on the opposite a small amount of water has only condensed. The highest amount of water condenses then below 56 °C. But it does not mean that nitric acid is then less corrosive than sulfuric acid because it is more dilute in water. Depending on the material of the heat exchanger, there is a maximal point of corrosion for a certain composition of the acids and water in the condensate. And for this reason, it can happen that nitric acid is very corrosive under certain conditions. Another effect to be taken into consideration in the corrosion process is the temperture. The acid mixture corrodes the material more quickly in zones where the gas temperature is higher than in zones where the gas temperature is smaller due to the activation energy [56]. The activation energy increases with the temperature, and the higher the activation energy is, the higher is the reaction of corrosion described by the Arrhenius equation.

It can be clearly seen in Figure 7.26 that the condensation of nitric acid and water occurs at the bottom of the tube in the second row, whereas the condensation of sulfuric acid occurs before.

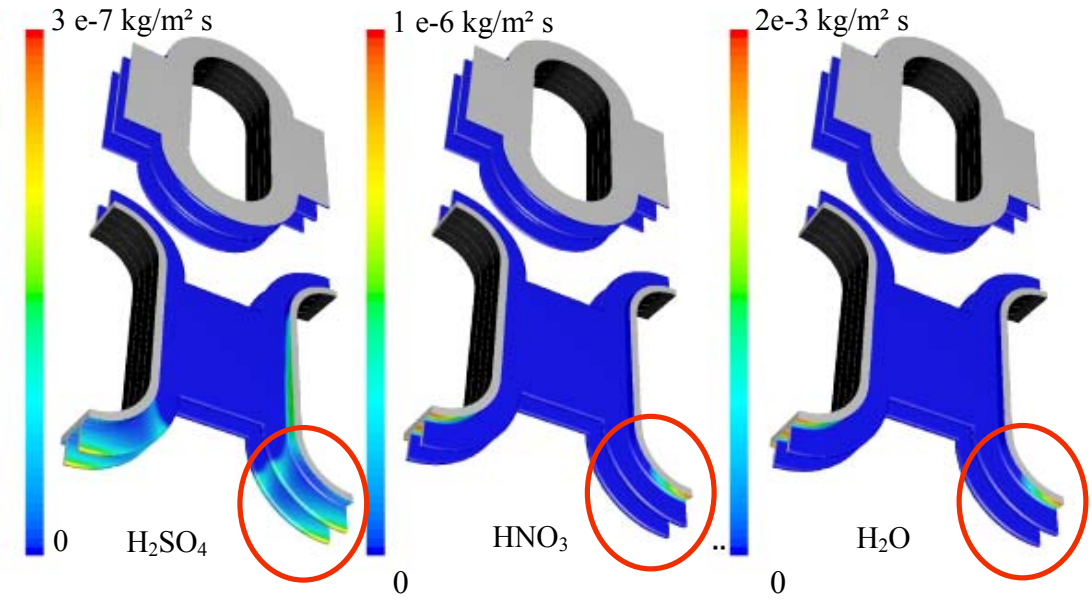

Figure 7.26 Rate of condensation of H_2SO_4, HNO_3 and H_2O

However, it is to be noted the maximal rate of condensation at the bottom of the fin in the second row for the case of condensation of sulfuric acid. The behavior should be analogous to the condensation rate along the tube decreasing as the boundary layer grows in the flow direction. But in this zone, there is back flow existing as shown in Figure 7.27.

This back flow has an influence in the rate of condensation, and the fin in this location is considered as if it would be a vertical plate. The gas flows upwards in this region producing some vortices and the maximal gas velocity is reached at the bottom of the fin. By means of this, the boundary layer is thinner in this location and the components can easier diffuse towards the wall, and hence the rate of condensation increases there.

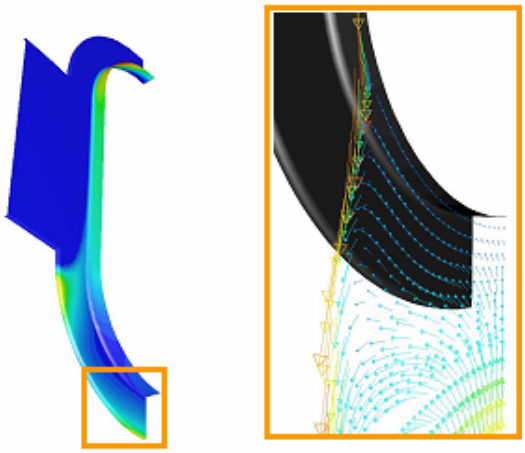

Figure 7.27 Flow vector at the bottom of the heat exchanger

As mentioned in one of the above paragraphs, the rate of corrosion of the material due to the condensation depends on the composition of the components present in the condensate. But it also depends on the material and surface temperature. This rate of corrosion as a function of the temperature and mass fraction of the acid is represented in the UDF in Fluent by polynomial functions based on the curves shown in Figure 7.28 [56].

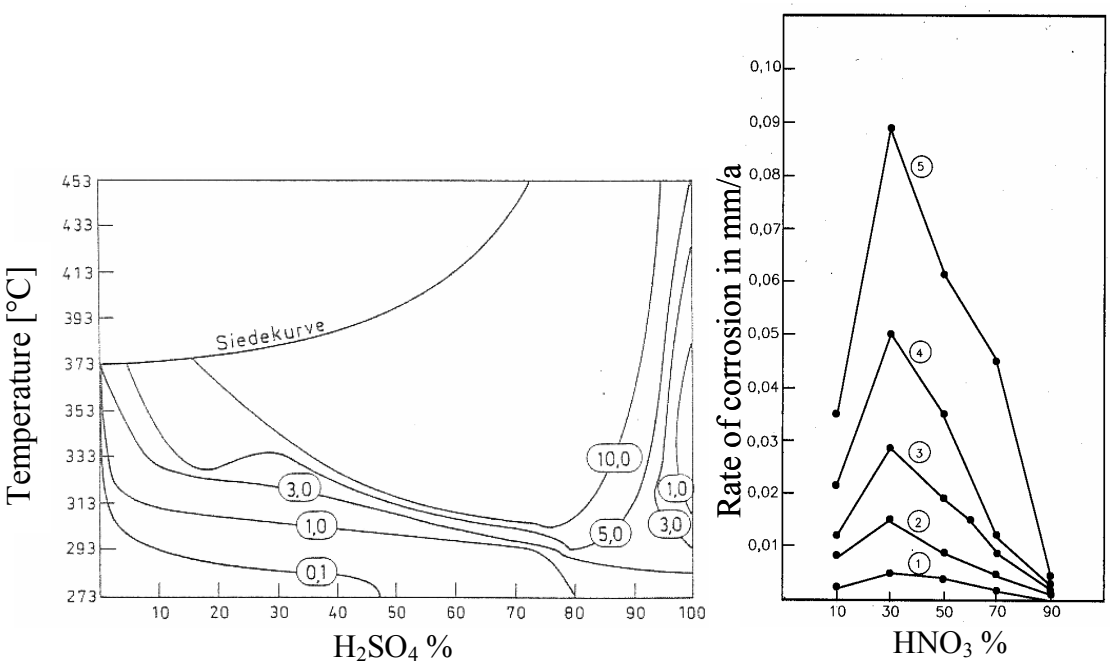

Figure 7.28 Rate of corrosion in mm/a in aluminium for different surface temperatures On the right figure, the numbers 1-5 refer to the surface temperature corresponding to 313, 323, 333, 343 and 353 K

A last point to take into consideration is the effect of the combustion power on the rate of condensation. In Figure 7.29, the condensation rate of sulfuric acid is presented for a combustion power of 8 and 24 kW. In spite of the high surface temperature reached, for a power of 24 kW in comparison to 8 kW, the rate of condensation of sulfuric acid in the zone 1 on the tube is higher. This is why for a power of 24 kW, the gas velocity is higher, the boundary layer is thinner and therefore the sulfuric acid diffuse easier towards the wall. But it should be noted that the condensation takes place earlier on the tube (zone 1) as well as on the fin (zone 2) for a smaller combustion power than for a higher combustion power. Concerning the condensation at the bottom of the fin, back flow exists as shown in Figure 7.27. And it can be observed that the higher the combustion power, the higher the rate of condensation due to the high gas velocities.

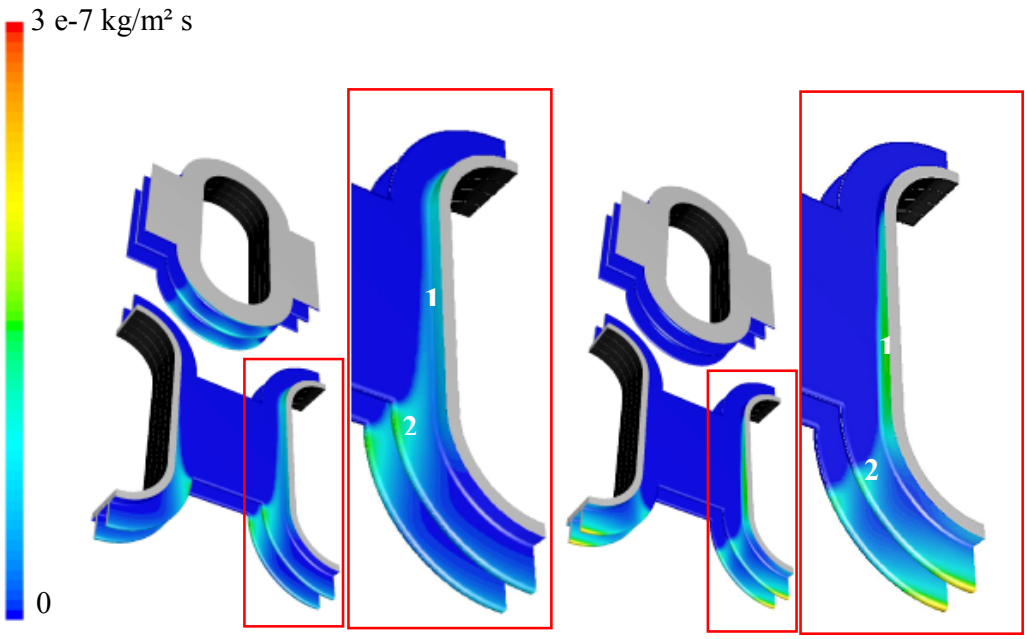

Figure 7.29 Rate of condensation of H_2SO_4 for a combustion power of 8 (left) and 24 kW (right)

7.5.2 Pin Fin Heat Exchanger

The simulation model developed in FLUENT was also applied on a pin fin heat exchanger. The results closely resemble experimental observations.

As it was mentioned, the condensation of acids leads to corrosion of the material, and objective in this work is to be able to know where condensation takes place in order to prevent this corrosion by performing parametric studies. Once it is known where condensation takes place as well as the mass composition of the components in the condensate, the rate of corrosion can be obtained by using the diagrams in Figure 7.28.

The rate of corrosion due to the nitric acid and sulfuric acid corresponding to a combustion power of 8 kW, when steady state was reached, has been obtained. The boundary conditions were then changed to the ones corresponding to a higher combustion power of 24 kW. In addition, a simulation for unsteady state was carried out.

As the combustion power is increased, the surface temperature also increases. This means that the rate of corrosion shifts along the surface of the heat exchanger after a certain time as some of the condensate is evaporated due to the increase of the surface temperature. Condensation takes place when the combustion power is decreased from 24 kW to 8 kW due to the cooling of the surface of the heat exchanger. Therefore, the

condensate becomes increasingly corrosive at surfaces of the heat exchanger after it is concentrate by repeated condensation and evaporation.

The deviation between the numerical simulation and experimental results is about 20 %. By means of this result, the simulation model in FLUENT can be applied to a given design in order to perform parametric studies and optimize the geometry with the aim of minimizing corrosion.

8 Conclusions and Outlook

A simulation model for the condensation of the exhaust gas mixture from the combustion of methane, was developed by using the commercial code FLUENT as well as by using an Engineering Equation Solver program where the calculation was based on empirical correlations. A vertical water-cooled plate was built in order to carry out experiments for the validation of the model.

The combustion of methane only was carried out as well as methane with a certain amount of an odourant compound, C_3H_8S. The products of combustion are typically nitrogen oxides and sulfur oxides as well as the expected water vapor and carbon dioxide. These oxides react with water vapor forming nitric acid, HNO_3, and sulfuric acid, H_2SO_4. Therefore, the understanding of the reaction mechanisms of these acid gases was required. These mechanisms depend on the gas temperature. In the simulation, the intermediate reactions are not taken into account because the inlet gas temperature is below the temperature at which the acids are already completely formed.

Condensation occurs when the surface temperature is below the dew point of the multicomponent mixture. Therefore, Vapor-Liquid Equilibrium (VLE) models were required in order to determine the dew point of the mixture. In this work, the condensation of sulfuric acid with water was considered to take place between the dew point temperature of the system HNO_3/H_2O of 56 °C and the dew point of the binary mixture H_2SO_4/H_2O of 115 °C. The condensation of nitric acid with water occurs below 56 °C. For a temperature near by 56 °C, all sulfuric acid has almost condensed.

Both binary systems exhibit azeotropy and therefore the activity coeffcients of the components present in the mixture have been calculated. The Van Laar model was applied to consider this deviation of the ideality. These activity coefficients were taken into consideration in the Raoult´s law providing a very good approximation. This knowledge was then used to developed the simulation model in FLUENT.

Measurements were carried out for different combustion powers 8 kW-18 kW by varying the average surface temperature of the plate 20 °C-50 °C below the dew point of the mixture. The experimental results were compared with the simulation results. The discrepancies are in a range 7-25 % depending on the combustion power and the average surface temperature.

Dropwise condensation is taken place on the surface of the copper plate coated with gold instead of filmwise condensation. It is well-known that no model exists to consider the physics in dropwise condensation with a very good accuracy. In spite of this, the

deviations obtained by this model in comparison with the experiments are very good for such complicated processes as the condensation.

The copper plate was coated with gold in order to avoid wrong measurements in the composition of NO_x and SO_x at the inlet and outlet of the test section. A balance composition of these oxides was carried out to consider them as boundary condition in the simulation.

The highest deviations between experiments and simulation correspond to the smallest average surface temperature of 20 °C. The drops grow very quickly up to an equivalent diameter of approximately 1 to 3 mm. Vortices exist between the drops making the gas stream more complex as in the theoretical assumption. There is no governing equation to take into consideration this behaviour. For a higher average surface temperature of 50 °C, the drops grow slowly and they are smaller. The vortices between the drops are also small, and they have practically no influence on the main gas stream. Therefore, a better agreement between the simulation and experiments is obtained. This influence of these vortices was shown as result of the simulation carried out in this study by adding drops of different diameters to the surface of the plate.

By comparing the numerical simulation with the simulation based on the empirical correlations, it is found that the accuracy is good for almost all range of combustion power as well as average temperature surfaces. A maximal deviation of 8 % is obtained for a combustion power of 8 kW. The numerical simulation is better in these cases as the noncondensable boundary layer is thick enough requiring a better consideration of the diffusion process. In the numerical simulation, the diffusion coefficients are calculated by using the Maxwell-Stefan equation for multicomponent mixtures in which the nonidealities are taken into account. On the opposite, for the simulation based on empirical correlations, the diffusion coefficients are considered as if the mixture would be ideal.

The numerical simulation model was applied to a 3D vertical water-cooled plate and the results obtained were the same as for the 2D simulation. This model was also applied to real 3D geometries including an annular fin heat exchanger and a pin fin heat exchanger producing results which closely resemble experimental observations.

To further validate the simulation, experiments could be carried out by promoting film condensation on the surface of the water-cooled plate by using an hydrofoil product as TiO_2-Nanoparticles in order to compare the results with the ones obtained in the present work corresponding to dropwise condensation. This is a way to know if the process of condensation, film- or dropwise, have an influence in the validation of the simulation model, as this model is based on the film theory. It is expected that it should have a very small influence because the gas thermal resistance dominate over the other resistances.

The numerical simulation can be extended to other 3D geometries, and parametric studies can be performed as well as the optimization of the geometry with the goal of minimizing corrosion due to the condensation of acid gases.

The simulation model can be improved by:

- considering the evaporation process, as the acid condensate becomes increasingly corrosive after it is concentrated by repeated condensation and evaporation. But for the evaporation, the ternary mixture sulfuric acid/nitric acid/water is an aqueous solution of electrolytes. In this case, the ions to be considered are H_3O^+, SO_4^{-2} and NO_3^- and the best method to estimate the phase equilibrium of such systems is the UNIQUAQ method.
- taking into consideration the intermediate reactions that take place in the formation of the acids as well as the diffusion coefficients of these intermediate species. In reality exhaust gas temperatures range from 30 °C to1500 °C, and therefore the acids are not completely formed over the whole surface of the heat exchanger.
- considering the combined effect of the ions, NO_3^-, SO_4^{-2}, H_3O^+, on the rate of corrosion in a given material. In the present work, the rate of corrosion was calculated from diagrams corresponding to either sulfuric acid and water or nitric acid and water, but not the three components at once. Nevertheless, the diagrams for the rate of corrosion of the binary systems should be obtained in order to get more accuracy results.

Furthermore, the simulation model can be applied to other fields where condensation occurs such as exhaust gas aftertreatment e.g. Particle filter, Selective Catalytic Reduction. If the reactions that are taking place are different from the ones considered in the present research, the main structure of the program could be used but a few modifications must be made. The Vapor-Liquid Equilibrium for the system has to be estimated as well as a thorough understanding of the reaction mechanisms must be developed.

Appendices

Appendix A

Thermophysical Properties

A.1 Water

The values are based on data from Van Wylen and Sonntag [50], VDI [7] and Krey, Joachim [45]. The properties are valid from 273 to 815 K at 101325 Pa. The software CurveExperte 1.3 [55] was used to adapt the properties as a function of T in Kelvin.

Thermal Conductivity of Vapor

$\lambda=0.0167 + 6.79\ 10^{-5}\cdot T + 8.0621E\text{-}08\cdot T^2 - 3.512\ 10^{-11}\cdot T^3$ [W/m K]

Thermal Conductivity of Liquid

$\lambda=0.544 + 0.002345\cdot T - 0.00001356\cdot T^2 + 2.163\ 10^{-8}\cdot T^3$ [W/m K]

Isobaric Specific Heat of Vapor

$C_p=1.874 - 0.0001327\cdot T + 0.000003356\cdot T^2 - 6.385\ 10^{-9}\cdot T^3$ [kJ/kg K]

Isobaric specific Heat of Liquid

$C_p=4.182 + 0.0002316\cdot T - 0.0000109\cdot T^2 + 1.223\ 10^{-7}\cdot T^3$ [kJ/kg K]

Dynamic Viscosity of Vapor

$\mu=0.000008956 + 3.596E\text{-}08\cdot T + 1.1026E\text{-}11\cdot T^2 - 1.086\ 10^{-14}\cdot T^3$ [kg/m s]

Dynamic Viscosity of Liquid

$\mu=0.00156 - 0.00003467\cdot T + 3.558\ 10^{-7}\cdot T^2 - 1.379\ 10^{-9}\cdot T^3$ [kg/m s]

Density of Vapor

$\rho=0.8034 - 0.0029\cdot T + 0.00000936\cdot T^2 - 1.857\ 10^{-8}\cdot T^3$ [kg/m^3]

Density of Liquid

$\rho=1000.87 - 0.03667\cdot T - 0.004916\cdot T^2 + 0.00001041\cdot T^3$ [kg/m^3]

Enthalpy of Vaporization

$h_v=0.1229 + 4.1864\cdot T$ [kJ/kg]

Saturation Pressure

$p^{sat}= \exp(18.3036-(3816.44/T-46.13))$ [bar]

Diffusion coefficient

$D_{h2o\text{-}air} = 6.057\ 10^{-6} + 4.055\ 10^{-8}\ T + 1.25\ 10^{-10}\ T^2 - 3.367\ 10^{-14}\ T^3$ [m^2/s]

$D_{h2o\text{-}hno3} = 1.797\ 10^{-5} + 1.15\ 10^{-8}\ T + 1.548\ 10^{-10}\ T^2 - 2.81\ 10^{-14}\ T^3$ [m^2/s]

$D_{h2o\text{-}h2so4} = 1.382\ 10^{-5} + 8.874\ 10^{-8}\ T + 1.19\ 10^{-10}\ T^2 - 2.158\ 10^{-14}\ T^3$ [m^2/s]

A.2 Nitric Acid

The values are based on data from Aspen [51], NIST [52] and VDI [7]. The properties are valid from 278 to 773 K at 101325 Pa. The software CurveExperte 1.3 [55] was used to adapt the properties as a function of T in Kelvin.

Thermal Conductivity of Vapor by Harrys Model

$$\lambda = \frac{1}{152 - 38.47\ T^{0,1943}}$$ [W/m K]

Thermal Conductivity of Liquid by Richards Model

$$\lambda = \frac{0.4011}{(1 + e^{17.286 - 0.0733T})^{\frac{1}{44.3052}}}$$ [W/m K]

Isobaric Specific Heat of Vapor

$$Cp = 19.632 + 153.96 \cdot \frac{T}{1000} - 115.838 \cdot \frac{T^2}{1000} + 32.879 \cdot \frac{T^3}{1000} - \frac{0.249}{\left(\frac{T^2}{1000}\right)}$$ [J/mol K]

Isobaric Specific Heat of Liquid

$C_p = 115404.1 + 240.83 \cdot T - 2.98 \cdot T^2 + 0.0598 \cdot T^3 - 4\ 10 \cdot T^4 + 1.13\ 10^{-6}\ T^{-5}$ [kJ/kg K]

Dynamic Viscosity of Vapor [51]

$\mu = 8.465\ 10^{-6} + 3.3\ 10^{-8} \cdot T - 9.73\ 10^{-12} \cdot T^2 + 4.45\ 10^{-15} \cdot T^3 - 9.445\ 10^{-19}\ T^4$ [kg/m s]

Dynamic Viscosity of Liquid by Quadratic Model

$$\mu = \frac{1}{830.11 + 16.44\ T + 0.003345\ T^2}$$ [kg/m s]

Density of Vapor [51]

$\rho = 2.5196 \exp(-0.002\ T)$ [kg/m^3]

Density of Liquid

$\rho = 1553 \exp(-0.0013\ T)$ [kg/m^3]

Enthalpy of Vaporization

h_v=626.3 [kJ/kg]

Saturation Pressure

p^{sat}= exp(7.441+(1386.17/T+220.55)) [bar]

Diffusion coefficient [7]

$D_{hno3\text{-}h2so4} = 7.2570^{-6} + 4.66\ 10^{-8}\ T + 6.25\ 10^{-11}\ T^2 - 1.33\ 10^{-14}\ T^3$ [m^2/s]

$D_{hno3\text{-}h2o} = 1.798\ 10^{-5} + 1.15\ 10^{-8}\ T + 1.548\ 10^{-10}\ T^2 - 2.81\ 10^{-14}\ T^3$ [m^2/s]

$D_{hno3\text{-}air} = 5.309\ 10^{-7} + 1.01\ 10^{-8}\ T + 2.128\ 10^{-11}\ T^2 - 2.045\ 10^{-14}\ T^3$ [m^2/s]

A.3 Sulfuric Acid

The values are based on data from Aspen [51], NIST [52] and VDI [7]. The properties are valid from 278 to 773 K at 101325 Pa. The software CurveExperte 1.3 [55] was used to adapt the properties as a function of T in Kelvin.

Thermal Conductivity of Vapor

$\lambda = 0.00493 + 3.76\ 10^{-5} \cdot T + 7.65\ 10^{-10} \cdot T^2 - 4.09\ 10^{-12}\ T^3 + 6.64\ 10^{-15} \cdot T^4$ [W/m K]

Thermal Conductivity of Liquid

$\lambda = 0.3082383 + 0.0010763\ T$ [W/m K]

Isobaric Specific Heat of Vapor

$$Cp = 47.289 + 190.33 \cdot \frac{T}{1000} - 148.129 \cdot \frac{T^2}{1000} + 43.866 \cdot \frac{T^3}{1000} - \frac{0.74}{\left(\frac{T^2}{1000}\right)}$$ [J/mol K]

Isobaric Specific Heat of Liquid

$C_p = 131385 + 178.9 \cdot T + 0.133 \cdot T^2 - 0.000875 \cdot T^3 + 1.66\ 10^{-6} \cdot T^4$ [kJ/kg K]

Dynamic Viscosity of Vapor

$\mu = 5.3\ 10^{-6} + 1.82\ 10^{-8} \cdot T + 7.44\ 10^{-13} \cdot T^2 + 7.97\ 10^{-16} \cdot T^3 - 4.74\ 10^{-19}\ T^4$ [kg/m s]

Dynamic Viscosity of Liquid by MMF Model

$$\mu = \frac{0.0655 \cdot 61.1873 + 1.324\,10^{-5}\ T^{1.4717}}{61.187 + T^{1.4717}}$$ [kg/m s]

Density of Vapor by Reciprocal Model

$$\rho = \frac{1}{0.0008366\ T + 0.228525}$$ [kg/m^3]

Density of Liquid

$\rho=1853.25 - 1.000739 \cdot T + 0.0006165 \cdot T^2 - 4.25 \cdot 10^{-6}\ T^3 + 5.28\ 10^{-9} \cdot T^4$ [kg/m^3]

Enthalpy of Vaporization

$h_v=605$ [kJ/kg]

Saturation Pressure

$p^{sat}= \exp(8.72272-(3521.23/T+263.881))$ [bar]

Diffusion coefficient

$D_{h2so4\text{-}air} = 5.0032\ 10^{-6} + 1.04\ 10^{-8}\ T + 1.64\ 10^{-11}\ T^2 - 1.566\ 10^{-14}\ T^3$ [m^2/s]

$D_{h2so4\text{-}hno3} = 7.257410^{-6} + 4.66\ 10^{-8}\ T + 6.25\ 10^{-11}\ T^2 - 1.33\ 10^{-14}\ T^3$ [m^2/s]

$D_{h2so4\text{-}h2o} = 1.382\ 10^{-5} + 8.874\ 10^{-8}\ T + 1.19\ 10^{-10}\ T^2 - 2.158\ 10^{-14}\ T^3$ [m^2/s]

A.4 Air

The values are based on data from [49] in a temperature range from 100 to 3500 K.

Thermal Conductivity

$\lambda= 0.02364 + 0.000075624 \cdot T - 2.522\ 10^{-08} \cdot T^2 + 4.64\ 10^{-12} \cdot T^3$ [W/m K]

Isobaric Specific Heat

$C_p=1.0065 + 9.129\ 10^{-6} \cdot T - 1.81449E\text{-}07 \cdot T^2 + 3.56\ 10^{-9}\ T^3$ [kJ/kg K]

Dynamic Viscosity

$\mu=0.0000173 + 4.8717\ 10^{-8} \cdot T - 4.0264\ 10^{-11} \cdot T^2 + 4.62\ 10^{-14} \cdot T^3$ [kg/m s]

Density

$\rho=1.2917 - 0.00466 \cdot T + 0.000015047 \cdot T^2 - 2.9856\ 10^{-8} \cdot T^3$ [kg/m^3]

Appendix B

Chemical Treatment of the Test Surface

The chemical treatment of the plate surface was as follows:

- Washing in PC Cleaner (Shipley GmbH)
- Washing in distilled water
- Galvanic deposition of Nickel in a Ni-Sulfamat bath (15 mA/cm^2, 3 µm)
- Washing in distilled water
- Galvanic deposition of Gold in Aurema 311 (Degussa SA) (40 mA/cm^2, 2 µm)
- Washing in distilled water

Appendix C

Analysis of Experimental Uncertainty

In this appendix, the uncertainty analysis of the experimental work according to a suggestion of Moffat [53] is presented.

The reported estimations of uncertainty are given for a confidence level of 95 %. The uncertainty of the measurement of the variables presented in Table C.1 allows to know whether the taken values for these variables in the simulation are appropriate.

The result R of an experiment is represented by:

$R = R(X_1, X_2, X_3, ...X_n)$

where X_i are the variables of the experiment. Each variable X_i can be measured with an uncertainty ΔX_i:

$X_i(\text{true}) = X_i(\text{measured}) \pm \Delta X_i$

The influence of this uncertainty ΔX_i on the result of the experiment R can be expressed by the partial derivative:

$$\Delta R_{xi} = \frac{\partial R}{\partial X_i} \Delta X_i$$

The result of the contribution of the uncertainties of all independent variables X_i to the total uncertainty of measurement can be estimated from a root-sum-square (rss) method (Kline and Mc Clintock [54]):

$$\Delta R = \sqrt{\sum_{i=1}^{n} \left(\frac{\partial R}{\partial X_i} \Delta X_i \right)}$$

An error is usually categorised as systematic or random, depending on whether the error is steady or changes during the time of one complete experiment.

If, for the uncertainty of one variable X_i, both components, the systematic error and the random error have to be considered simultaneously, the total uncertainty of the variable X_i can be calculated by the rss combination (Moffat [53]):

$$\Delta X_i = \sqrt{\left(\Delta X_{i,\text{systematic}}\right)^2 + (2\sigma)^2}$$

where $\Delta X_{i,systematic}$ is the systematic error uncertainty and 2σ is the random uncertainty. In statistical terms σ_i is the standard deviation of the population of randomly distributed measurements.

Table C.1 Sources of uncertainty associated with the measurements

Variable	Systematic error	Random error	Total error	% Error
$T_{g,in}$, $T_{g,out}$	± 0.3 K	± 0.2 K	± 0.36 K	0.18 - 0.3
$\dot{V}$	± 4 l/h	± 8 l/h	± 8.95 l/h	5.2
T_{water}	± 0.3 K	± 0.01 K	± 0.3 K	0.1
T_{wall}	± 0.3 K	± 0.1 K	± 0.33 K	0.11
$\dot{m}_{cond,total}$	± 0.035 g		± 0.035 g	0.1
x_{h2so4}	± 1 ppm (cromatography) ± 1ppm (gas analyser)		± 2 ppm	15
$\dot{m}_{cond,h2so4}$	± 1 ppm (cromatography)		± 1 ppm	10
x_{hno3}	± 3 ppm (cromatography) ± 1ppm (gas analyser)		± 4 ppm	15
$\dot{m}_{cond,hno3}$	± 3 ppm (cromatography)		± 3 ppm	10

Appendix D

Atomic and Molecular Diffusion Volumes for the Estimation of D_{AB} by the Method of Füller, Schettler, and Giddings

The empirical correlation by Fuller, Schettler, and Giddings reads:

$$D_{AB} = \frac{0.001\,T^{1.75}(1/M_A + 1/M_B)^{1/2}}{P\,[(\sum \nu_A)^{1/3} + (\sum \nu_B)^{1/3}]^2} \qquad [0.1]$$

The quantities $\sum\nu_A$, $\sum\nu_B$ are obtained by summing atomic-diffusion volumes for each constituent of the binary. M_A, M_B are the molar mass of the components. Values of ν are listed in Table D.1. The average deviation between calculated and experimental values for binary gas systems at low pressures is 4 to 7 percent.

Table D.1 Atomic and Molecular Diffusion volumes

A) Atomic and structural diffusion volume increments, υ

C	16.5	(Cl)	19.5
H	1.98	(S)	17
O	5.48	Aromatic Ring	-20.2
(N)	5,69	Heterocyclic Ring	-20,2

B) Diffusion volumes for simple molecules, $\sum\upsilon$

H_2	7.07	CO	18.9
D_2	6.70	CO_2	26.9
He	2.88	N_2O	35.9
N_2	17.9	NH_3	14.9
O_2	16.6	H_2O	12.7
Air	20.1	(CCl_2F_2)	114.8
A	16.1	(SF_6)	69.7
Kr	22.8	(Cl_2)	37.7
(Xe)	37.9	(SO_2)	41.1

*Parentheses indicate that the value listed is based on only a few data points

Appendix E

Full Multicomponent Diffusion $D_{ij,Maxwell}$

Maxwell-Stefan Equation

The Maxwell-Stefan equations can be written as

$$\sum_{\substack{j=1\\ j\neq i}}^{N}\frac{\tilde{x}_i\tilde{x}_j}{D_{ij}}(\vec{V_j}-\vec{V_i})=\vec{d_i}-\frac{\nabla T}{T}\sum_{\substack{j=1\\ j\neq i}}^{N}\frac{\tilde{x}_i\tilde{x}_j}{D_{ij}}(\frac{D_{T,j}}{\rho_j}-\frac{D_{T,i}}{\rho_i})$$

where $\vec{V}$ is the diffusion velocity, D_{ij} is the binary mass diffusion coefficient, and D_T is the thermal diffusion coefficient.

For an ideal gas the Maxwell diffusion coefficients are equal to the binary diffusion coefficients (Appendix D). If the external force is assumed to be the same on all species and that pressure diffusion is negligible, then $\vec{d}_i=\nabla X_i$. Since the diffusive mass flux vector is $\vec{J}_i=\rho_i\vec{V}_i$, the above equation can be written as

$$\sum_{\substack{j=1\\ j\neq i}}^{N}\frac{\tilde{x}_i\tilde{x}_j}{D_{ij}}(\frac{\vec{J_j}}{\rho_j}-\frac{J_i}{\rho_i})=\overrightarrow{\nabla X_i}-\frac{\nabla T}{T}\sum_{\substack{j=1\\ j\neq i}}^{N}\frac{\tilde{x}_i\tilde{x}_j}{D_{ij}}(\frac{D_{T,j}}{\rho_j}-\frac{D_{T,i}}{\rho_i})$$

After some mathematical manipulations, the diffusive mass flux vector, $\vec{J}_i$, can be obtained from:

$$\vec{J_i}=-\sum_{j=1}^{N-1}\rho D_{ij}\nabla y_j-D_{T,i}\frac{\nabla T}{T}$$

where y_i is the mass fraction of species j. Other terms are defined as follows:

$$D_{ij,Maxwell}=[D]=[A]^{-1}[B]^{-1}$$

$$A_{ii}=-\left(\frac{\tilde{x}_i}{D_{i,N}}\frac{\tilde{M}_w}{\tilde{M}_{w,N}}+\sum_{\substack{j=1\\ j\neq i}}^{N}\frac{\tilde{x}_j}{D_{ij}}\frac{\tilde{M}_w}{\tilde{M}_{w,i}}\right)\qquad A_{ij}=\tilde{x}_i\left(\frac{1}{D_{i,j}}\frac{\tilde{M}_w}{\tilde{M}_{w,j}}-\frac{1}{D_{i,N}}\frac{\tilde{M}_w}{\tilde{M}_{w,N}}\right)$$

$$B_{ii} = -\left(\tilde{x}_i \frac{\tilde{M}_w}{\tilde{M}_{w,N}} + (1-\tilde{x}_i)\frac{\tilde{M}_w}{\tilde{M}_{w,i}} \right) \qquad B_{ij} = \tilde{x}_i \left(\frac{\tilde{M}_w}{\tilde{M}_{w,j}} - \frac{\tilde{M}_w}{\tilde{M}_{w,N}} \right)$$

where [A] and [B] are (N-1) x (N-1) matrices and [D] is an (N-1) x (N-1) matrix of the generalized Fick´s law diffusion coefficient D_{ij}.

Appendix F

Activity Coefficient for the Binary System HNO_3-H_2O

The activity coefficients have been calculated by using the Van Laar Model described in detail in chapter 2. They are valid for any temperature or pressure. These coefficients are listed in Table F.1 below.

Table F.1 Activity coefficients for system HNO_3-H_2O

y_{hno3}	γ_{hno3}	γ_{h2o}
0	0.0104	1
0.1	0.07	0.96
0.2	0.115	0.83
0.3	0.2012	0.6235
0.375	0.3056	0.5043
0.4	0.3443	0.4676
0.5	0.51	0.3396
0.6	0.6747	0.265
0.7	0.82	0.21
0.8	0.95	0.205
0.9	0.985	0.188
0.92	0.988	0.168
1	0.988	0.05807

Appendix G

Activity Coefficient for the Binary System H_2SO_4-H_2O

The activity coefficients have been calculated by using the Van Laar Model described in detail in chapter 2. They are valid for any temperature or pressure. These coefficients are listed in Table G.1 below.

Table G.1 Activity coefficients for system H_2SO_4-H_2O

y_{h2so4}	γ_{h2so4}	γ_{h2o}
$5.40\ 10^{-9}$	$9.44\ 10^{-3}$	0.95
$5.44\ 10^{-8}$	$2.37\ 10^{-3}$	0.95
$5.44\ 10^{-7}$	$3.63\ 10^{-3}$	0.95
$3.00\ 10^{-6}$	$6.73\ 10^{-3}$	0.95
$3.00\ 10^{-5}$	$1.48\ 10^{-2}$	0.88
$3.00\ 10^{-4}$	0.034	0.8
$3.00\ 10^{-3}$	0.076	0.53
$3.00\ 10^{-2}$	0.17	0.198
0.1	0.26	0.1
0.2	0.32	0.09
0.4	0.3472	0.08
0.6	0.355	0.07
0.8	0.366	0.05
0.95	0.37	0.05
0.98	0.371	0.05

Appendix H

Parameter UNIQUAQ Model

As described in chapter 2, the UNIQUAQ model takes some parameters into consideration which were determined experimentally [45]. These parameters are listed below.

r_i: molecular van der Waals volumes

r_{hno3}=1.64

r_{h2so4}=2.156

r_{h2o}=0.92

q_i:molecular surface areas

q_{hno3}=1.6

q_{h2so4}=1.513

q_{h2o}=1.4

u_{ij} and u_{ii}: energy of interaction between groups in J/mol

$u_{hno3\text{-}hno3}$=682.66

$u_{hno3\text{-}h2so4}$=0

$u_{hno3\text{-}h2o}$=-2431.66

$u_{h2so4\text{-}hno3}$=0

$u_{h2so4\text{-}h2so4}$=-3995.99

$u_{h2so4\text{-}h2o}$=-7503.19

$u_{h2o\text{-}hno3}$=-2431.66

$u_{h2o\text{-}h2so4}$=-7503.19

$u_{h2o\text{-}h2o}$=0

Bibliography

[1] Stephan, K., *Wärmeübergang beim Kondensieren und beim* Sieden, Springer Verlag (1988)

[2] Baehr, H.D., Stephan, K., *Wärme- und Stoffübertragung*, Berlin, Heidelber: Springer-Verlag (1994)

[3] Tanasawa, I., *Advances in Condensation Heat Transfer*, Advances in Heat Transfer, Vol. 21, pp.55-133 (1991)

[4] Ganzevles, F.L.A., van der Geld, C.W.M., *Temperatures and the condensate heat resistance in dropwise condensation of multicomponent mixtures with inert gases,* International Journal of Heat and Mass Transfer 45 (2002)

[5] Wagner, W., *Wärmeübertragung*, 5 Auflage, Vogel Buchverlag (1998)

[6] DeWitt, D.P, Incropera, F.P., *Fundamentals of Heat and Mass Transfer,* 4th ed. (1996)

[7] VDI-Wärmeatlas., *Berechnungsblätter für den Wärmeübergang,* 8 Auflage. Springer-Verlag Berlin (1997)

[8] Cerbe, G., *Grundlagen der Gastechnik,* 3 Auflage. Carl Hanser Verlag (1992)

[9] Recknagel, Sprenger, Schramek., *Taschenbuch für Heizung und Klimatechnik, 2000,* 69 Auflage. R. Oldenbourg Verlag (2000)

[10] Peterson P.F., Schrock V.E, Kageyama, T., *Diffusion layer theory for turbulent vapor condensation with non-condensable gases,* Journal of Heat Transfer, 115, 998-1003 (1992)

[11] Martin H., Gnielinski V., *Calculation of heat transfer from pressure drop in tube bundles,* 3rd European Thermal Sciences

[12] Pacheco, J.R., Pacheco-Vega, A.J., *The solution of viscous incompressible film flows*. *Proceedings of the 3rd European Thermal Science Conference*. Editors: E.W.P. Hahne, W. Heidemann, K. Spindler Editors, Edizioni ETS. Vol. 1, pp. 269-274 (2000)

[13] Stephan, K., *Wärmeübergang und Druckabfall bei nicht ausgebildeter Laminarströmung in Rohren und ebenen Spalten*. Chem.-Ing.-Techn.31 S.773/78 (1959)

[14] Munoz-Cobo, J.L, Herranz, L.E, Palomo, M.J., *Steam condensation modeling*

onto horizontal and inclined finned tubes with non-condensable gases: its role for new reactor containment design, 9th Internatinal Topical Meeting on Nuclear reactor Thermalhydraulics, San Francisco, California, 3-8 October (1999)

[15] Karl, J., Hein, D., *Effect of spontaneous condensation on condensation heat transfer in the presence of non-condensable gases,* 5th ASME/JSME Joint Thermal Engineering Conference, March 15-19, San Diego, California (1999)

[16] Van P.Carey., *Liquid-vapor phase-change phenomena: An Introduction to the Thermophysics of Vaporization and Condensation Processes in Heat Transfer Equipment,* G.F. Hewitt, C.L. Tien Editors (1992)

[17] HEDH *Heat Exchanger Design Handbook,* VDI-Verlag GmbH, (1986)

[18] Gnielinski,V., *Zur Wärmeübertragung bei laminarer Rohrströmung und konstanter Wandtemperatur*. Chem-Ing.-Techn.61, S.160/61 (1989)

[19] Konakov, P.K., *Berichte der Akademie der Wissenschaften der UdSSR,* BandL I, 51. Nr.7, S.503/06 (1946)

[20] Rotta, J.C., *Turbulente Strömungen*, Verlag Teubner, Stuttgart (1972)

[21] Chen, M.M., *An Analytical Study of Laminar Film Condensation,* Part1, Flat plates. Part 2, Single and multiple horizontal tubes. Trans. Am. Soc. Mech. Eng., Ser. C. J. Heat Transfer 83, 48-60 (1961)

[22] Rohsenow, W.M., *Heat Transfer and Temperature Distribution in Laminar Film Condensation,* Trans. Am. Soc. Mech. Eng., Ser. C. J. Heat Transfer 78 (1956)

[23] Gaddis, E.S. and Gnielinski, V.V., *Pressure Drop in Cross Flow Across Tube bundle,* Int.Chem. Eng. Vol.25, No.1, pp. 1-15 (1985)

[24] McAdams, *Heat Transmission,* McGraw-Hill, New York (1954)

[25] Perry, R.H., Chilton, C.H., ed., *Chemical Engineers Handbook,* 5th ed., McGraw-Hill, New York (1973)

[26] Zimmermann, H.W., *Untersuchungen zur Wirkungsgradsteigerung von Gas-Brennwertgeräten,* Dissertation Universität Kaiserslautern (1997)

[27] BC Gas Inc. *Natural Gas Characteristics and Combustion,* Canada

[28] Ambrosini, W., Brusa, L., Mazzocchi, L., Forgione, N., *Modelling Condensation on Finned Tube Heat Exchangers in the Presence of Noncondensable Gases,* Edizioni ETS, Pisa (1999)

[29] Yen-Hsiung Kiang., *Predicting Dewpoints of Acid Gases,* Chemical

Engineering, February 9 (1981)

[30] Ganzevles, F., Van der Geld, C.W.M., *Drainage and Condensate Heat Resistance in Dropwise Condensation of Multicomponent Mixtures in a Plastic Plate Heat Exchanger,* Doctoral Thesis, Netherlands (2002)

[31] Müller, P., *Beitrag zur Frage des Einflusses der Schwefelsäure auf die Rauchgas-Taupunkttemperatur,* Institut für Kolbenmaschinen der Technischen Hochschule Hannover, Chemie-Ing. Techn. 31. Jahrg. Nr 5 (1959)

[32] Hardman, R., Stacy, R. *Estimating Sulfuric Acid Aerosol Emissions from Coal-Fired Power Plants,* U. S. Department of Energy-FETC. Conference on Formation, Distribution, Impact, and Fate of Sulfur Trioxide in Utility Flue Gas Streams, March (1998)

[33] Singer, J. P., *Combustion Fossil Power*, pp. 14-36, 15-27, and 15-30 (1991)

[34] Sherwood, K., Pigford, R.L., Wilke, Ch., *Mass Transfer,* New York: McGraw Hill, Kogakuscha Ltd. (1995)

[35] Kenneth Kuan-yun K., *Principles of Combustion,* John Wiley & Sons (1986)

[36] Fluent 6.1.22 Users guide. Fluent Inc. (2003)

[37] Denny, V.E., Mills, A.F., Jusions, V.J., *Laminar Film Condensation from a Steam-Air Mixture Undergoing Forced Flow Down a Vertical Surface,* Journal of Heat Transfer, August (1971)

[38] Jackson J.D., Ahmadinejad M., *Heat Transfer from a Steam/AirMmixture to a Water-Cooled Condensing Plate,* Heat Transfer 2002

[39] Hahne, E., Grigull, U., *Formfaktor und Formwiderstand der Stationären mehrdimensionalen Wärmeleitung,* Int. J. Heat and Mass Transfer. Vol. 18, pp.751-767 (1975)

[40] *Forced Convection over a Flat Plate Experiment*, ME 412 Heat Transfer Laboratory. Summer (2003)

[41] Peterson, P., Schrock, V.E, Kageyama, T., *Diffusion layer Theory for turbulent vapor condensation with noncondensable gases,* Journal of Heat Transfer, Vol. 122, pp. 716-720 (2000)

[42] Goldbrunner, M., *Lokale Phänomene bei der Kondensation von Dampf in Anwesenheit eines nichtkondensierbaren Gases,* VDI Verlag. Dissertation Universität München (2003)

[43] Reid, R., Pausnitz, J., Poling, B., *The Properties of Gases and Liquids*.(1992)

[44] Taylor, R., Krishna, R., *Multicomponent Mass Transfer,* Wiley (1993)

[45] Krey, J., *Dampf-Flüssigkeits Gleichgewichte von Säuregemischen,* VDI Verlag Nr.372. Dissertation RWTH Aachen (1994)

[46] *Stainless Steel AL 29-4C Alloy*, Heating and Ventilating Reference Data. Allegheny Ludlum Corporation Pittsburgh, PA

[47] Ullmann Encyclopedia Ind. Chemistry 2004, 6.Ausgabe

[48] Kunze, E., *Korrosion und Korrosionsschutz*. Wiley (2000)

[49] Keenan, Chao, Keyes, *Gas Tables*, Wiley (1983)

[50] Van Wylen, Sonntag., *Fundamentals of Classical Thermodynamics*, 3rd ed, John Wiley and Sons (1986)

[51] Aspen Plus Physical Data. Version 11.1

[52] NIST Chemistry Web Book. March (2003)

[53] Moffat, R., *Describing the Uncertainties in Experimental Results,* Experimental Thermal and Fluid Science, 3-17 (1988)

[54] Kline, S. J., Mc Clintock, F. A.., *Describing Uncertainties in Single Sample Experiments,* Mechanical Engineer, p.p 3-8, January (1994)

[55] Cerbe, G., *Grundlagen der Gastechnik,* Wien:Hanser (1988)

[56] Behrens, D., *Dechema-Werkstoff-Tabelle,* september (1990)

[57] Kaminski, S., *Numerische Simulation der luftseitigen Strömungs- und Wärmetransportvorgänge in Lamellenrohr-Wärmeübertragern,* Dissertation Technische Universität Bergakademie Freiberg (2002)